Structure and surface correlations to the optical properties of nonthermal plasma-produced silicon nanoparticles

A DISSERTATION
SUBMITTED TO THE FACULTY OF THE GRADUATE SCHOOL
OF THE UNIVERSITY OF MINNESOTA
BY

Rebecca Joy Anthony

IN PARTIAL FULFILLMENT OF THE REQUIREMENTS
FOR THE DEGREE OF
DOCTOR OF PHILOSOPHY

Uwe Kortshagen, Advisor

JUNE 2011

Acknowledgements

I would like to acknowledge my funding sources for supporting my research these past years. In addition, there are many people who have helped me along the way to my degree, from my excellent adviser to my indomitable labmates to my ever-cheering friends and family. To all of you, I offer my sincerest thanks and my best wishes for your future endeavors.

Abstract

Nanomaterials have diverse capabilities to enable new technology and to deepen our understanding of our world, providing exciting prospects for scientists and the public alike in a vast span of uses. In the past decade, however, the potential held by nanotechnology has been reframed in the context of helping to slow global climate change and to alter the ways in which we use our energy to reflect more efficient technology and renewable energy sources. Silicon is a standout material in this new framework: as a nanomaterial, silicon can emit light when exposed to an applied voltage or ultraviolet optical excitation source. Silicon nanocrystals also exhibit size-dependent light emission, due to quantum confinement.

This thesis is an exploration of the synthesis and processing parameters that affect the optical performance of silicon nanocrystals produced in a nonthermal plasma reactor. The efficiency of this light emission is sensitive to both synthesis environment and post-synthesis treatment. The work presented here is an attempt to deepen our understanding of the effects of different reactor and treatment parameters on the light emission efficiency from silicon nanoparticles, such that the luminescence behavior of the nanoparticles can be specifically engineered. Being able to fine-tune the structure, surface, and optical characteristics of the silicon nanocrystals is key in maximizing their use in luminescence applications.

For all of the experiments described here, a nonthermal plasma flow-through reactor has been used to create the silicon nanoparticles. Silane gas is dissociated in the plasma and fragments come together to form silicon clusters, then grow to create

nanoparticles. The nanoparticles were collected from the reactor for further processing, characterization, and experiments.

The first discovery in this project was that by adjusting the power to the plasma reactor, the crystallinity of the silicon particles can be tuned: low power results in amorphous silicon nanoparticles, and high power yields crystalline nanoparticles. Even more important, the crystallinity of a nanoparticle ensemble relates directly to the photoluminescence (PL) efficiency, or quantum yield, from the ensemble: crystalline silicon nanoparticle samples, after alkyl functionalization, exhibit PL efficiencies of 40% or greater, while amorphous samples emit light with very poor efficiency (<2%).

Additional studies of the plasma reactor revealed the importance of injecting a flow of hydrogen gas into the afterglow of the plasma, which turns out to have dramatic implications for the ultimate PL quantum yields of the nanocrystals. This injection scheme was systematically studied by varying the injected gas and its position. Hydrogen injected directly into the plasma afterglow was found to be vital for achieving high quantum-yield silicon nanocrystals, likely due to a reduction in surface trap states due to additional hydrogen passivation at the nanocrystal surface.

Further investigations into the nanocrystal surface and how it relates to PL quantum yield showed that the photoluminescence from silicon nanocrystals is not only dependent on synthesis parameters, but also on processing temperatures and procedures following synthesis. While the highest PL efficiencies are found for silicon nanocrystals capped with alkyl chains, the PL efficiency of a nanocrystal ensemble can also be improved simply by heating the sample to temperatures between 150-200° C. This

heating step also leads to a change in the hydride structure at the nanocrystal surface, which appears to be brought about by the effusion of silyl (or disilane) groups.

Finally, details of the construction of a silicon-nanocrystal-based LED will be discussed. The LED project is part of a collaboration, and while the majority of device-specific aspects of the project were carried out in the lab of Professor R. Holmes by his Ph.D. student Kai-Yuan Cheng, the processing and alterations made to the nanocrystals used in the LED were all the responsibility of the author. The details of the project and a summary of the results bear discussion here in this thesis, as well as outlining of a novel scheme for deposition of SiNCs for device construction.

Table of Contents

List of Figures

1. Introduction

1.1 Motivation for studying silicon-based light emission

With carbon-based energy sources dwindling and rising energy costs, the global climate effects of the traditional energy economy are becoming clear. Specifically, the climate on Earth is changing—the average temperature is rising and the ice caps are melting—directly as a result of the greenhouse gases emitted into the atmosphere from human activities. In order to help reduce our dependence on fossil-fuel energy sources and curb greenhouse gas emissions, there is a new focus on developing technologies that are versatile, inexpensive to fabricate, and use as little energy as possible. One place to concentrate these new efforts is in reduction of energy expenditure due to lighting: of total electricity consumption in the United States, in residential settings 9% is used for lighting and as much as 37% of electricity in commercial settings is used for lighting.[1] Therefore, development of new, efficient, clean light sources such as solid state lighting will have a dramatic impact on energy use. The U. S. Department of Energy has developed a program to promote research into promising solid-state lighting technologies as alternatives to incandescent and fluorescent lighting.[2] Figure 1.1 shows a comparison in luminous efficacy of different types of lamps, including incandescent, compact fluorescent, and light-emitting diode (LED) lamps.[3] Both compact fluorescent and LED lamps can perform two to ten times better than incandescent lamps—but fluorescent bulbs contain toxic materials such as mercury, leading to end-of-life product disposal problems. On the other hand, LEDs can potentially be made without toxic materials, and

can also be designed as thin-film devices which take up little space compared to bulky fluorescent or incandescent bulbs.

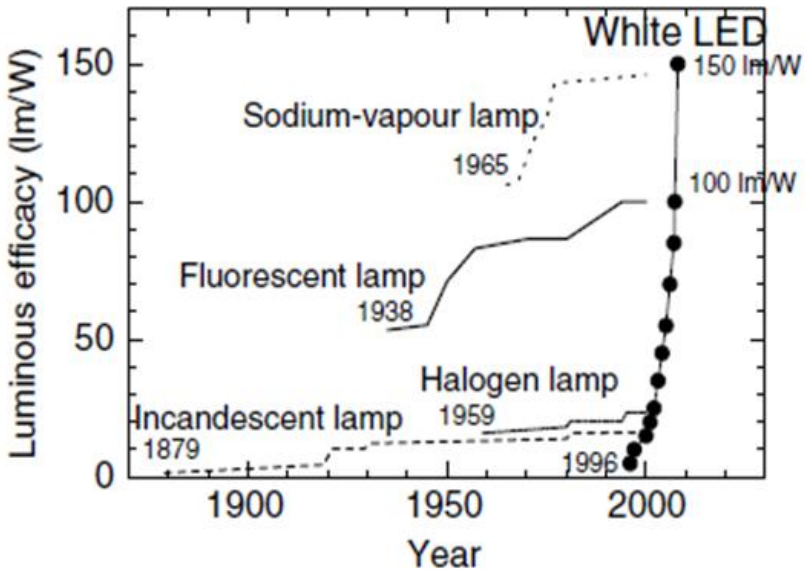

Figure 1.1: The history of luminous efficacy of white light lamps. Adapted from Narukawa, *et al.*[3]

1.2 Organic and inorganic light-emitting devices

The potential attributes of LEDs which are attractive compared to current lighting sources are improved efficacy, diminished toxicity, and a compact package. Based on these features, there are two types of light-emitting materials that fit the bill: organic molecules and polymers, and semiconductor nanocrystals. These materials can exhibit highly efficient electroluminescence, do not necessarily contain the heavy metals and materials that cause problems with fluorescent bulbs, and can be solution- or gas-phase-processed to create thin films, even enabling flexible LEDs.[4-10] The basis of LED operation is that some materials (such as bulk inorganic materials, organic molecules, and semiconductor nanocrystals) can emit light when supplied with electricity, and have the

potential to do so quite efficiently. Conventional LEDs utilize emission from bulk semiconductor materials such as gallium nitride (GaN) and gallium arsenide (GaAs), but there are spectral limitations when using bulk semiconductors. Additionally, bulk materials such as these are difficult to fabricate using thin or flexible substrates. Alternatives that allow greater spectral variation and more versatile fabrication include films of organic molecules and ultra-small inorganic semiconductors such as nanocrystals.

The first modern organic light-emitting diode (OLED) was reported in 1987 by Tang *et al.*, using a bilayer of organic molecules as the active portion of the device.[11] The organics both transported charge carriers and led to electroluminescence (EL) from the device. The first hybrid device, incorporating both nanocrystals and organic molecules, was reported in 1994 by Colvin *et al*. in a structure utilizing the polymer PPV (*p*-paraphenylene vinylene) as a charge-injection layer and several drop-cast layers of cadmium selenide (CdSe) nanocrystals as emitters.[12] There are several advantages to using hybrid organic/inorganic materials as emissive layers in LEDs. For example, due to quantum confinement, semiconductor nanomaterials can exhibit efficient electroluminescence that can be tuned according to nanoparticle size—making them excellent candidates for construction of new light-emitting devices that span the UV, visible, and infrared portions of the spectrum. In addition, the low operating voltages and stability of inorganic bulk semiconductors are potentially maintained using inorganic nanomaterials.[12] Also, solution- or gas-phase processability of these hybrid systems allows large-area deposition and the potential for flexible or thin device substrates.

1.3 Silicon nanocrystal LEDs

Since the first hybrid device,[12] semiconductor nanocrystals have been studied extensively in formation of light-emitting devices.[9,10,13-18] In particular, Group II-VI nanocrystals have shown good performance in hybrid polymer-quantum dot LEDs.[10,13,18] Group IV nanomaterials such as silicon have been less well-studied for use in LEDs, in part due to the more nuanced luminescence mechanisms of indirect-bandgap semiconductors, and because wet-chemistry synthesis methods have shown limited success for growing narrowly size-dispersed Group IV nanocrystals. In other regards, however, silicon is an excellent choice for creation of light-emitting devices. For example, it has the advantage of high natural abundance, as well as low toxicity—especially when compared to cadmium, selenium, and lead, which are some of the elements commonly used to form electroluminescent Group II-VI semiconductors. Hence, as synthesis methods for creating silicon nanocrystals have improved and as researchers have begun to understand more clearly how to control luminescence from silicon nanostructures, the use of silicon in LEDs has been increasing in recent years.[19-26]

The need for efficient light sources based on nontoxic thin-film technologies spurred the most exciting application of silicon nanocrystals (SiNCs) produced for this thesis. In collaboration with Professor Russell Holmes and his Ph.D. student Kai-Yuan Cheng in the Chemical Engineering department at the University of Minnesota, we have developed a hybrid organic/inorganic LED that combines layers of charge-injecting organic materials (polymers and small organic molecules) with an emissive layer of SiNCs. Figure 1.2 shows a cartoon of the LED. This device has, to date, the world

record for efficiency of any nanocrystal-based LED, with a peak performance of 8.6%.[19] We have worked to optimize the performance of the device by altering several aspects of LED layers and construction, and have discovered that the optical performance, surface ligand type and coverage, and layer formation of the SiNCs are vital to creating an efficient LED.

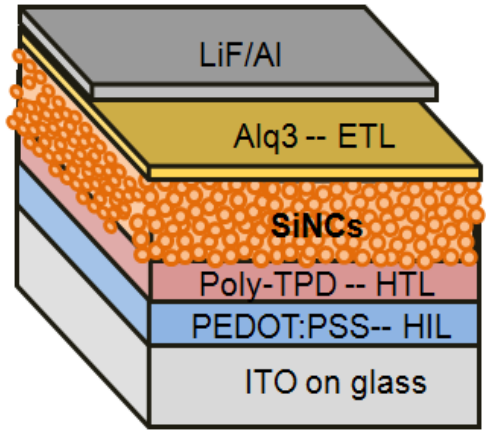

Figure 1.2: Schematic of the hybrid SiNC/organic LED.[19] Lithium Fluoride and Aluminum constitutes the top contact for the device. Alq3 and Poly-TPD are the electron transport and hole transport organic layers, respectively. PEDOT:PSS is a hole-injection layer, and ITO is the transparent contact. The SiNCs serve as the emissive layer.

The LED that motivates this work operates on the principle of electrically excited carriers—that is, charge carriers are injected through organic layers, meet and form excitons in the silicon layer, and recombine to emit visible or infrared (IR) light. The process of light emission due to electrical excitation is known as electroluminescence (EL). By contrast, light emission as a result of photoexcited carriers is known as photoluminescence (PL). The correlations between device performance and SiNC PL

quantum yield and processing parameters provide excellent motivation to study how to synthesize high-quality SiNCs and the reasons behind their PL behavior. If we can better understand how to engineer SiNCs with the highest PL quantum yields, we can not only enhance the performance of this hybrid device structure but we can also provide the framework for creation of other technologies using the emission from SiNCs.

1.4 Optical basics of silicon nanoparticles

Bulk silicon does not exhibit efficient optical emission, due to the indirect nature of its bandgap—any optical transitions between the conduction band minimum and the valence band maximum are inefficient because they require phonons to account for the difference in momentum between the two states (see Fig 1.3). However, SiNCs can be very efficient light-emitters, due to the overlap of the electron and hole wavefunctions that occurs when these charges are confined spatially. When a valence electron in silicon is promoted to the conduction band (via absorption of a high-energy photon, in the case of PL), it forms a Coulombic attraction to the hole in the valence band that takes its place: this electron-hole pair is called an exciton. The Bohr radius, which is the effective size of the exciton, is 4.9 nm for silicon.[28] In bulk silicon where the size of the crystal is, for all intents and purposes, infinite in comparison to this Bohr radius, the exciton must comply

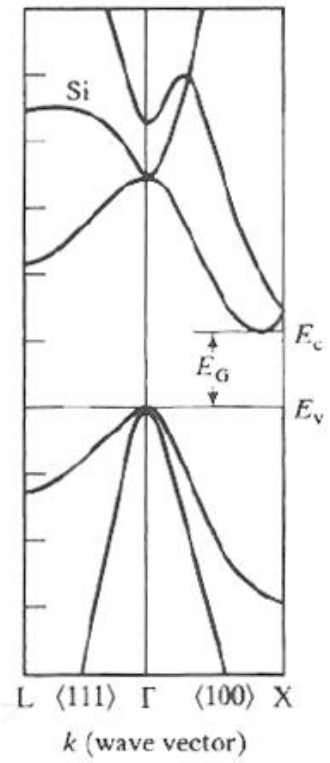

Figure 1.3: Band diagram of bulk silicon. Adapted from [27].

with quantum selection rules that govern the behavior of charges with respect to energy and momentum. However, when the crystal size approaches or becomes smaller than the effective size of the exciton, the exciton becomes confined by the boundaries of the nanocrystal. In this case, the selection rules are relaxed due to the Heisenberg uncertainty principle, and the exciton can recombine more directly. Hence, efficient luminescence can be achieved for nanocrystals with a size near or smaller than the Bohr radius of the exciton in silicon.

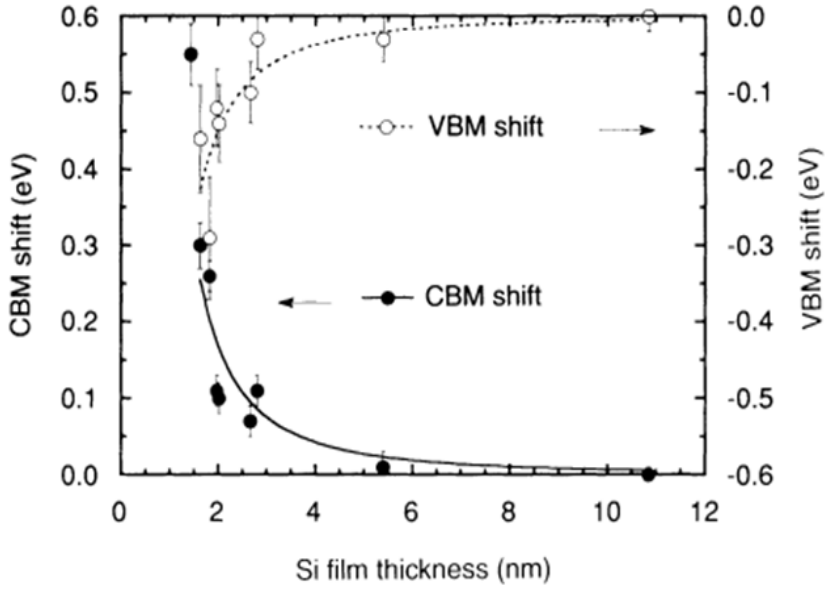

Figure 1.4: Band edge shifts in layers of crystalline silicon film, by varying thickness. Symbols represent experimental X-ray photoelectron spectroscopy data, and lines are drawn by least-squares fit. Adapted from Lu, *et al.*[29]

As the nanocrystal becomes even smaller, the band gap increases.[29,30] This allows the luminescence from silicon to be tuned, giving researchers a useful parameter in developing applications for the light emission of nanoscale silicon.

1.5 Synthesis of silicon nanocrystals

The first report of efficient room-temperature photoluminescence from silicon came in 1990, from L. T. Canham—this researcher had made porous silicon, a type of nanostructured silicon, using an electrochemical etching process and saw visible red emission upon green and blue laser excitation.[31] The interest in silicon as light-emitting material and as a potential emissive layer in LED structures increased rapidly following

that discovery. Since then, photoluminescence has been observed from porous silicon,[31-34] embedded nanoparticles of silicon,[35-38] and freestanding silicon nanoparticles,[20,39,40] among other structures.

Synthesis techniques are varied and yield an array of nanostructure features, such as crystallinity, surface termination, and dangling bond density. Liquid-phase reactions such as thermal degradation of diphenylsilane[41] and chemical reactions between silicon-based salts and other compounds[42] have had some success at producing luminescent silicon nanoparticles. It is also possible to use thermal decomposition of silane as a route to silicon nanocrystals.[43,44] Aerosol techniques include laser and thermal decomposition of silane,[39,43-45] atmospheric pressure plasma synthesis,[46-48] and ion implantation or plasma-enhanced chemical vapor deposition of SiO_x/Si films followed by annealing,[49-51] to name a few. For simply achieving silicon nanostructures, these methods can be useful; however, they also have their limitations. For example, in atmospheric-pressure synthesis methods such as laser pyrolysis, although freestanding and brightly luminescent silicon nanoparticles can be the end result,[39,52] there is typically a wide size distribution that must be narrowed after synthesis before the nanoparticles can be used effectively as light-emitters in wavelength-specific applications. In addition, these methods can lead to oxidation of the nanocrystal surface, which can hinder further processing, change opto-electronic properties, and require additional processing to remove the oxide layer.

On the other hand, using a nonthermal plasma reactor to nucleate and grow silicon nanoparticles in the gas phase allows accurate size control, adjustable particle structure, and a hydride-terminated surface that shows flexibility in post-synthesis processing

routes. Furthermore, due to charging of the nanoparticles in the plasma, they emerge from the reactor with a lesser degree of agglomeration than in some other methods. Using ordinary equipment such as a nitrogen-purged glove bag in which to collect the nanoparticles, oxidation of the silicon nanoparticle surfaces can be nearly completely avoided, preserving the native hydride coverage on the silicon surface and enabling study of pure silicon nanocrystals as well as easing wet-chemistry functionalization schemes. The low-pressure nonthermal plasma reactor has been shown effective not only for silicon nanoparticle synthesis,[40] but is used in our group also for synthesis of germanium nanocrystals[53], compounds such as indium phosphide[54] and gallium nitride, and alloy silicon-germanium nanoparticles.[55] In this work, all the nanoparticles studied were produced in this plasma reactor.

A schematic of the plasma reactor is shown in Figure 1.5—this reactor was developed by Elijah Thimsen and Lorenzo Mangolini in the Uwe Kortshagen laboratory in 2005, and has been well-characterized.[40,56] This flow-through reactor consists of a quartz or pyrex tube with a 9.5mm O.D. top portion, an expansion to a 25mm O.D., and two sidearm appendages, each with a 6.5mm O.D., located directly below the expansion zone. Argon and silane (5% in helium) are flown through the upper portion of the reactor, around which a pair of ring electrodes is situated. The ring electrodes are positioned so that the bottom edge of the grounded electrode is 2cm above the beginning of the expansion region, and there is 1cm distance between inside edges of the two electrodes.

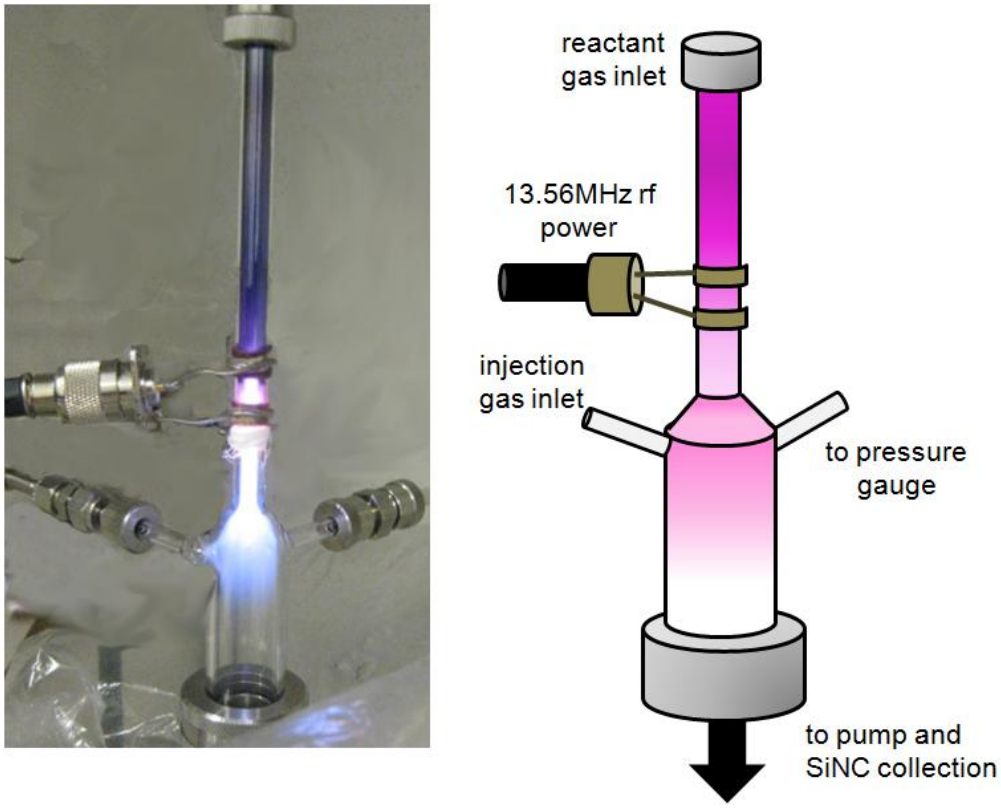

Figure 1.5: Photograph and schematic of the nonthermal plasma reactor used in this work.

Hydrogen gas is injected through one sidearm, and the other sidearm leads to a capacitance manometer to read the reactor pressure. Using a feedback-monitored butterfly valve, the pressure in the reactor is kept constant at 1.4 Torr in most cases. One of the ring electrodes is grounded, and the other is connected via a matching network to a 13.56 MHz radiofrequency (rf) power supply. When switched on, the rf power excites a plasma in the upper portion of the tube, dissociating the silane and leading to nucleation and growth of silicon nanoparticles. Particle size may be tuned simply by adjusting the flowrate of argon gas through the reactor,[40] which is an important feature as the photoluminescence peak is dependent on silicon nanoparticle size. Adjusting the power

to the reactor changes the overall crystallinity of the ensemble of nanoparticles collected, as will be discussed in detail in Chapter 2. For most of the experiments in this work, the SiNCs are collected via diffusion onto a stainless steel mesh and removed from the reactor into a nitrogen-purged glove bag for transfer into sealed vials which are then placed into an inert-atmosphere glove box or else kept air-free using a N_2-vacuum Schlenk line.

For many of the experiments presented in this thesis, the SiNCs were surface-functionalized in a thermal hydrosilylation reaction. As it is used so frequently for this work, it bears description here. Following SiNC synthesis, the sealed vial containing the collection of SiNCs is removed from the glove bag. Using the Schlenk line, 15-20mL of functionalization solution is transferred into the vial. The solution is a mixture of 5:1 v/v mesitylene:1-dodecene, which has been degassed and dried by nitrogen bubbling and molecular sieves (size 4Å). In some experiments, the functionalizing solvent types and ratios were changed to study particular SiNC attributes and applications. The SiNCs are sonicated into solution until they are no longer agglomerated at the bottom of the vial, then transferred using the Schlenk line into a prepared bulb and refluxer tube situated in a sandbath heater. A diagram of the functionalization setup is shown in Figure 1.6. The solution is heated in the bulb under nitrogen flow to 215° C (for 1-dodecene reaction; temperature varies by reactant) and cooling water in the refluxer tube is used to recondense any evaporated solvents, preventing the solution from drying during the reaction. The solution is heated for 2 hours minimum, until the nanocrystals form a clear colloid rather than a cloudy dispersion. This thermally-initiated process is detailed for

silicon surfaces[57] and has been described for plasma-produced SiNCs.[58]

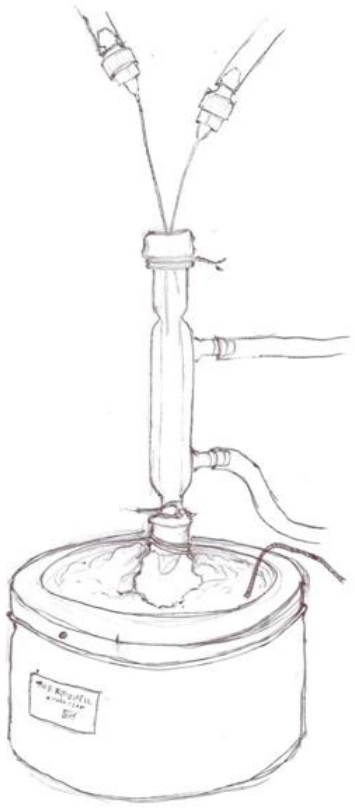

Figure 1.6: Diagram of the reactor setup for SiNC thermal functionalization.

1.6 Outline of presented work

This thesis examines distinct fabrication and treatment factors that are relevant to PL intensity in SiNCs. In the first examination, presented in Chapter 2, the effect of plasma power on the structure of SiNCs is revealed. The power applied to the plasma controls the number densities and energies of excited and ionized species in the plasma, leading to different effects on silicon nanoparticle structure. Under low-power

conditions, the silicon nanoparticles collected from the plasma have an amorphous structure, while high power leads to crystalline nanoparticles. Powers on a scale between these two extremes lead to nanoparticle ensembles with partial crystallinity. More interestingly, the structure of the silicon nanoparticles directly influences the PL efficiencies of these ensembles: silicon particles made with high power, *i.e.* nanocrystals, exhibit high PL quantum yields (>40%) whereas amorphous silicon nanoparticles, synthesized with low power, exhibit very low PL quantum yields (<5%). The results from these experiments were published in the journal *Physical Review B* under the title "Photoluminescence quantum yields of amorphous and crystalline silicon nanoparticles".[59]

In Chapter 3, we confirm the importance of hydrogen injection into the afterglow of the plasma, through the sidearm tube of the reactor. When the reactor was designed, the hydrogen injection was used to quench the plasma, providing better nanocrystal size control. However, the effect of injection gas flow on photoluminescence from the SiNCs had not been examined scientifically until this work. By means of a series of experiments in which we used different injection gases and also tested the location of gas injection, we confirmed that the maximum photoluminescence from plasma-produced silicon nanocrystals is achieved when hydrogen gas is injected directly into the afterglow of the plasma. Our work showed that hydrogen injection serves two roles: to quench particle temperature and to passivate surface states on the SiNCs. This work has been submitted to the journal *Advanced Functional Materials* with the title "Routes to achieving high quantum yield luminescence from gas-phase-produced silicon nanocrystals", and is co-

authored by David Rowe, Jihua Yang, and Matthias Stein.

The third attempt to understand photoluminescence from plasma-produced SiNCs comes from further investigations of the SiNC surface, and its role in photoluminescence quantum yield. Chapter 4 will outline this problem and the results of the study. Past experiments done by Lorenzo Mangolini implied that heating of silicon nanocrystals was key in improving PL quantum yield, for samples which had been surface-grafted with alkyl ligands in a gas-phase (a non-thermal process). To better understand why heating is necessary to raise the PL quantum yields of functionalized silicon nanocrystals, we performed heating experiments on hydrogen-terminated SiNCs, and discovered that during the heating process, a surface reorganization occurs, coinciding with the improvement in PL efficiency. This work will hopefully expand the range of possibilities for eliciting high-efficiency luminescence from films and solutions of SiNCs.

As the motivating goal of this thesis work is to improve the performance of SiNCs in light-emitting device structures, the last two portions of this thesis will focus on the SiNC LEDs that we constructed in collaboration with Professor Russell J. Holmes and Kai-Yuan Cheng in the Chemical Engineering and Materials Science Department. Chapter 5 is a modified description of the hybrid SiNC-organic LED that achieved the highest efficiency,[19] and the processes which are used in its fabrication. Specifically, the chapter will outline the first attempt at a hybrid device, which demonstrated a modest but respectable external quantum efficiency of 0.6%. Then, we will discuss the changes to the structure that led to the record-breaking 8.6% efficiency device. We will also explain some additional studies that are in progress with respect to the SiNC surface

functionalization and how that impacts the device performance.

Chapter 6 describes an exciting new process for depositing luminescent SiNCs directly onto LED substrates, in complete avoidance of liquid-phase processes. Although the LED incorporates no organic layers and exhibits low EQE, the fact that the SiNCs can be functionalized and deposited in a gas-phase-only scheme, and lead to photo- and electroluminescence as-deposited, is a promising result of this project. This work will be submitted for publication to *Nano Letters* under the title "Luminescent films of surface-functionalized silicon nanocrystals: a gas-phase-only approach to device formation", co-authored by Kai-Yuan Cheng and Professor Russell J. Holmes.

References

(1) Independent Statistics and Analysis: U. S. Energy Information Administration **2003**.

(2) EERE: Solid-State Lighting Home Page **2010**.

(3) Narukawa, Y.; Ichikawa, M.; Sanga, D.; Sano, M.; Mukai, T. *Journal of Physics D: Appled Physics* **2010**, *43*.

(4) Weaver, M. S.; Michalski, L. A.; Rajan, K.; Rothman, M. A.; Silvernail, J. A.; Brown, J. J.; Burrows, P. E.; Graff, G. L.; Gross, M. E.; Martin, P. M.; Hall, M.; Mast, E.; Bonham, C.; Bennett, W.; Zumhoff, M. *Applied Physics Letters* **2002**, *81*, 2929-2931.

(5) Lee, K. J.; Lee, J.; Hwang, H.; Reitmeier, Z. J.; Davis, R. F.; Rogers, J. A.; Nuzzo, R. G. *Small* **2005**, *1*, 1164-1168.

(6) Santato, C.; Manunza, I.; Bonfiglio, A.; Cicoira, F.; Cosseddu, P.; Zamboni, R.; Muccini, M. *Applied Physics Letters* **2005**, *86*.

(7) Schrage, C.; Kaskel, S. *ACS Applied Materials & Interfaces* **2009**, *1*, 1640-1644.

(8) Willander, M.; Nur, O.; Bano, N.; Sultana, K. *New Journal of Physics* **2009**, *11*.

(9) Tan, Z.; Xu, J.; Zhang, C.; Zhu, T.; Zhang, F.; Hedrick, B.; Pickering, S.; Wu, J.; Su, H.; Gao, S.; Wang, A. Y.; Kimball, B.; Ruzyllo, J.; Dellas, N. S.; Mohney, S. E. *Journal of Applied Physics* **2009**, *105*.

(10) Kim, T.; Cho, K.; Lee, E. K.; Lee, S. J.; Chae, J.; Kim, J. W.; Kim, D. H.; Kwon, J.; Amaratunga, G.; Lee, S. Y.; Choi, B. L.; Kuk, Y.; Kim, J. M.; Kim, K. *Nautre Photonics* **2011**, *5*, 176-182.

(11) Tang, C. W.; VanSlyke, S. A. *Applied Physics Letters* **1987**, *51*, 913-915.

(12) Colvin, V. L.; Schlamp, M. C.; Alivisatos, A. P. *Nature* **1994**, *370*, 354-357.

(13) Coe-Sullivan, S.; Woo, W.; Steckel, J. S.; Bawendi, M.; Bulovic, V. *Organic Electronics* **2003**, *4*, 123-130.

(14) Anikeeva, P. O.; Halpert, J.; Bawendi, M.; Bulovic, V. *Nano Letters* **2009**, *9*, 2532-2536.

(15) Chitara, B.; Bhat, S. V.; Vivekchand, S. R. C.; Gomathi, A.; Rao, C. N. R. *Solid State Communications* **2008**, *147*, 409-413.

(16) Anikeeva, P. O.; Halpert, J. E.; Bawendi, M. G.; Bulovic, V. *Nano Letters* **2007**, *7*, 2196-2200.

(17) Sun, Q.; Subramanyam, G.; Dai, L.; Check, M.; Campbell, A.; Naik, R.; Grote, J.; Wang, Y. *ACS Nano* **2009**, *3*, 737-743.

(18) Wood, V.; Panzer, M. J.; Caruge, J.; Halpert, J. E.; Bawendi, M. G.; Bulovic, V. *Nano Letters* **2010**, *2010*, 24-29.

(19) Cheng, K.; Anthony, R.; Kortshagen, U. R.; Holmes, R. J. *Nano Letters* **2011**, *11(5)*,1952-1956.

(20) Cho, K. S.; Park, N.; Kim, T.; Kim, K.; Sung, G. Y. *Applied Physics Letters* **2005**, *86*.

(21) Hirschman, K. D.; Tsybeskov, L.; Duttagupta, S. P.; Fauchet, P. M. *Nature* **1996**, *384*, 338-341.

(22) Anopchenko, A.; Marconi, A.; Moser, E.; Wang, M.; Pucker, G.; Bellutti, P.; Pavesi, L. *IEEE Conference on Group IV Photonics* **2009**.

(23) Huh, C.; Kim, K.; Kim, B. K.; Kim, W.; Ko, H.; Choi, C.; Sung, G. Y. *Advanced Materials* **2010**, *2010*, 5058-5062.

(24) Cheng, K.; Anthony, R.; Kortshagen, U. R.; Holmes, R. J. *Nano Letters* **2010**, *10(4)*, 1154-1157.

(25) Puzzo, D. P.; Henderson, E. J.; Helander, M. G.; Wang, Z.; Ozin, G. A.; Lu, Z. .

(26) Ligman, R. K.; Mangolini, L.; Kortshagen, U. R.; Campbell, S. A. *Applied Physics Letters* **2007**, *90*.

(27) Pierret, R. F. *Advanced Semiconductor Fundamentals*; Modular Series on Solid State Devices; Second Edition.; Pearson Education, Inc.: Upper Saddle River, New Jersey, 2003; Vol. VI.

(28) Beard, M. C.; Knutsen, K. P.; Pingrong, Y.; Luther, J. M.; Song, Q.; Metzger, W. K.; Ellingson, R. J.; Nozik, A. J. *Nano Letters* **2007**, *7*, 2506-2512.

(29) Lu, Z. H.; Lockwood, D. J.; Baribeau, J. *Nature* **1995**, *378*, 258-260.

(30) Wang, L.; Zunger, A. *Journal of Physical Chemistry* **1994**, *98*, 2158-2165.

(31) Canham, L. T. *Applied Physics Letters* **1990**, *57*, 1046-1048.

(32) Cullis, A. G.; Canham, L. T. *Nature* **1991**, *353*, 335-338.

(33) Boukherroub, R.; Morin, S.; Wayner, D. D. M.; Bensebaa, F.; Sproule, G. I.; Baribeau, J.; Lockwood, D. J. *Chemical Materials* **2001**, *13*, 2002-2011.

(34) Matsumoto, T.; Belogorokhov, A. I.; Belogorokhova, L. I.; Masumoto, Y.; Zhukov, E. A. *Nanotechnology* **2000**, *11*, 340.

(35) Wang, Y. Q.; Kong, G. L.; Chen, W. D.; Diao, H. W.; Chen, C. Y.; Zhang, S. B.; Liao, X. B. *Applied Physics Letters* **2002**, *81*, 4174-4176.

(36) Comedi, D.; Zalloum, O. H. Y.; Wojcik, J.; Mascher, P. *IEEE Journal of Selected Topics in Quantum Electronics* **2006**, *12*, 1561-1569.

(37) Kim, S.; Park, Y. M.; Choi, S.; Kim, K. J. *Journal of Applied Physics* **2007**, *101*.

(38) Xie, Z.; Zhu, J.; Zhang, M.; Zhao, Y.; Lu, M. *Applied Surface Science* **2009**, *255*, 3833-3836.

(39) Li, X.; He, Y.; Talukdar, S. S.; Swihart, M. T. *Langmuir* **2003**, *19*, 8490-8496.

(40) Mangolini, L.; Thimsen, E.; Kortshagen, U. *Nano Letters* **2005**, *5*, 655-659.

(41) Holmes, J. D.; Ziegler, K. J.; Doty, R. C.; Pell, L. E.; Johnston, K. P.; Korgel, B. A. *Journal of the American Chemistry Society* **2001**, *123*, 3743-3748.

(42) Liu, Q.; Kauzlarich, S. M. *Materials Science and Engineering B96* **2002**, 72-75.

(43) Littau, K. A.; Szajowski, P. J.; Muller, A. J.; Kortan, A. .. R.; Brus, L. E. *Journal of Physical Chemistry B* **1993**, *97*, 1224-1230.

(44) Onischuk, A. A.; Levykin, A. I.; Strunin, V. P.; Ushakova, M. A.; Samoilova, R. I.; Sabelfeld, K. K.; Panfilov, V. N. *Journal of Aerosol Science* **2000**, *31*, 879-906.

(45) Brus, L. E.; Szajowski, P. F.; Wilson, W. L.; Harris, T. D.; Schuppler, S.; Citrin, P. H. *Journal of the American Chemistry Society* **1995**, *117*, 2915-2922.

(46) Nozaki, T.; Sasaki, K.; Ogino, T.; Asahi, D.; Okazaki, K. *Nanotechnology* **2007**, *18*.

(47) Gupta, A.; Swihart, M. T.; Wiggers, H. *Advanced Functional Materials* **2009**, *19*, 696-703.

(48) Sankaran, R. M.; Holunga, D.; Flagan, R. C.; Giapis, K. P. *Nano Letters* **2005**, *5*, 537-541.

(49) Garrido Fernandez, B.; Lopez, M.; Garcia, C.; Perez-Rodriguez, A.; Morante, J. R.; Bonafos, C.; Carrada, M.; Claverie, A. *Journal of Applied Physics* **2002**, *91*, 798-807.

(50) Irrera, A.; Iacona, F.; Crupi, I.; Presti, C. D.; Franzo, G.; Bongiorno, C.; Sanfilippo, D.; Di Stefano, G.; Piana, A.; Fallica, P. G.; Canino, A.; Priolo, F. *Nanotechnology* **2006**, *17*, 1428-1436.

(51) Pi, X. D.; Zalloum, O. H. Y.; Roschuk, T.; Wojcik, J.; Knights, A. P.; Mascher, P.; Simpson, P. J. *Applied Physics Letters* **2006**, *88*.

(52) Ledoux, G.; Gong, J.; Huisken, F.; Guillois, O.; Reynaud, C. *Applied Physics Letters* **2002**, *80*, 4834-4836.

(53) Gresback, R.; Holman, Z.; Kortshagen, U. *Applied Physics Letters* **2007**, *91*.

(54) Gresback, R.; Hue, R.; Gladfelter, W. L.; Kortshagen, U. R. *Nanoscale Research Letters* **2011**, *68*.

(55) Pi, X. D.; Kortshagen, U. *Nanotechnology* **2009**, *20*.

(56) Mangolini, L.; Jurbergs, D.; Rogojina, E.; Kortshagen, U. *physics status solidi (c)* **2006**, *3*, 3875-3978.

(57) Buriak, J. M. *Chemical Reivews* **2002**, *102*, 1272-1308.

(58) Jurbergs, D.; Rogojina, E.; Mangolini, L.; Kortshagen, U. *Applied Physics Letters* **2006**, *88*.

(59) Anthony, R.; Kortshagen, U. *Physical Review B* **2009**, *80*.

2. Photoluminescence quantum yields from amorphous and crystalline silicon nanoparticles

2.1 Introduction

Since the first observation of efficient photoluminescence PL from nanoscale silicon[1,2] this topic has attracted considerable attention due to the potentially high PL efficiencies that can be achieved over a broad spectral range from silicon nanocrystals (NCs). As an indirect band-gap semiconductor, bulk silicon is an inefficient optical emitter and absorber. However, it is now widely accepted that the optical properties of nanoscale crystalline silicon are considerably improved due to a combination of two effects: the enhanced overlap of electron and hole wave functions in quantum confined silicon leading to faster recombination[3] and the reduction in the rate of nonradiative events.[4]

There have been a number of reports that have demonstrated that nanocrystalline silicon can achieve photoluminescence quantum yields rivaling those of direct band-gap semiconductors. An important measure of the optical quality of silicon nanocrystals is the quantum yield (QY) for photoluminescence defined as the number of photons emitted divided by the number of exciting photons absorbed. While silicon nanocrystals passivated by native oxide layers typically have PL QYs of up to about 10%, there have

been limited reports of even higher quantum yields of up to 30%.[5] High QYs were also found for the silicon nanocrystals embedded in high-quality thermal oxides.[6] The surface functionalization with organic monolayers is another proven way to achieve high-efficiency PL from silicon nanocrystals.[7,8] In Refs. 9 and 10, we reported QYs as high as 70% for ensembles of nonthermal plasma produced SiNCs[11] whose surfaces were treated with 1-dodecene under careful avoidance of oxygen. Moreover, in single quantum dot experiments, PL QYs as high as 88% were observed for individual quantum dots.[12] However, these studies also found an often large difference between the QYs of individual particles and nanocrystal ensembles, whose QYs were found to be on the order of just a few percent due to the large fraction of "dark," i.e., nonemitting, particles. Significantly fewer reports have addressed optical emissions from amorphous silicon nanoclusters. Several groups[13-17] have reported photoluminescence from amorphous silicon nanoparticles (a-NPs) embedded in solid-state matrices. In the work by Park et al.,[16,17] several sizes of a-NPs were produced in SiO_2. Size-tunable photoluminescence from these amorphous particles was reported ranging from blue to red. The blueshift of photoluminescence energy upon shrinkage of particle size indicated that quantum confinement effects may be seen in amorphous nanoscale silicon. In the paper by Molinari et al.,[18] it was suggested that the PL from amorphous silicon nanoclusters in SiO_2 and Si_3N_4 matrices is due to quantum confinement but that the emission intensity and efficiency are lower than those for nanocrystalline particles because of the higher number of nonradiative recombination centers in amorphous clusters. This group proposes that well-passivated crystalline silicon nanoparticles will have much more

intense PL due to fewer of these defects. Work presented in Refs. 19 and 20 arrives at similar conclusions. While luminescence could be observed from a-NPs, the luminescence from crystalline particles was found to be more efficient.

Previous studies of the emission of amorphous silicon nanoparticles have been limited to clusters embedded in dielectric matrices such as SiO_2 and Si_3N_4. In such systems, it is often difficult to distinguish between intrinsic limitations of the material itself and extrinsic limitations caused by the presence of the interface with the surrounding matrix. It is also difficult to perform absolute measurements of the photoluminescence quantum yield. In fact, such measurements have not been reported to date; hence, it is difficult to quantify what the reports of "efficient luminescence" from a-NPs actually mean. In this paper, we will study the PL efficiency of freestanding silicon a-NPs compared to those of free-standing silicon NCs. The use of free-standing nanoparticles suspended in colloidal solution enables the absolute measurement of the photoluminescence quantum yield, which is routinely reported in the nanocrystal literature, and which we had previously established for silicon nanocrystals.[9,10] Measurements of the absolute QY will enable us to quantify the luminescence efficiency of amorphous silicon particles. The use of free-standing silicon particles also enables the same careful passivation of the a-NP surfaces that provided ensemble QYs as high as 70% for silicon nanocrystals[9,10] and may allow conclusions about the intrinsic luminescence potential of amorphous silicon nanoclusters. The particle structure is varied between amorphous and crystalline by adjusting the power delivered to the plasma. We study silicon particles with surfaces functionalized both with organic monolayers and a

native oxide layer. Results of absolute QY measurements for ensembles of amorphous and crystalline free-standing silicon nanoparticles are reported.

2.2 Experimental Details

We synthesized silicon nanoparticles in a nonthermal low pressure plasma reactor, as described previously.[11] The quartz reactor has a 10-mm-outer diameter reaction area, where the radiofrequency electrode is placed, which then expands to 25-mm-outer diameter before exiting to the collection filter and pump. The size of the particles is controlled by adjusting the flow rate of argon gas through the reactor tube between 25 and 100 sccm standard cubic centimeters per minute(sccm). Silane gas (5% in helium) was flown through the reactor tube at 13-14 sccm and hydrogen gas was injected at 100 sccm *via* a sidearm into the 25 mm expansion region of the reactor tube. When the argon flow rate was greater than 50 sccm, 2 sccm of additional hydrogen was added to the reactant gas mixture. To change the crystallinity of the particles, we adjusted the 13.56 MHz radiofrequency input power to the reactor between 25 and 100 W. Crystalline and amorphous particles of four sizes were synthesized from 3 to 5 nm in diameter. Following synthesis, some of the amorphous and crystalline particle samples of several sizes were surface processed with a 5:1 v/v mixture of mesitylene and 1-dodecene in a liquid-phase thermal hydrosilylation reaction[10] to render them stable in nonpolar solvent dispersions and to help protect the nanoparticles from oxidation. For a sample of 5 nm silicon NCs, the hydrosilylation procedure yielded a clear colloidal dispersion of particles by the end of a 2 to 3 h refluxing period at 205–215 °C. This reaction time was fairly

consistent for NCs. Reaction time increased with decreasing particle size, but even the smallest NCs examined in this study reacted with the 1-dodecene to form a clear colloid. While, due to steric hindrance of the ligand molecules, it is not expected that more than 30% to 40% of the silicon NC surface sites are functionalized with ligand molecules,[21] we showed in Ref. 22 that this procedure yields colloids of individually dispersed Si NCs. We also found that the remaining surface sites are covered with hydrogen from the plasma reaction. In this study we found that a-NPs require longer reaction times before a clear solution is obtained. In fact, for the smallest a-NPs, a clear colloidal dispersion is never achieved. This hints at a different surface structure of the a-NPs compared to NCs, which was not further examined in the present study.

To examine the effects of oxidation on the particle photoluminescence, several samples of each phase were dispersed while still bare (unfunctionalized) and were allowed to oxidize naturally due to contact with air in the environment. The PL from these samples was measured periodically. The particle samples were characterized in the University of Minnesota Characterization Facility, using an FEI Tecnai T-12 transmission electron microscope (TEM) for TEM images, a Bruker-AXS Microdiffractometer for x-ray diffraction (XRD) spectra, and a confocal Raman microscope Witec alpha300-R confocal Raman microscope with UHTS300 spectrometer and DV401 charge-coupled device for Raman vibrational spectroscopy. The photoluminescence quantum yields of the nanoparticles were measured at room temperature using a light-emitting diode (LED) excitation source at 390–400 nm, an integrating sphere, and a USB2000 spectrometer Ocean Optics, Inc. The procedure for

measuring quantum yields is described in detail in Ref. 10.

2.3 Results

2.3.1 Nanoparticle structural characterization

An increase in plasma power generally leads to increasing crystallinity of the nanoparticle samples. In Ref. 23, we showed that nanoparticles immersed in a plasma are strongly heated to temperatures several hundreds of Kelvin beyond the gas temperature through exothermic surface reactions, including electron-ion recombination and hydrogen-induced surface reactions. An increase in plasma power leads to increasing densities of the species involved in these surface reactions including electrons, ions, and atomic hydrogen radicals. Hence, increasing the plasma power leads to a significant increase in the particle heating, which we expect causes the transition from a-NPs to NCs with increasing power.

To verify the changing crystallinity of the nanoparticles, we synthesized several samples under the same flow and pressure parameters, with varying input powers. XRD patterns clearly show an increase in silicon particle crystallinity as we increase synthesis power (see Fig. 2.1). We took Raman vibrational spectra to corroborate this conclusion and the emergence of a peak near 520 cm^{-1}, corresponding to crystalline silicon, demonstrates the increase in crystallinity with increasing power (see Fig. 2.2). It should be noted that a quantitative determination of the crystal fraction from Raman spectra is

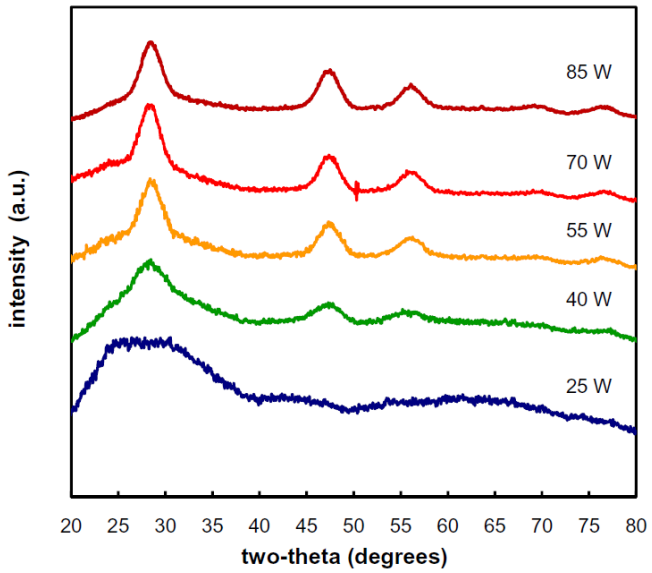

Figure 2.1: X-ray diffraction patterns from silicon nanoparticles produced at varying input powers. Peaks typical of silicon nanocrystallites are visible in all except the lowest-power sample.

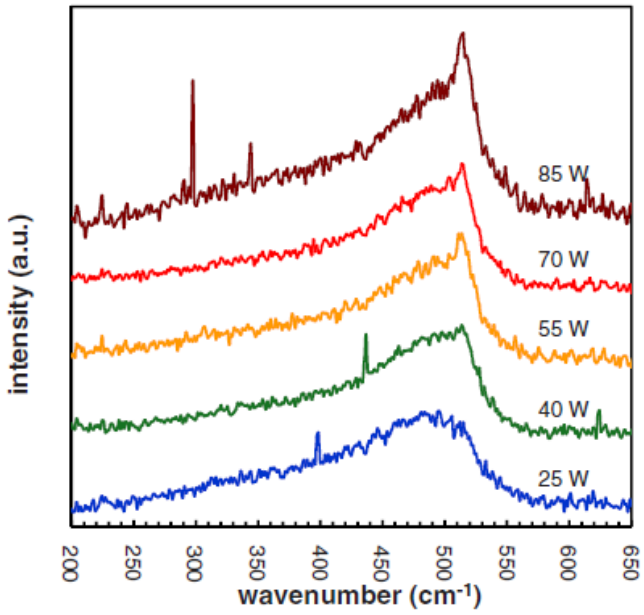

Figure 2.2: Raman spectra of silicon nanoparticle samples. The sharp peak near 520 cm^{-1}, indicative of silicon crystallites, first appears for the 40W sample, and increases with increasing power.

not straightforward, as the transverse optical peak near 520 cm^{-1} can be strongly asymmetric due the presence of strain and of a particle size distribution.[24] The XRD and Raman spectroscopy data shown here are consistent with the data found in the structural characterization of NCs by other authors.[25,26] We also performed TEM studies to characterize both the size and microstructure of produced samples (see Fig. 2.3). The bright-field TEM images in Figs. 3a and 3b demonstrate that the produced particles are highly monodisperse. The a-NPs and NCs have approximately the same size. It is obvious that NCs have more well-defined spherical shapes, while the shapes of a-NPs are slightly more irregular. The selected-area electron-diffraction (SAED) pattern shows bright diffraction rings attributable to a polycrystalline sample in the high-power case (Fig. 2.3b), while the SAED pattern from the low-power sample shows only a diffuse glow, indicative of amorphous material (Fig. 2.3a). Furthermore, well-defined bright areas of the dark-field image from the high-power sample further illustrate the crystallinity of the NCs (Fig. 2.3d). In the low-power sample, the dark-field image shows no crystal definition (Fig. 2.3c).

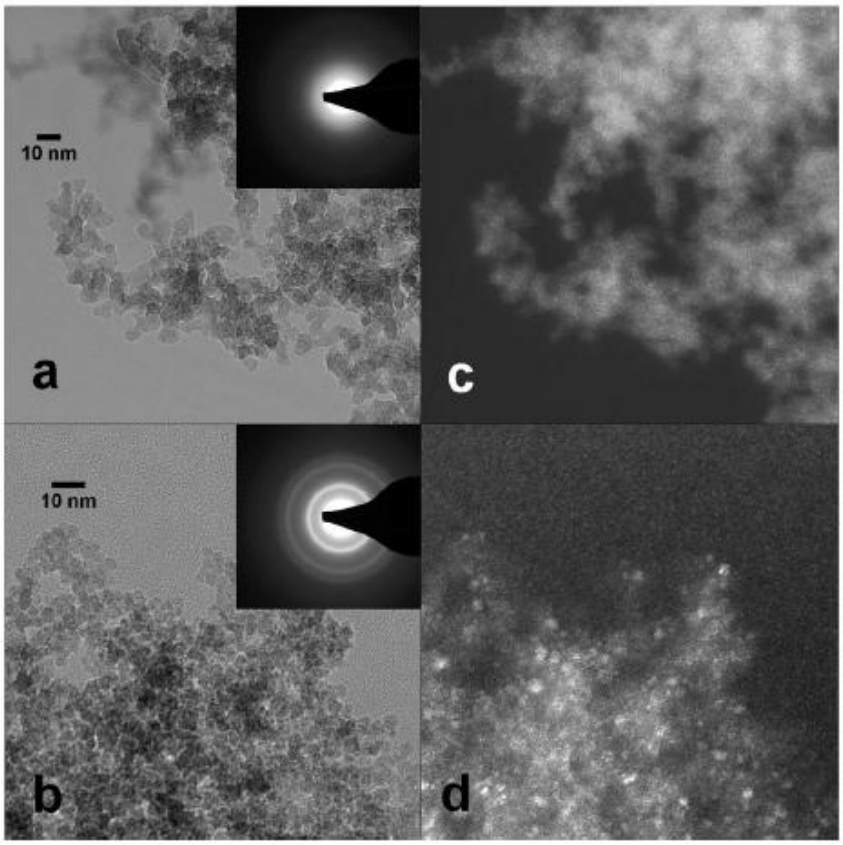

Figure 2.3: Transmission electron micrographs of silicon particles. (a) and (b) are bright-field images of NCs and a-NPs, respectively, with SAED patterns inset. (c) and (d) are dark-field images.

2.3.2 Photoluminescence quantum yields

We recorded and analyzed the photoluminescence spectrum of each liquid sample of surface-functionalized silicon particles to obtain the sample's ensemble quantum yield. These measurements were taken with the NCs and a-NPs dispersed in the residual functionalizing mixture of mesitylene and 1-dodecene. With decreasing input power and, thus, decreasing particle crystallinity, the quantum yields decreased as well. In fact, the QYs from the samples of a-NPs were so low as to be hardly measurable using our

instrument. Figure 2.4a displays a plot of PL QYs as a function of input power. All samples in this plot were synthesized with argon flow rates between 20–40 sccm. At high synthesis powers, high efficiency photoluminescence of the NCs prevails; at powers below 50 W, the samples do not exhibit the same high-efficiency photoluminescence.

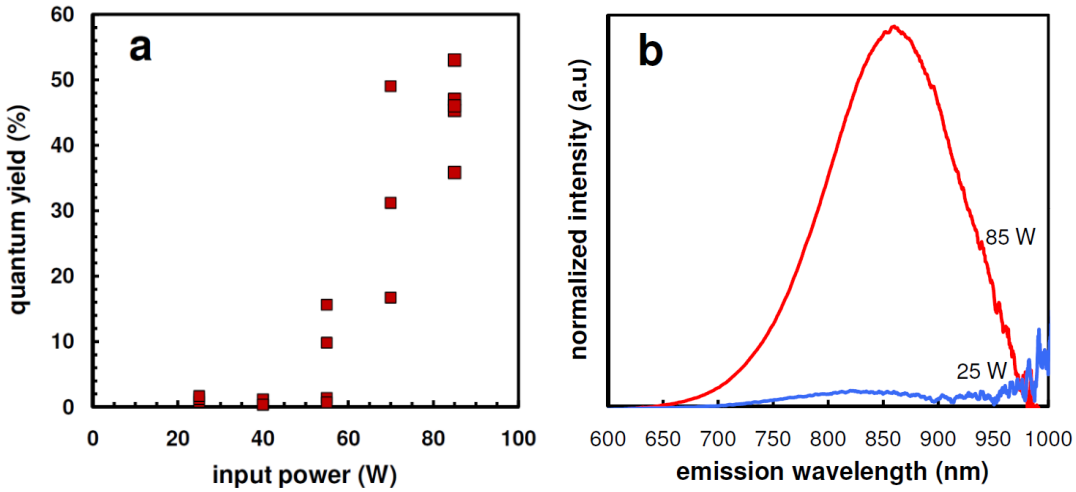

Figure 2.4: Photoluminescence quantum yields of samples (a) and PL spectrum comparison from 85W and 25W samples (b).

Samples generated with powers between 50–70 W show clear crystalline features in their XRD and Raman spectra. However, PL QYs for samples made at these powers vary from very low to moderately high, despite clear evidence that the samples have a measurable nanocrystalline fraction. The only samples for which we see consistently high-efficiency PL are those made at powers of 85 W or greater. A direct comparison of the photoluminescence spectra for NCs (85 W) and a-NPs (25 W) of the same size is shown in Fig. 4b. The PL from the a-NP sample is clearly significantly weaker than PL from the NC sample. This behavior was consistently found for all sizes of the samples studied.

It is important to note that the system variability contributes significantly to the degree of sample-to-sample variability seen in Fig. 2.4a. Each sample preparation requires partial disassembly and reassembly of the plasma reactor, which may cause slight changes in electrode position and other minor adjustments. We found that these lead to changes in the plasma conditions between samples which, at the transition from the a-NP to the NC regime, can lead to changes in the crystallinity for samples prepared at the same power. This likely explains why samples produced at 40 W show only very low quantum yield, yet the 40 W sample prepared for Raman (Fig. 2.2) and XRD (Fig. 2.1) diagnostics showed slight signatures for crystallinity. It likely also explains the strong sample-to-sample variation for the higher-power samples.

It is difficult to determine precisely whether the weak emission observed from low-power samples is indeed due to emission from a-NPs or caused by a very small and hard to detect fraction of NCs. For instance, if a-NPs were non-emitting, a fraction of 1% of nanocrystals with an intrinsic QY of 45% would be interpreted as a sample with an ensemble quantum yield of 0.45%, a value which is consistent with the values observed in our measurements (see Fig. 2.4a). A crystalline fraction of a few percent in an otherwise amorphous sample would be difficult to detect with XRD or Raman scattering. However, the emission spectra in Fig. 2.4b suggest that the emission observed from the low-power sample may indeed originate from a small fraction of NCs in an otherwise amorphous sample. The emission of the a-NP sample produced at 25 W occurs at roughly the same emission wavelength as the emission of the NC sample produced at 85 W. While TEM observations suggest that the particle sizes for both samples are the same, the

emission of silicon NCs and a-NPs is not necessarily expected to occur at the same wavelengths. As suggested by Park et al.,[17] the emission energy E of quantum-confined amorphous silicon nanoclusters is expected to follow the relation:

$$E\ (eV) = 1.56 + {}^{2.4}/_{a^2}$$

with a as the nanoparticle diameter in nm. Hence, even for large a-NPs, emission should not be expected at wavelengths larger than 790 nm i.e., 1.56 eV. However, it is clearly observed from the a-NP sample in Fig. 4b. This suggests that the emission observed from the a-NP sample is from a small fraction of NCs that is too small to be observed with XRD or Raman.

While the classification of samples as "amorphous" is obviously not entirely unambiguous, the measurements presented here allow us to place an upper bound on the absolute QY of a-NPs in that no sample that we characterized as amorphous has shown a QY larger 2%. Hence, we can establish 2% as the upper bound for the absolute QY of freestanding silicon a-NPs with hydrosilylated surfaces, which is considerably lower than the QYs of 50% observed for NCs with the same surface treatment.

2.3.3 Oxidation experiments

Hydrosilylation is one mechanism of passivating dangling bonds at the nanoparticle surface[27] through the organic ligands and surface hydrogen and, thus, increasing ensemble quantum yields of the NCs, while a-NPs show PL with very low QY. However, many of the reports of PL from silicon a-NPs were based on particles embedded in a matrix of silicon nitride or silicon dioxide. To emulate these conditions, we allowed some

samples to oxidize in order to study the PL of particles when coated in an oxide shell. The formation of a native oxide shell on silicon nanocrystals is known to lead to an increase in the PL QY since the native oxide removes nonradiative surface states.[5]

We synthesized samples at 25, 55, and 85 W then dispersed the samples in chloroform and allowed them to oxidize via exposing the samples to air. As time progressed, we measured the quantum yields of these samples periodically (see Fig. 2.5a). The samples made at 85W initially had low PL efficiency, which increased in time as the particles oxidized. The growth of the oxide layer passivates the surface defects, leaving the NC core intact and able to emit efficiently. The samples also showed a blueshift in emission energy, in accordance with a shrinking nanocrystalline core (Fig. 2.5b), as the quantum-confined exciton energy is size dependent.[28] While the rate of emission blueshift was rapid in the early stages of oxidation, over a period of several months, this rate slowed to near zero. This blueshift was present in all samples prepared at different power levels. The sample prepared at 55 W shows a lower QY than the sample at 85 W, consistent with the likely lower crystalline fraction of this sample.

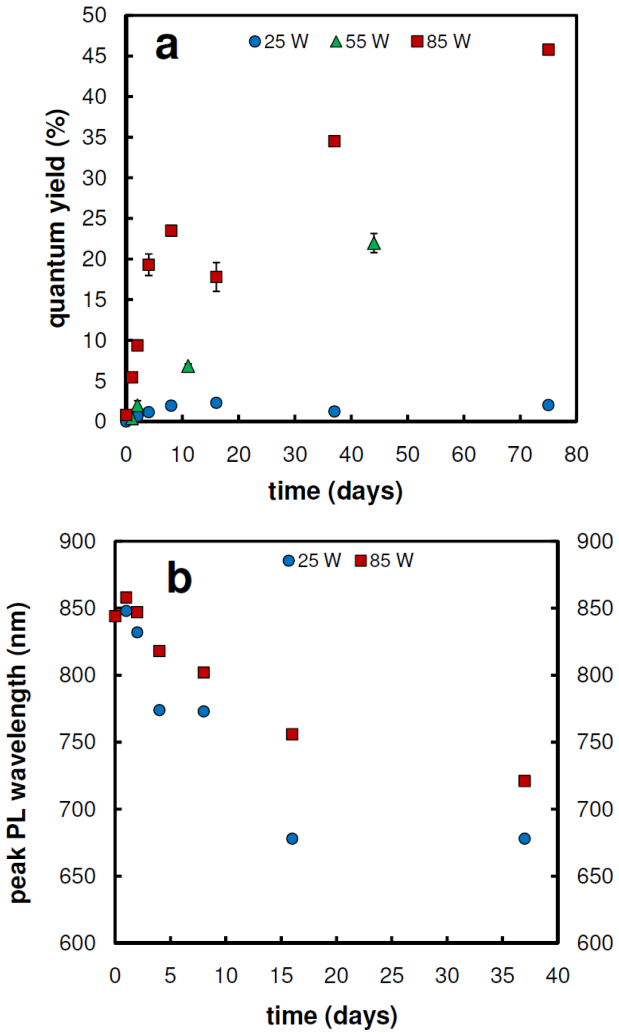

Figure 2.5: PL quantum yields of nanoparticle samples measured over time. The samples were unfunctionalized and allowed to oxidize, which acts to increase the QY of the crystalline (85W and 55W) samples, but has little pronounced effect on the amorphous (25W) sample. (a) Quantum yield; (b) peak PL wavelength.

The 25 W sample characterized as amorphous consistently displayed low QY despite experiencing the same oxidation conditions as the 85 W sample. Hence, the freestanding a-NPs, even after surface oxidation, do not exhibit high-efficiency PL as was reported in other work.[15,29] Again, it is not possible to determine whether the weak PL of this sample originates from the oxidized a-NPs or from a very small fraction of NCs that

remain undetectable by Raman scattering and XRD. However, the fact that the luminescence spectrum shows comparable blueshift of the peak PL as the highly crystalline 85 W sample suggests that emission in fact originates from a small fraction of NCs in the 25W sample. As above, while this measurement is not entirely unambiguous, we can use it to define an upper bound for the absolute PL QY of oxidized a-NPs of about 2%. This is significantly less efficient than the QY of oxidized Si NCs, which ranges as high as 45%—a number consistent with observations in earlier studies.[5]

It is likely that the properties of the oxide used in Refs. [15,29] are different from the native oxide formed at room temperature in our work. Hence, it is difficult to draw direct comparisons to those studies. However, for the free-standing silicon a-NPs produced in this work high-efficiency PL was not observed. The upper bound for the absolute PL QY was found to be < 2% regardless of surface functionalization.

2.4 Conclusions

In this chapter, we studied the photoluminescence efficiency of free-standing silicon NCs and a-NPs. The crystallinity of silicon nanoparticles made in a nonthermal plasma reactor may be tuned simply by adjusting the input synthesis power. For our specific experimental setup, at powers greater than 55 W, samples with high crystallinity are obtained, whereas powers lower than 55 W yield primarily a-NPs. The surfaces of Si NCs and a-NPs were treated with two different surface functionalizations: the assembly of organic alkene monolayers through hydrosilylation and the coating of the surfaces through native oxide formation. Regardless of surface functionalization, the a-NPs

synthesized in the plasma reactor do not exhibit high-efficiency photoluminescence, while NCs produced routinely exhibit PL QYs greater than 40%. All a-NP samples showed PL QY less than 2%. This result defines an upper bound for the absolute QY of the free-standing silicon a-NPs studied in this work. However, as the a-NP PL was found to be much weaker but similar in wavelength and temporal evolution to that of the silicon NC samples, we suggest that the a-NP sample PL in fact originates from a small fraction of NCs that is not detected by XRD or Raman scattering. This would imply that the intrinsic absolute QY of silicon a-NPs is in fact even smaller than the 2% defined as upper bound.

References

(1) Canham, L. T. *Applied Physics Letters* **1990**, *57*, 1046-1048.

(2) Cullis, A. G.; Canham, L. T. *Nature* **1991**, *353*, 335-338.

(3) Delerue, C.; Allan, G.; Lannoo, M. *Physical Review B* **2001**, *64*.

(4) Brus, L. E.; Szajowski, P. F.; Wilson, W. L.; Harris, T. D.; Schuppler, S.; Citrin, P. H. *Journal of the American Chemistry Society* **1995**, *117*, 2915-2922.

(5) Ledoux, G.; Gong, J.; Huisken, F.; Guillois, O.; Reynaud, C. *Applied Physics Letters* **2002**, *80*, 4834-4836.

(6) Walters, R. J.; Kalkman, J.; Polman, A.; Atwater, H. A.; de Dood, M. J. A. *Physical Review B* **2006**, *73*.

(7) Holmes, J. D.; Ziegler, K. J.; Doty, R. C.; Pell, L. E.; Johnston, K. P.; Korgel, B. A. *Journal of the American Chemistry Society* **2001**, *123*, 3743-3748.

(8) Sankaran, R. M.; Holunga, D.; Flagan, R. C.; Giapis, K. P. *Nano Letters* **2005**, *5*, 537-541.

(9) Jurbergs, D.; Rogojina, E.; Mangolini, L.; Kortshagen, U. *Applied Physics Letters* **2006**, *88*.

(10) Mangolini, L.; Jurbergs, D.; Rogojina, E.; Kortshagen, U. *Journal of Luminescence* **2006**, *121*, 327-334.

(11) Mangolini, L.; Thimsen, E.; Kortshagen, U. *Nano Letters* **2005**, *5*, 655-659.

(12) Credo, G. M.; Mason, M. D.; Buratto, S. K. *Applied Physics Letters* **1999**, *74*, 1978-1980.

(13) Yu, W.; Zhang, J. Y.; Ding, W. G.; Fu, G. S. *European Physical Journal B* **2007**, *57*, 53-56.

(14) Wang, Y. Q.; Chen, W. D.; Liao, X. B.; Cao, Z. X. *Nanotechnology* **2003**, *14*, 1235-1238.

(15) Pi, X. D.; Zalloum, O. H. Y.; Roschuk, T.; Wojcik, J.; Knights, A. P.; Mascher, P.; Simpson, P. J. *Applied Physics Letters* **2006**, *88*.

(16) Park, N.; Kim, T.; Park, S. *Applied Physics Letters* **2001**, *78*, 2575-2577.

(17) Park, N.; Choi, C.; Seong, T.; Park, S. *Physical Review Letters* **2001**, *86*, 1355-1357.

(18) Molinari, M.; Rinnert, H.; Vergnat, M. *Europhysics Letters* **2004**, *66*, 674-679.

(19) Irrera, A.; Iacona, F.; Crupi, I.; Presti, C. D.; Franzo, G.; Bongiorno, C.; Sanfilippo, D.; Di Stefano, G.; Piana, A.; Fallica, P. G.; Canino, A.; Priolo, F. *Nanotechnology* **2006**, *17*, 1428-1436.

(20) Boninelli, S.; Iacona, F.; Franzo, G.; Bongiorno, C.; Spinella, C.; Priolo, F. *Journal of Physics: Condensed Matter* **2007**, *19*.

(21) Zhu, X. -.; Boiadjiev, V.; Mulder, J. A.; Hsung, R. P.; Major, R. C. *Langmuir* **2000**, *16*, 6766-6772.

(22) Mangolini, L.; Jurbergs, D.; Rogojina, E.; Kortshagen, U. *physics status solidi (c)* **2006**, *3*, 3875-3978.

(23) Mangolini, L.; Kortshagen, U. *Physical Review E* **2009**, *79*.

(24) Tripathi, V.; Nazrul Islam, M.; Mohapatra, Y. N.; Roca i Cabarrocas, P. *The European Physical Journal Applied Physics* **2007**, *39*, 203-209.

(25) Sirenko, A. A.; Fox, J. R.; Akimov, I. A.; Xi, X. X.; Ruvimov, S.; Liliental-Weber, Z. *Solid State Communications* **2000**, *113*, 553-558.

(26) Kapaklis, V.; Politis, C.; Poulopoulos, P.; Schweiss, P. *Applied Physics Letters* **2005**, *87*.

(27) Buriak, J. M. *Chemical Reivews* **2002**, *102*, 1272-1308.

(28) Zunger, A.; Wang, L. *Applied Surface Science* **1996**, *102*, 350-359.

(29) Rinnert, H.; Vergnat, M.; Marchal, G.; Burneau, A. *Applied Physics Letters* **1998**, *72*, 3157-3159.

3. Effects of afterglow injection

Note: much of this chapter has been submitted to the journal *Advanced Functional Materials* by R. J. Anthony, D. J. Rowe, M. Stein, J. Yang, and U. Kortshagen. At the date of this thesis submission, the manuscript has not been accepted or returned with reviewer comments.

3.1 Preface

For some time, members of the Kortshagen laboratory have been synthesizing silicon nanocrystals using a plasma reactor nearly identical to the reactor (called the L122 reactor) used for this thesis. This separate reactor, located in the Univeristy of Minnesota's Nanofabrication Center (NFC) Area 1, also uses silane gas diluted with argon for nanocrystal synthesis. The NFC reactor is successful at producing crystalline silicon particles *en masse*, at rates of >50mg/hr (compared to ~10mg/hr in the L122 reactor), as it has the capability to flow much higher volumes of silane into the reactor. In addition, the NFC reactor is equipped with dopant gases which can be used to produce *n*- and *p*- doped SiNCs.

With its amplified collection rate and doping capabilities, the NFC reactor would seem to be the ideal instrument for producing high yields of photoluminescent silicon nanocrystals to be used in the hybrid organic/inorganic LED, solar cells, and other applications. However, even when exact recipes for high QY nanocrystals from the L122 reactor are copied as closely as possible in the NFC reactor, the SiNCs do not perform as well optically as those made in the L122 reactor. There is one difference between the two reactors, though, which leads to an important recipe amendment when trying to share synthesis parameters: the NFC reactor is not equipped with hydrogen gas. Thus, any

recipes calling for sidearm injection of hydrogen have to be altered for the NFC reactor to omit this flow.

When he constructed the current configuration and recipe for the L122 reactor, Dr. Lorenzo Mangolini stated that the inclusion of hydrogen as a sidearm injection gas would quench the plasma and halt the growth of silicon nanoparticles, lending an added degree of control over the size of the SiNCs.[1] The exact effect of the hydrogen injection on SiNC properties was not known. However, given the discrepancy in PL QYs for SiNCs made in L122 and in the NFC reactor, we surmised that the hydrogen must be the key in obtaining high-QY photoluminescence from plasma-produced silicon nanocrystals. A few preliminary studies in which argon was substituted for hydrogen in the injection region indicated that the hydrogen was indeed a key parameter for the SiNCs. Hence, a more detailed study of the influence of gas injection on the luminescence properties of SiNCs was undertaken, in order to definitively show the effect of hydrogen on the SiNCs and to pinpoint the exact reasons that hydrogen injection is important for SiNC PL. A note: some additional supporting information for this chapter can be found in Appendix B.

3.2 Introduction

During the last two decades, silicon nanocrystals (SiNCs) have gathered much interest due to their tunable, efficient luminescence properties. Light emission from SiNCs has many potential applications, from use in electroluminescent structures for communication technology to use as biological lumophores.[2-6] Understanding the

synthesis and processing conditions that lead to high photoluminescence (PL) intensity and efficiency is crucial to many applications relying on SiNC luminescent properties.

Nonthermal plasmas have been shown to be capable of producing SiNCs with high photoluminescence quantum yields (PL QY). SiNCs functionalized with alkene organic ligands have been demonstrated to exhibit PL QYs exceeding 60%.[7] However, reports of PL QYs of plasma synthesized SiNCs have been highly inconsistent in the literature or not even included. [8-12] This suggests that an important aspect in the synthesis of high PL QY SiNCs has so far not been identified. In this study, we demonstrate for the first time the importance of the conditions in the post-synthesis, afterglow region of the plasma, which to date have not been discussed in the literature. In particular, the mechanisms by which hydrogen injection into the afterglow of the nonthermal synthesis plasma leads to high efficiency PL had not been understood.

Hydrogen has been known to play an important role for the PL QY of SiNCs for quite a while. For example, Cheylan *et al.*[13] showed that hydrogen passivation of SiNCs embedded in SiO_2 improves the PL intensity of the nanocrystals. Similarly, Pellegrino *et al.* [14] showed that hydrogenation of SiNCs in silica can lead to decreases in dangling bonds and a corresponding PL enhancement. Hao and Shen[15] found that annealing of SiNCs in different gaseous environments, such as argon, hydrogen, and oxygen, produced different and identifiable PL characteristics. For SiNCs synthesized in a nonthermal plasma, Holm and Roberts[16] studied the role of the plasma environment on the structure and surface chemistry of the particles, but did not correlate these results with PL measurements. For SiNCs synthesized in a microplasma, Nozaki *et al.*[10] uncovered a

relationship between the inclusion of hydrogen in the microplasma and the luminescence peak and intensity of the nanocrystals.

3.3 Experimental details

Here, we study the relationship between the overall PL QY and the conditions in different afterglow environments. This is accomplished by injecting different gases into the afterglow of the synthesis plasma in the plasma reactor shown in Figure 3.1. In the primary plasma region, SiNCs are synthesized by flowing 13 sccm of 5% silane in helium and 35 sccm of argon into the reactor and exciting a plasma using 75-80 W of 13.56 MHz rf power. Downstream of the primary plasma particle synthesis region, there is an inlet that allows gas to be injected into the afterglow of the plasma. The total pressure in the synthesis region was held constant at 1.4 Torr, using a pressure-controlled butterfly valve located between the reactor and the vacuum pump.

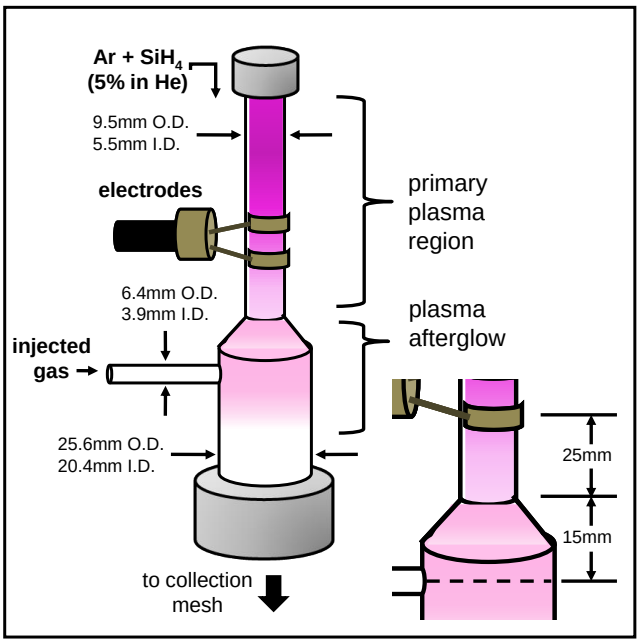

Figure 3.1: Schematic of the plasma reactor, including dimensions.

After passing through the afterglow region, the SiNCs were collected via diffusion on a stainless steel mesh at the exit of the reactor and transferred into a Schlenk line, where they were functionalized under air-free conditions with 1-dodecene in a hydrosilylation reaction, as described in detail in Ref. 7. SiNCs were mixed with a 5:1 v/v solution of mesitylene and 1-dodecene. Following ~2 hours of heating at 215°C under nitrogen-purged refluxing conditions, the SiNCs formed a clear colloidal solution.

3.4 Results

3.4.1 Argon vs. hydrogen injection

In an initial study, we varied the composition of the injected gas from 0% hydrogen to 100% hydrogen on a volume basis with argon as the balance gas, keeping the

partial pressure of injected gas mixture constant throughout. After synthesis but before hydrosilylation, the particle surfaces were studied using a Bruker Alpha Fourier Transform Infrared (FTIR) spectrometer in diffuse reflectance (DRIFTS) mode. After hydrosilylation, the PL was measured using a light emitting diode at 395-400 nm as excitation source and an Ocean Optics, Inc., USB2000 spectrometer equipped with an integrating sphere. The QY was calculated by comparing absorption and emission from the PL spectra.[17] The PL QYs from the SiNCs are shown in Figure 3.2a, plotted against fractional volume flow (%H_2) in the afterglow injection gas. For samples produced with 0% H_2, i.e. exclusively argon in the injection flow, the PL QY was close to 13%, and as

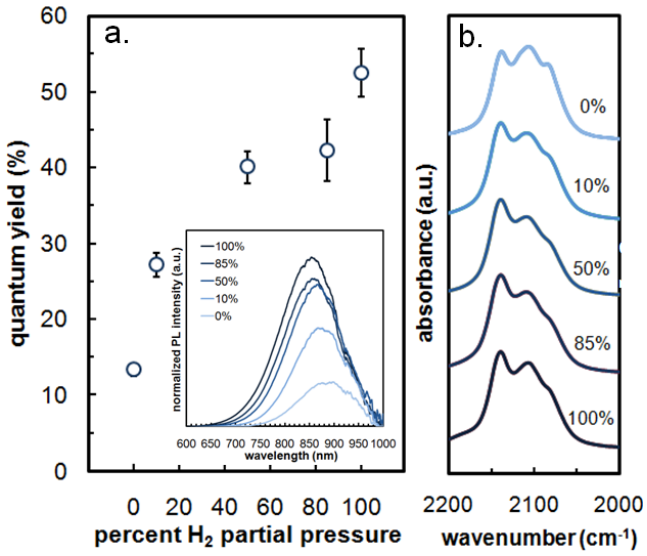

Figure 3.2: PL (a) and FTIR (b) results from hydrogen/argon injection experiments. PL QY results are plotted against %H_2 injection gas in a, with the inset showing PL curves. Error bars represent the standard deviations of the measurements. FTIR spectra of the samples, displaying the Si-H_x stretch region, are shown in b.

the $\%H_2$ was increased, the QY rose to a peak level of 52% for pure hydrogen injection. This is a clear indication that hydrogen injection into the plasma afterglow region is important for the synthesis of high-QY SiNCs. The absorption-normalized PL spectra for these samples are plotted as the inset of Fig. 3.2a.

3.4.2 Possible effects of hydrogen injection

The results of this study provoke the question as to the physical role of the injection of hydrogen on the ultimate PL QY of SiNCs in the nonthermal plasma reactor. A simple analysis of binary diffusion of hydrogen in argon shows that hydrogen injected into the afterglow is unlikely to diffuse against the gas flow into the primary plasma region. The residence time of the gas traveling from the end of the primary plasma region to the injection site due to convection is ~4.4 ms, while the typical back diffusion time of hydrogen over the same distance is ~9.5 ms. Hence we assume that the conditions in the primary plasma region are barely, if at all, affected by the injection of the gas into the afterglow region. The significant change in the PL QY should thus be a direct consequence of the changes in the conditions in the afterglow plasma region. The details of the calculations for diffusion time and convection time can be found in the supplemental section.

In most nanocrystal systems, the loss of PL efficiency is associated with the presence of nonradiative surface states. Remediation of surface states often leads to improved PL QY.[18] In figure 3.2b we study the surface coverage of SiNCs with hydride species, since hydrogen is known to be an excellent passivating agent for silicon surface

states.[19,20] The infrared absorption features around 2,100 cm^{-1} correspond to three different silicon hydride surface species: SiH (2,086 cm^{-1}), SiH_2 (2,112 cm^{-1}), and SiH_3 (2,136 cm^{-1}).[21] Figure 3.2b demonstrates the general trend that injection of additional hydrogen into the afterglow plasma region leads to an increased surface coverage with SiH_3 and a relative decrease of the concentration of SiH groups. (Note that even in the case of 0%H_2, there is a significant amount of hydrogen present from the SiH_4 precursor.) We hypothesize that the increased coverage with SiH_3 species is a general indication of a more complete termination of SiNC surface states, giving rise to the higher PL QY observed from the SiNCs after hydrosilylation. To provide evidence for this, we used a Bruker Continuous Wave EleXsys E500 electron paramagenetic resonance (EPR) spectrometer to measure the signal from dangling bond defects, also known as D-defects, of Si NCs with both hydrogen and argon injection. The D-defects are characteristic of disorder in a Si matrix, and are assigned to the bond sites at the surface of the SiNCs missing hydrogen passivation.[22] All samples were prepared and measured under air-free conditions so that D-defects dominated the signal while defects related to dangling bonds at the SiNC/silicon oxide interface were not observed. As shown in Figure 3.3 the EPR signal intensity is much lower for the SiNCs prepared with hydrogen injection than for the SiNCs made with argon injection, lending evidence to our hypothesis that hydrogen injection leads to a more efficient termination of dangling bond states.

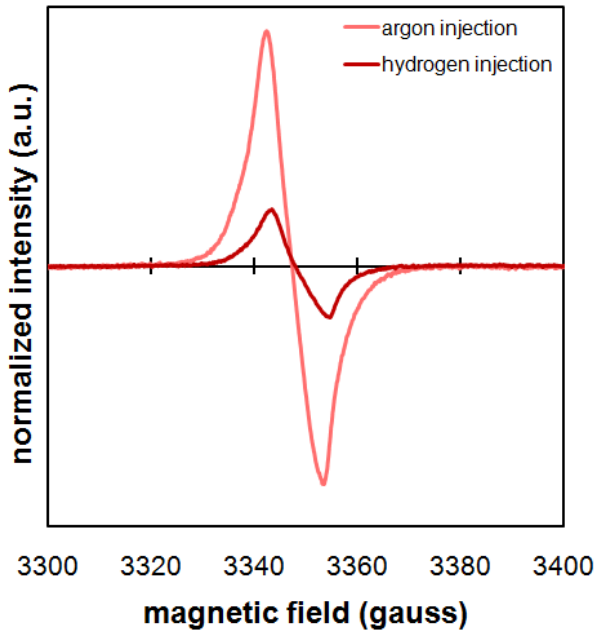

Figure 3.3: EPR spectra of SiNCs synthesized with hydrogen and argon injection.

We further hypothesize that the stronger coverage with SiH_3 species in the case of increased hydrogen injection may be due to two different mechanisms:

1. The faster quenching of the SiNC temperature as the SiNCs leave the synthesis plasma zone. As discussed by Mangolini and Kortshagen,[23] SiNCs immersed in a plasma are subjected to a range of energetic surface reactions that heat the SiNCs to temperatures of several hundred Kelvin beyond the gas temperature. Since surface hydrogen desorbs from different surface groups at different temperatures, the surface hydrogen coverage may be used as an empirical measure of the particle temperature history. Holm and Roberts showed that surface hydrogen first desorbs from SiH_3 groups between 400-500 °C, while it persists to temperatures of up to 650 °C in SiH_2 and more than 700 °C in SiH groups.[24] The increased SiH_3 coverage with increased

hydrogen injection may thus indicate faster cooling of the SiNCs emerging the synthesis plasma, due to the higher thermal conductivity of hydrogen compared to that of argon.

2. Improved SiNC hydrogen coverage due to an increased flux of atomic hydrogen species. The injection of hydrogen may lead to the production of additional atomic hydrogen species, which may insert themselves into surface dangling bonds.[10] The increased hydrogen coverage would be reflected in a higher concentration of more saturated surface hydrides.

3.4.3 Other gas injection scenarios

In order to test our hypothesis that these two mechanisms indeed play a role and to assess their relative importance, we performed additional experiments in which different gases were injected into the plasma afterglow. For one set of experiments, we injected helium (He), which has similar thermal conductivity and specific heat capacity compared to hydrogen but which does not bond to silicon surface sites. In the second set of experiments, we injected deuterium (D_2) which has lower thermal conductivity compared to hydrogen but is chemically almost identical and shares hydrogen's ability to passivate silicon surface states. Due to the larger mass of deuterium, the SiD_x stretch modes occur at lower wavenumbers than the SiH_x modes, allowing us to easily verify the reactions of D_2 species with the SiNC surfaces in the afterglow through FTIR studies.

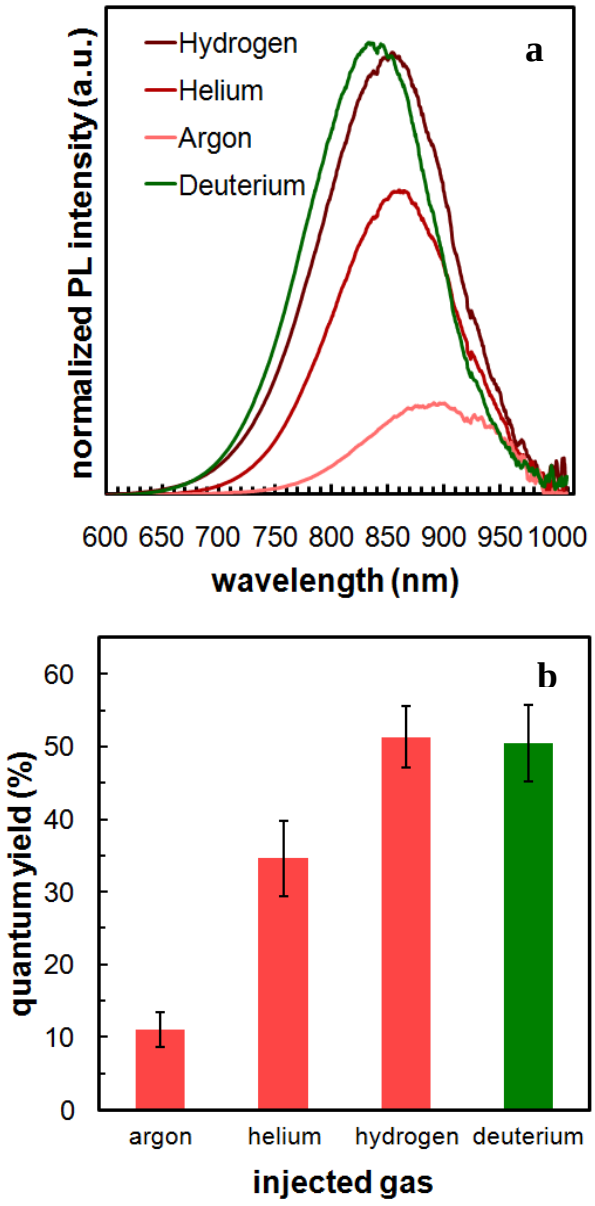

Figure 3.4: PL spectra (a) and quantum yields (b) for different injection gas schemes. Error bars reflect the root-sum-square of the individual sample measurement and the standard deviation among samples.

A summary of the effect of all different injection gases on the SiNC PL QYs is plotted in Figure 3.4. Argon gas injection leads to the lowest PL performance with ~12%. The injection of helium leads to a significant increase in the PL QY to ~35%,

which is, however, lower than the PL QY of ~52% achieved with hydrogen. This result suggests that the fast quenching of the particle temperature through injection of a suitable gas is important but is not the only factor in achieving a high quantum yield. The FTIR spectra shown in Figure 3.5 confirm that helium injection indeed leads to a higher SiH_3 concentration compared to argon, which is consistent with the SiNCs experiencing lower temperatures and reduced hydrogen desorption from SiH_3 groups in the afterglow with helium injection. However, the SiH_3 concentration is not as high as that obtained with hydrogen injection.

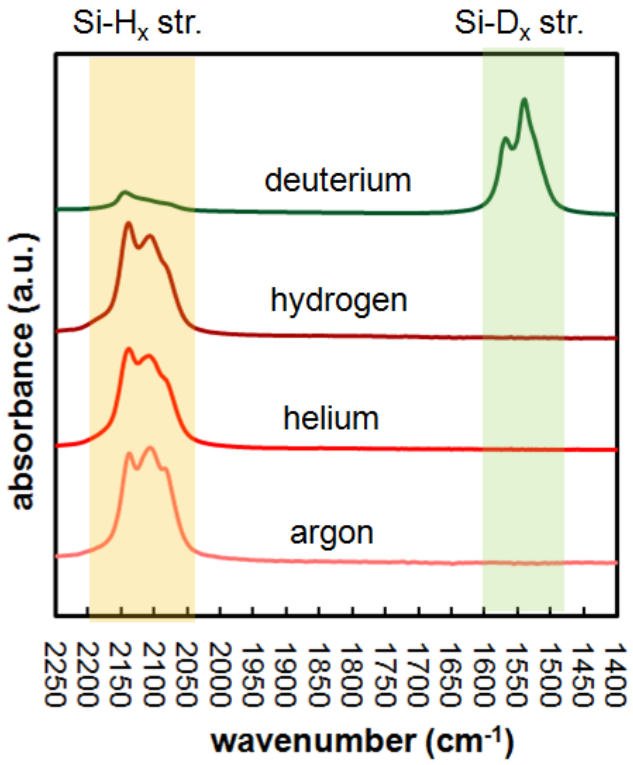

Figure 3.5. FTIR spectra for different injection gas schemes. The Si-H_x and Si-D_x stretching vibration regions are highlighted.

The injection of deuterium leads to an almost identical PL QY as the injection of hydrogen. It is interesting to observe in Figure 3.5 that the SiH_x stretch modes are almost completely replaced by SiD_x modes. This suggests that even though the plasma afterglow is often considered as a region of recombining plasma with limited chemical activity, a significant amount of deuterium is dissociated such that almost every H atom bonded to a silicon surface site is replaced by a D atom. This observation confirms that a significant flux of H or D atoms reaches the SiNC surfaces in the afterglow which, combined with the fast quenching of the particle temperature, leads to the highest surface coverage with H (or D) atoms.

The studies presented above demonstrate that the PL QY of SiNCs produced in nonthermal plasmas sensitively depends on the conditions in the afterglow plasma following the main plasma synthesis zone. Measures to achieve the highest possible surface coverage with hydrogen lead to the highest PL QY. In Appendix B, we present additional data of experiments, in which no gas was injected into the afterglow or in which hydrogen was injected further downstream of the afterglow plasma. In both cases, a lower quantum yield than with hydrogen injection directly into the afterglow is achieved.

3.5 Conclusions

In summary, we have examined the role of the afterglow plasma on the PL QY achieved with nonthermal plasma synthesized SiNCs. FTIR studies suggest that the highest SiNC PL QY is achieved with the most complete surface coverage of SiNCs with

hydrogen or deuterium. The comparison of different injection gases suggests that this is achieved through a combination of two mechanisms: 1) the fast quenching of the SiNC temperature through the gases injected into the afterglow plasma and 2) the exposure of SiNC surfaces to a flux of hydrogen or deuterium atoms, which terminate dangling bond states. We observed that the conditions in the afterglow can modify the SiNC PL QY by a factor of almost five. Hence it is important to carefully design the afterglow plasma region in order to achieve the highest PL QY from plasma synthesized SiNCs.

The authors are grateful to Mr. Ryan Mello for his support with EPR measurement.

References

(1) Mangolini, L. Non-thermal plasma synthesis and passivation of luminescent silicon nanocrystals. Ph.D. Thesis, University of Minnesota: Minneapolis, MN, 2007.

(2) Wang, M.; Anopchenko, A.; Marconi, A.; Moser, E.; Prezioso, S.; Pavesi, L.; Pucker, G.; Bellutti, P.; Vanzetti, L. *Physica E* **2009**, *41*, 912-915.

(3) Yanagisawa, S.; Sato, K.; Hirakuri, K. *Thin Solid Films* **2007**, *515*, 7990-7993.

(4) Cheng, K.; Anthony, R.; Kortshagen, U. R.; Holmes, R. J. *Nano Letters* **2011**, *11 (5)*,1952-1956.

(5) Biaggi-Labiosa, A.; Sola, F.; Resto, O.; Fonseca, L. F.; Gonzalez-Berrios, A.; De Jesus, J.; Morell, G. *Nanotechnology* **2008**, *19*.

(6) Erogbogbo, F.; Yong, K.; Roy, I.; Xu, G.; Prasad, P. N.; Swihart, M. T. *ACS Nano* **2008**, *2*, 873-878.

(7) Jurbergs, D.; Rogojina, E.; Mangolini, L.; Kortshagen, U. *Applied Physics Letters* **2006**, *88*.

(8) Sankaran, R. M.; Holunga, D.; Flagan, R. C.; Giapis, K. P. *Nano Letters* **2005**, *5*, 537-541.

(9) Beard, M. C.; Knutsen, K. P.; Pingrong, Y.; Luther, J. M.; Song, Q.; Metzger, W. K.; Ellingson, R. J.; Nozik, A. J. *Nano Letters* **2007**, *7*, 2506-2512.

(10) Nozaki, T.; Sasaki, K.; Ogino, T.; Asahi, D.; Okazaki, K. *Nanotechnology* **2007**, *18*.

(11) Gupta, A.; Swihart, M. T.; Wiggers, H. *Advanced Functional Materials* **2009**, *19*, 696-703.

(12) Shen, P.; Uesawa, N.; Inasawa, S.; Yamaguchi, Y. *Journal of Materials Chemistry* **2010**, *20*, 1669-1675.

(13) Cheylan, S.; Elliman, R. G. *Applied Physics Letters* **2001**, *78*, 1912-1914.

(14) Pellegrino, P.; Garrido, B.; Garcia, C.; Ferre, R.; Moreno, J. A.; Morante, J. R. *Physica E* **2003**, *16*, 424-428.

(15) Hao, H. L.; Shen, W. Z. *Nanotechnology* **2008**, *19*.

(16) Holm, J.; Roberts, J. T. *Journal of Vacuum Science and Technology* **2010**, *28*, 161-169.

(17) Mangolini, L.; Jurbergs, D.; Rogojina, E.; Kortshagen, U. *Journal of Luminescence* **2006**, *121*, 327-334.

(18) Hines, M. A.; Guyot-Sionnest, P. *Journal of Physical Chemistry* **1996**, *100*, 468-471.

(19) Min, K. S.; Shcheglov, K. V.; Yang, C. M.; Atwater, H. A.; Brongersma, M. L.; Polman, A. *Applied Physics Letters* **1996**, *69*, 2033-2035.

(20) Seraphin, A. A.; Ngiam, S.; Kolenbrander, K. D. *Journal of Applied Physics* **1996**, *80*, 6429-6433.

(21) Marra, D. C.; Edelberg, E. A.; Naone, R. L.; Aydil, E. S. *Journal of Vacuum Science and Technology A* **1998**, *16*, 3199-3210.

(22) Stutzmann, M.; Biegelsen, D. K. *Physical Review B* **1989**, *40*, 9834-9840.

(23) Mangolini, L.; Kortshagen, U. *Physical Review E* **2009**, *79*.

(24) Holm, J.; Roberts, J. T. *Journal of Physical Chemistry C* **2009**, *113*, 15955-15963.

4. Silyl effusion from silicon nanocrystals

4.1 Introduction

The efficient and tunable luminescence from quantum-confined silicon nanocrystals (SiNCs) has attracted much attention in recent years. A few characteristics that set SiNCs apart from other luminescent quantum dots are the silicon's abundance as well as its relatively low toxicity. Applications for SiNCs range from use as lumophores in biological tagging to emissive layers in electroluminescent devices.[1-4] Recently, a hybrid organic / SiNC light-emitting device showed peak external quantum efficiency of 8.6% in the near infrared spectral region.[3] While organic semiconductors can perform quite well in the visible region, SiNCs offer the advantage of efficient luminescence in the infrared range, potentially enabling the use of hybrid LEDs for remote communications. In addition, the infrared emission and ultraviolet absorption of SiNCs makes them attractive for use in biological applications, as these wavelengths are compatible with transmission through tissue.

One of the steps in optimizing SiNC–based applications is to fully understand the mechanisms affecting luminescence from the nanocrystals. By revealing the effects of surface treatments and particle quality on the SiNC emission, these nanocrystals can be engineered to exhibit efficient luminescence, enabling SiNCs to compete with other light-emitting device structures. Among the many issues controlling nanocrystal luminescence efficiency is the role of dangling bonds at the nanocrystal surface. It is understood that passivation of the surface silicon atoms can eliminate dangling bonds and lead to

enhanced emission properties.[5-16] Methods of passivation include annealing and attachment of functional groups to the SiNC surfaces.

Mangolini, *et al.* [5] explored the use of a dual-plasma reactor to synthesize SiNCs and then graft alkenes onto the nanocrystal surfaces in-flight. An interesting finding from this work was that while the alkene chains were successfully bound to nanocrystal surfaces in the in-flight functionalization step, a subsequent heating of the functionalized SiNCs was required in order to raise the photoluminescence (PL) quantum yield (QY) of the nanocrystals. Simultaneously, this heating step appeared to cause a reduction in surface dangling bonds as seen in electron paramagnetic spin resonance (EPR) spectroscopy as well as a change in surface hydrogen as seen in Fourier-transform infrared spectroscopy (FTIR) measurements. The implication from this study is that attachment of ligands is not solely responsible for enhanced QY from these SiNCs, and that the heating of the functionalized nanocrystals plays an important role in the defect densities and luminescence behavior of SiNC ensembles.

In this work, we examine the PL properties of SiNCs, produced in a nonthermal plasma reactor, upon annealing in inert atmosphere. The goal of our study is to pinpoint the effects of heating on the SiNCs from the perspective of defect density and surface hydride species. The effects of heating on SiNC surfaces is investigated using FTIR measurements, thermal desorption spectroscopy, and EPR spectroscopy, and is correlated to PL quantum yields of the nanocrystals.

4.2 Experimental details

The SiNCs in this experiment were produced in a low-pressure, non-thermal rf plasma reactor, as described previously in this thesis. The reactant gases used for these experiments were silane (5% in He) and argon, with an injection of hydrogen into the effluent of the plasma. The total gas flowrate was 130-150 sccm. The pressure in the reactor was 1.4 Torr and the nominal rf power was 75-90 W. A nitrogen-purged glove bag surrounding the plasma reactor allowed collection of the SiNCs in an air-free environment to prevent oxidation.

For steps involving boiling the SiNCs in solvent, the nanocrystals were immersed in anhydrous, degassed mesitylene using a N_2/vacuum schlenk line. Dry heating experiments were also performed in a nitrogen environment. FTIR data were taken using a Nicolet Series II Magna-IR System 750 FTIR. Electron paramagnetic spin resonance (EPR) was carried out on a Bruker CW EleXsys E500 EPR spectrometer. Photoluminescence measurements were taken using an Ocean Optics, Inc. USB2000 spectrometer and an integrating sphere.

4.3 Heating of SiNCs: FTIR and PL

We first tried heating the Si NCs in neat mesitylene to examine the effects of heating on the photoluminescence of the samples. Upon heating to 160°C for 1 hour, the luminescence intensity of the nanocrystals was enhanced significantly, as shown in Figure 4.1a. This enhancement was achieved in the absence of functionalizing ligands, simply due to the heating of the nanocrystals: the dispersion was cloudy both before and

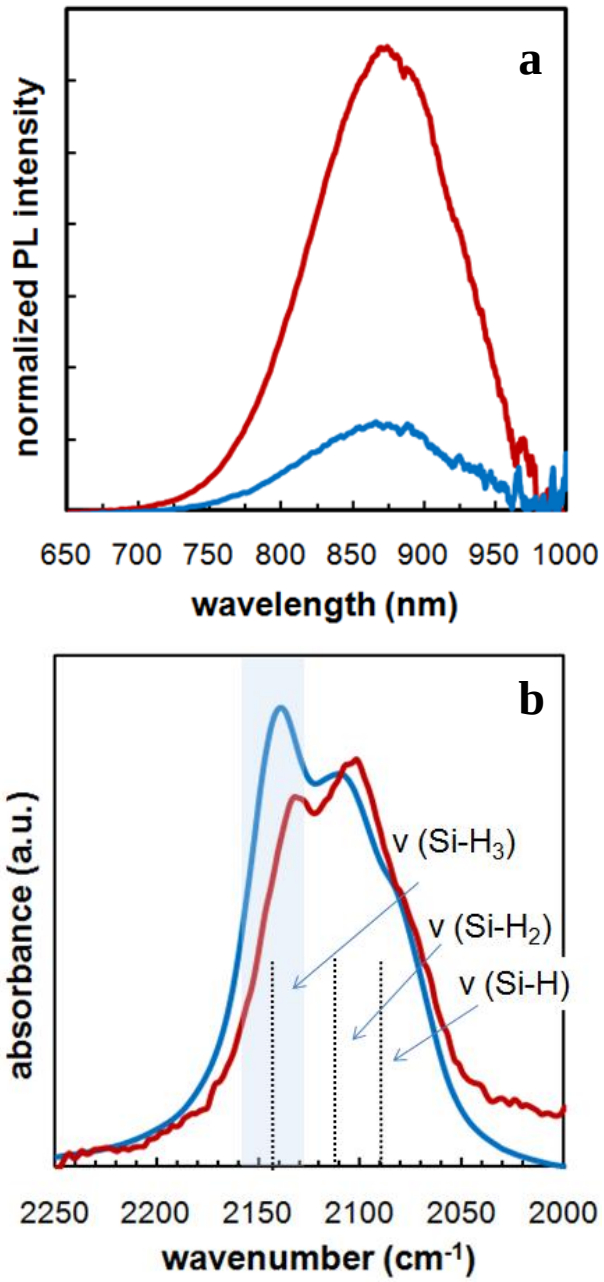

Figure 4.1: PL (a) and FTIR (b) from as-produced SiNCs (blue) and SiNCs refluxed in mesitylene to 160°C (red).

after this treatment. Upon examination of the surface bonds of the samples using FTIR spectroscopy, a slight change can be seen in the structure of the silicon tri-, di-, and monohydrides in the stretch vibration region between 2000 and 2200 cm^{-1}. For this study, we are assigning the peaks near 2,140 cm^{-1}, 2,110 cm^{-1}, and 2,080 cm^{-1} as stretching vibrations from $Si-H_3$, $Si-H_2$, and Si-H, respectively.[17] In the heated sample, the $Si-H_3$ peak is diminished when compared to the as-produced Si NC sample (Fig. 4.1b).

To watch the change in the SiNC surface during heating rather than simply before and after, we used a diffuse-reflectance FTIR setup equipped with a heater in a vacuum chamber in Professor Aydil's lab in the Chemical Engineering and Materials Science department. We placed SiNCs onto gold-coated silicon inside the chamber, pumped it

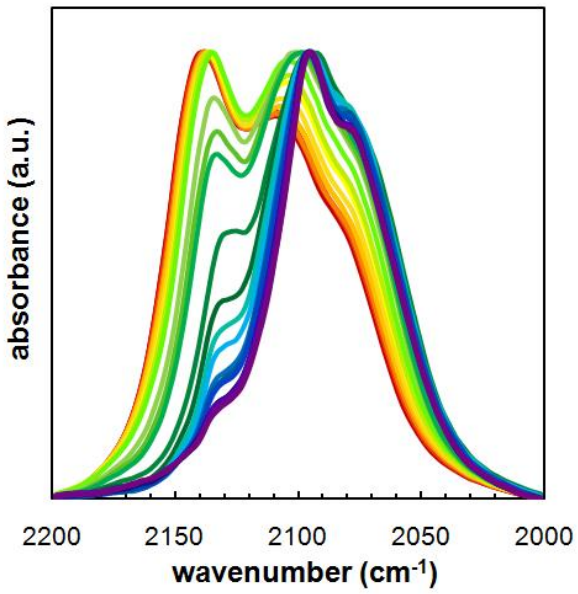

Figure 4.2: *In-situ* FTIR spectra ($Si-H_x$ region) of heated SiNCs. Red shows the as-produced sample, and as the colors move towards purple the temperature is increased to 550°C, with $\Delta T = 25°C$. Spectra are normalized to the highest point in the displayed region.

down to vacuum level, and then proceeded to heat the sample as we recorded FTIR spectra periodically. The sample was heated from room temperature to 550°C. The FTIR spectra from the Si-H_x stretching region are presented in Figure 4.2. During this heating, the shift in Si-H_x surface structure is clear to see, with a gradual reduction in tri-hydrides as heating progresses, accompanied by a shift to di- and mono-hydride coverage.

4.4 Electron paramagnetic spin resonance measurements

These experiments showed that heating the as-produced SiNCs leads to a reduction in Si-H_3 groups at the SiNC surface, and that the heating also increases the intensity of PL from the SiNCs. However, the relationship between these two features was unknown. Our next experiments were designed to identify the possible correlations between Si-H_x species at the SiNC surface and the intensity of PL from the samples. The study of Si-H_x and hydrogen diffusion on silicon surfaces is not a new one.[17-19] Marra *et al.* showed that silicon trihydrides on silicon nanoparticles can be the result of adsorption of SiH_3 on dangling bond sites, and that these trihydrides can be dissociated or removed at temperatures below 250°C.[17] The group of Kessels examined the radicals present near the substrate during thin-film nanocrystalline silicon growth in a low-pressure silane/argon/hydrogen plasma, and showed that the silicon trihydride radical is the most prevalent.[20] If the same is true for our nonthermal plasma reactor, the predominance of SiH_3 in the plasma could lead to adsorbed radicals on the nanoparticles' surfaces, creating dangling bonds and limiting the PL intensity from as-produced nanoparticles.

We suspected that the heating step may have caused a decrease in dangling bond density via reduction of the Si-H_x groups, leading to enhanced luminescence, and so we performed EPR on heated SiNCs in conjunction with PL measurements. For this study, we heated SiNCs under dry nitrogen conditions for 1 hour at 200°C, and then took EPR and PL measurements on both the as-produced and the heated samples. EPR is a spectroscopic technique used to identify and quantify dangling bonds based on the free electron energy level splitting in a magnetic field and the resulting resonance under applied microwave radiation. Specific types of free electrons, or dangling bonds, can be distinguished based on their resonance at a specific applied magnetic field and microwave radiation. The equation that governs the resonance of the free electrons is

$$\Delta E = h\nu = g * \mu_B * B$$

where ΔE is the spin-based energy splitting of the electrons, hν is the microwave radiation energy, g is the so-called g-value which is specific to the type of dangling bond, μ_B is the Bohr magneton, and B is the applied magnetic field. We have seen that the D-defect, which is associated with disorder in silicon, has a g-value of 2.0052, and that the P_b-defect found at Si-SiO_2 interfaces has a parallel and anti-parallel g-values of 2.0019 and 2.0086.[21] These two defects have resonances close enough to one another that the EPR signals are superimposed. The silyl radical ·SiH_3 has a g-value within spectroscopic range of these, at 2.0036,[22] and would likely have a signal which is superimposed on the D- and P_b defects as well. For the EPR instrument that we used in these experiments, we

kept the microwave radiation constant and scanned the magnetic field in the range where we expected to see the dangling bonds in silicon.

The heating again caused a significant increase in PL intensity, as seen in Fig. 4.3a. Concurrently, the overall dangling bond density from the Si NCs decreased notably after this heating step (Fig. 4.3b), which indicates that heating the nanocrystals indeed removes dangling bonds and may be responsible for the simultaneous increase in PL efficiency. This result was not entirely unexpected; Niesar *et al.* also showed a reduction in dangling bond density in silicon nanocrystals upon low-temperature heating, although that group did not examine photoluminescence from the SiNCs.[23] Here, we see that the EPR signal has changed from largely symmetric for the as-produced sample to more asymmetric following heating, indicating that the remaining defect signature is the asymmetric P_b-defect related to Si/SiO_2 rather than the symmetric resonance of the D defect.

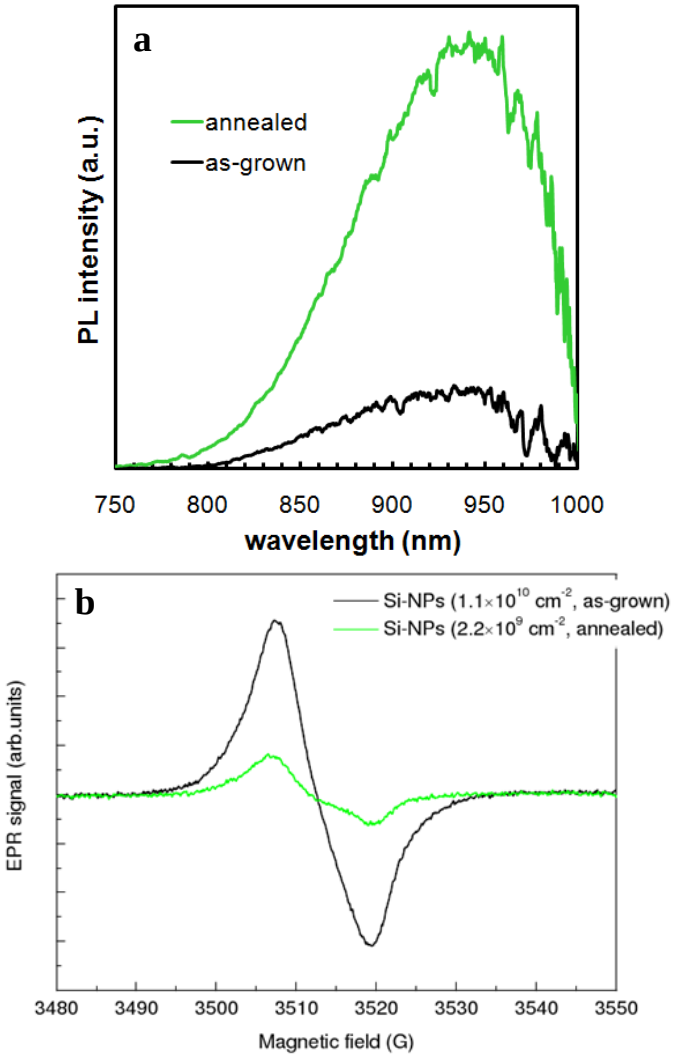

Figure 4.3: PL (a) and EPR (b) spectra from as-produced and heat-treated SiNCs. The PL intensity goes up concurrently with a decrease in the amplitude of the EPR signal. Many thanks to Dr. Rui Pereira for his help with the EPR measurement and analysis.

To break down the process even further, we performed *in-situ* heating/EPR and heating/PL measurements on the nanocrystals at a lower temperature of 125°C. The EPR sample was placed into the instrument cavity and heated to 125°C while recording the EPR signal approximately every 5 minutes. The amplitude of the EPR signal decreased gradually over the course of an hour until it reached a saturation value (Fig. 4.4a). In

previous experiments with Dr. Rui Pereira, we learned that the defect density of these nanocrystals does not increase or decrease over the course of a few hours, when

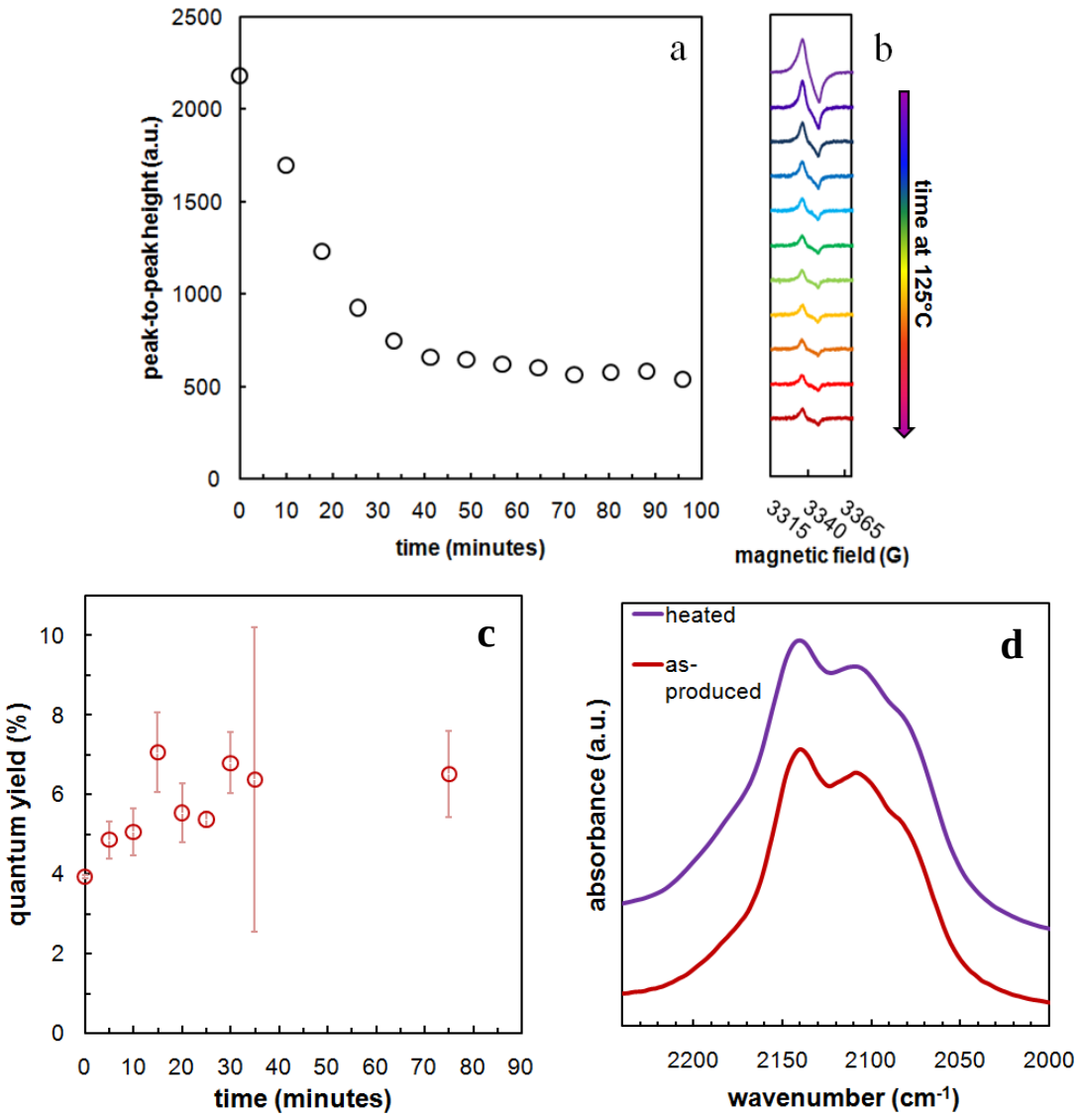

Figure 4.4: EPR signal amplitude (a) and spectral representation (b) from SiNCs as a function of *in-situ* heating time at 125°C. The PL QYs from an SiNC sample heated under the same conditions are shown in (c), and FTIR spectra of an as-produced sample and a sample heated to 125°C is pictured in (d). Error bars in the QY measurement reflect standard deviation.

measurements are conducted at room temperature. This indicates that the decrease in defect density that we see is due to heating. We expected to see a gradual increase in PL intensity with the SiNC sample heated and measured under the same conditions, if dangling bonds either as D-defects or as silyl radicals were creating non-radiative exciton decay pathways in the SiNCs. However, our PL experiments showed only a very slightly improved quantum yield for the heated sample compared to the initial value of quantum yield (Fig. 4.4c). Furthermore, the Si-H_x stretching vibration region for the nanocrystals heated to 125°C does not display a measureable change (Fig. 4.4d). In addition, analysis of the EPR signal from unheated SiNCs revealed that the as-produced nanocrystals exhibit approximately one dangling bond per 100 nanocrystals—a dangling bond density that is hard to imagine being responsible for a reduction in ensemble quantum yield. These experiments and analysis discount the hypothesis that a decrease in dangling bond density upon annealing, for these nanocrystals, is directly related to the increase in PL QY that we see.

4.5 Thermal desorption experiments

So far, we see that surface hydrogen is somehow altered in the heating process, provided the heating temperature is greater than 160°C—in addition, the PL QY goes up coincidentally with this surface change. However, rearrangement in surface bonds and PL increase have been decoupled from any reduction in EPR-active dangling bond density, as shown in the previous section. To try to understand the physical processes occurring at the SiNC surfaces, we performed temperature-programmed desorption

studies on the SiNCs. Thermal desorption studies have been well-used to examine the release of hydrogen and other species from silicon structures,[24-28] with peaks from effused hydrogen typically occurring between 300-400°C, and sometimes lower temperatures in the case of nanostructures. By using thermal desorption, we intended to study whether hydrogen is removed from the freestanding SiNCs at lower temperatures such as 160°C, or whether it simply shifts around, forming more stable bond configurations. SiNCs were collected as usual on a stainless steel mesh and then transferred to a glass microscope slide. The sample was loaded into a vacuum chamber equipped with a lamp heater and a residual gas analyzer (Stanford Research Systems RGA100). For control purposes, we also performed the experiments using a clean glass slide as the sample. The temperature of the sample, as measured using a thermocouple attached to the sample stage, was ramped from room temperature to 400°C at a rate of 10°C per minute with mass spectra from the RGA recorded every minute. The mass spectra from an SiNC sample and the control are shown in Figure 5a. We were initially interested to see the atomic and molecular hydrogen features in the mass spectra, seen as the lowest-mass peak around 1-2 amu. Thus, we were surprised to note that the most significant differences between the control spectrum and the sample spectrum came near 29-31 amu and 58-62 amu. These very notable peaks derive from silyls and disilyls— Si-H_x and Si_2-H_x. The signals for silyl groups begin to emerge between 100-200°C. The

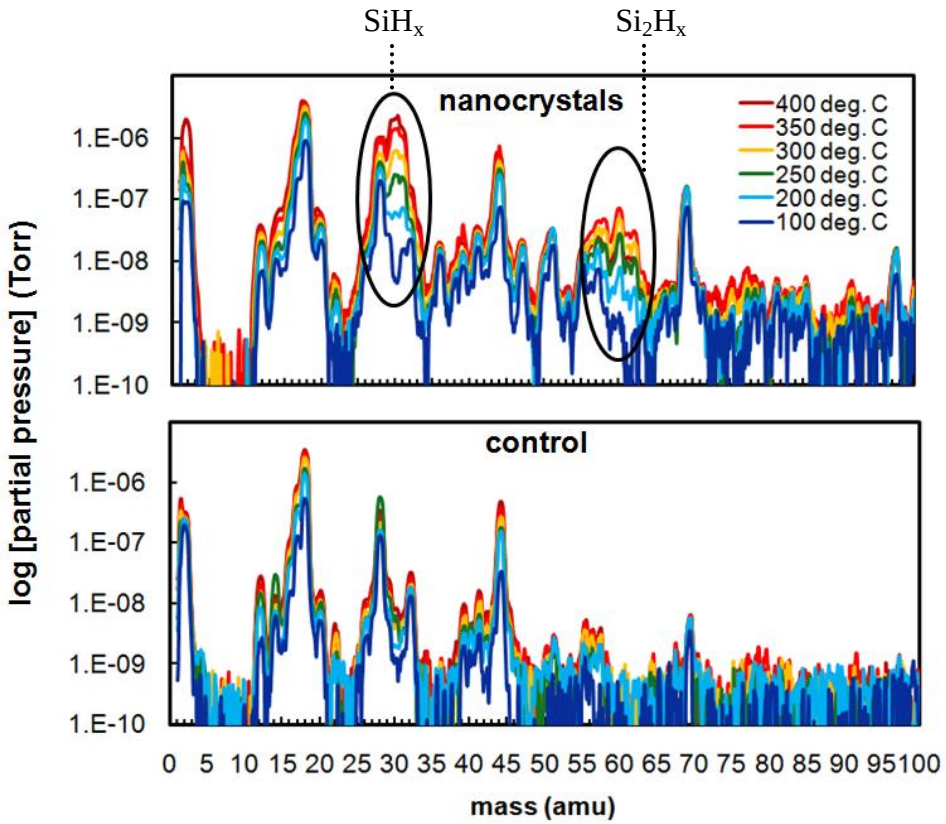

Figure 4.5: RGA mass spectra from SiNCs (top) shows a removal of Si-H_x groups beginning between 100-200°C. These peaks are not evident in the control mass spectra (bottom). Silyl peaks are circled in black.

silyl signal is still present at 400°C; however, by holding the sample at that temperature and recording a spectrum after 1, 5, an 10 minutes (Figure 6), we saw the signal fall off—demonstrating that the silyl groups are indeed effusing from the SiNC surface and evaporating away. It is likely that the multiple species of silicon hydrides we see removed from the SiNCs are primarily the result

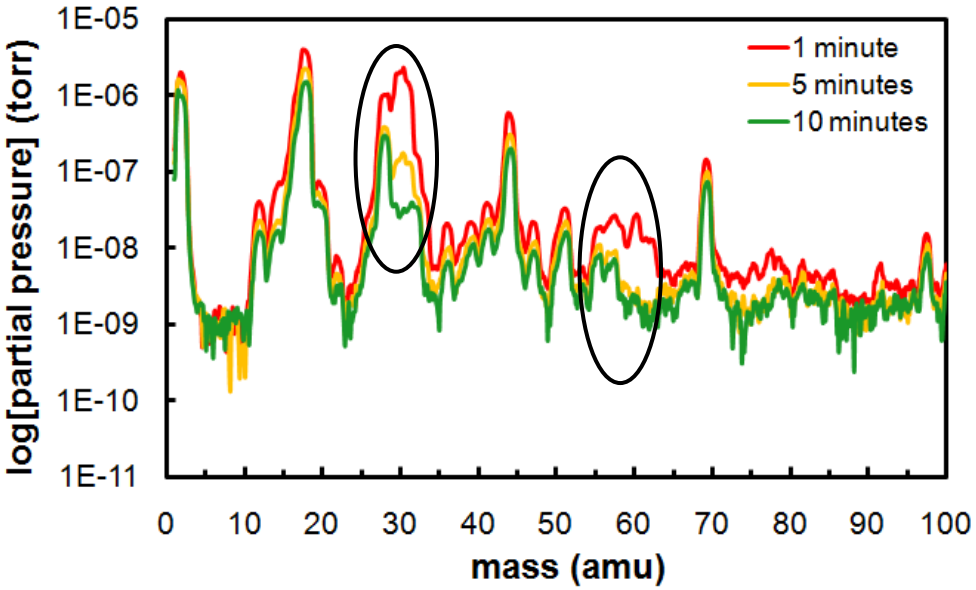

Figure 4.6: RGA mass spectra for sample held at 400°C. While silyl peaks (circled in black) are visible at 1 minute, they are reduced after 5 minutes and not visible above the noise after 10 minutes, demonstrating the removal of these groups during heating.

of Si-H_3 desorption: Martín *et al.* performed similar thermal desorption studies on nanostructured porous silicon and found that removal of silyl groups was due to Si-H_3 abstracting a nearby hydrogen, desorbing as silane, and then the silane decomposing in the gas phase prior to collection by the RGA filament.[29] As the Si-H_3 peak is the first hydride peak that we see diminishing in our FTIR studies on heated SiNCs, this is a plausible explanation for the behavior of plasma-produced SiNCs as well. However, we speculate a different possible pathway. We don't see a correlation between dangling bond reduction and PL increase during heating of the SiNCs, which means that the EPR may not be sensitive to the silyl-related dangling bonds. However, ·SiH_3 dangling bonds should have a resonance. We speculate that the silyl radicals on the SiNCs are actually charged, meaning that an electron from the SiNC joins the silyl, creating :SiH_3, which is

a charged species. This charged silyl would not have an EPR resonance, because of its even number of free electrons. Moreover, the remaining hole on the SiNC would mean that the silyl and nanocrystal are bound through Coulomb attraction, so that the silyl would not be free to evaporate without some activation energy. SiH_3 groups have many possible adsorption configurations on silicon surfaces.[24] We speculate that heating the SiNCs may potentially enable the diffusion of these charged silyls on the SiNC surface until two silyls meet, form disilane, and are desorbed. This process could allow the electrons to recombine, returning the SiNCs to neutral states and increasing the radiative recombination of excitons.[30,31] This hypothesized situation could also explain the silyl and disilyl peaks we see during thermal desorption studies, as the desorbed disilane could easily dissociate near the RGA filament and produce many SiH_x and Si_2H_x ions. There are some potential problems with this argument, though, as two charged silyls may repel one another. However, speculations about the possible routes for the silyl effusion are useful for formatting future experiments, which may pin down the real relationship between surface silyls, heating, and PL efficiency.

4.6 Conclusions and future work recommendations

This work has shown that heating the plasma-produced SiNCs leads to a change in Si-H_x (specifically SiH_3) species at the nanocrystal surface through effusion, and that this is concurrent with an improvement in PL intensity and does not closely correlate with measured dangling-bond density. Because of the dynamic gas environment in the nonthermal plasma reactor, it is reasonable to expect that these unstable species could be

deposited at the SiNC surface. Previous work by our group (see Ch. 3) has indicated a close relationship between PL and the surface as constructed by the plasma afterglow environment. Hence, it is clear that efficient emission from SiNCs is related in a complicated way to the surface of the as-produced SiNCs. While the exact reason for the increase in PL upon sufficient heating has not been identified, we surmise that there is a link between the change in the SiNC surface, the removal of Si-H_x groups, and an increase in PL efficiency via diffusion of surface species such as SiH_3 and hydrogen, leading to release of silane and a removal of non-radiative excitonic recombination routes.

We recommend future studies to identify more conclusively the role of Si-H_3 species at the SiNC surface. One idea to test this relationship is to try PL lifetime measurements on heated and unheated SiNCs. While EPR is not sensitive to the charged silyl defects, the presence of a higher concentration of defects would be manifested in a reduced PL lifetime, due to the fast non-radiative recombination of excitons at those defects. Another suggestion is to attempt to quantify the amount of hydrogen on the SiNC surfaces before and after heating to various temperatures. While relative comparisons might be drawn using FTIR, another measurement to try is FRES (forward recoil elastic spectrometry), which can identify hydrogen content in different samples using an ion beam spectroscopy method.[32] In addition, the photothermal desorption spectroscopy (PDS) technique used by Daouahi *et al.*[33] has promise in quantifying defects that are not EPR-sensitive, and may be able to elucidate some of the subtle defect

densities such as monatomic hydrogen that could be influential in the efficiency of PL from SiNCs.

We would like to gratefully acknowledge Mike Behr, Zak Holman, and Dr. Rui Pereira for their assistance with *in-situ* FTIR/heating, setting up the RGA, and performing and analyzing some of the EPR data, respectively.

References

(1) Erogbogbo, F.; Yong, K.; Roy, I.; Xu, G.; Prasad, P. N.; Swihart, M. T. *ACS Nano* **2008**, *2*, 873-878.

(2) Biaggi-Labiosa, A.; Sola, F.; Resto, O.; Fonseca, L. F.; Gonzalez-Berrios, A.; De Jesus, J.; Morell, G. *Nanotechnology* **2008**, *19*.

(3) Cheng, K.; Anthony, R.; Kortshagen, U. R.; Holmes, R. J. *Nano Letters* **2011**, *11 (5)*, 1952-1956.

(4) Puzzo, D. P.; Henderson, E. J.; Helander, M. G.; Wang, Z.; Ozin, G. A.; Lu, Z. *Nano Letters ASAP*.

(5) Mangolini, L.; Kortshagen, U. *Advanced Materials* **2007**, *19*, 2513-2519.

(6) Cheylan, S.; Elliman, R. G. *Applied Physics Letters* **2001**, *78*, 1912-1914.

(7) Godefroo, S.; Hayne, M.; Jivanescu, M.; Stesmans, A.; Zacharias, M.; Lebedev, O. I.; van Tendeloo, G.; Moshchalkov, V. V. *Nature Nanotechnology* **2008**, *3*, 174-179.

(8) Mangolini, L.; Jurbergs, D.; Rogojina, E.; Kortshagen, U. *Journal of Luminescence* **2006**, *121*, 327-334.

(9) Hua, F.; Swihart, M. T.; Ruckenstein, E. *Langmuir* **2005**, *21*, 6054-6062.

(10) Gupta, A.; Wiggers, H. *Nanotechnology* **2011**, *22*.

(11) Chen, C. H.; Chen, Y. F.; Shih, A.; Lee, S. C. *Physical Review B* **2002**, *65*.

(12) Kim, B.; Cho, C.; Kim, T.; Park, N.; Sung, G. Y.; Park, S. *Applied Physics Letters* **2005**, *86*.

(13) Garrido Fernandez, B.; Lopez, M.; Garcia, C.; Perez-Rodriguez, A.; Morante, J. R.; Bonafos, C.; Carrada, M.; Claverie, A. *Journal of Applied Physics* **2002**, *91*, 798-807.

(14) Comedi, D.; Zalloum, O. H. Y.; Mascher, P. *Applied Physics Letters* **2005**, *87*.

(15) Jung, Y.; Yoon, J.; Elliman, R. G.; Wilkinson, A. R. *Journal of Applied Physics* **2008**, *104*.

(16) Seraphin, A. A.; Ngiam, S.; Kolenbrander, K. D. *Journal of Applied Physics* **1996**, *80*, 6429-6433.

(17) Marra, D. C.; Edelberg, E. A.; Naone, R. L.; Aydil, E. S. *Journal of Vacuum Science and Technology A* **1998**, *16*, 3199-3210.

(18) Bakos, T.; Valipa, M. S.; Maroudas, D. *The Journal of Chemical Physics* **2006**, *125*.

(19) Gates, S. M.; Greenlief, C. M.; Beach, D. B. *Journal of Chemical Physics* **1990**, *93*, 7493-7503.

(20) Kessels, W. M. M.; Nadir, K.; van de Sanden, M. C. M. *Journal of Applied Physics* **2006**, *99*.

(21) Pereira, R. N.; Rowe, D. J.; Anthony, R. J.; Kortshagen, U. *Physical Reivew B* **2011**, *83*.

(22) Chatgilialoglu, C. *Chemical Reviews* **1995**, *95*, 1229-1251.

(23) Niesar, S.; Stegner, A. R.; Pereira, R. N.; Hoeb, M.; Wiggers, H.; Brandt, M. S.; Stutzmann, M. *Applied Physics Letters* **2010**, *96*.

(24) Ceriotti, M.; Bernasconi, M. *Physical Review B* **2007**, *76*.

(25) Gupta, P.; Colvin, V. L.; George, S. M. *Physical Review B* **1988**, *37*, 8234-8243.

(26) Rivolo, P.; Geobaldo, F.; Rocchia, M.; Amato, G.; Rossi, A. M.; Garrone, E. *physica status solidi (a)* **2003**, *197*, 217-221.

(27) Salivati, N.; Ekerdt, J. G. *Surface Science* **2009**, *603*, 1121-1125.

(28) Roura, P.; Farjas, J.; Rath, C.; Serra-Miralles, J.; Bertran, E.; Roca i Cabarrocas, P. *Physical Review B* **2006**, *73*.

(29) Martin, P.; Fernandez, J. F.; Sanchez, C. *Materials Science and Engineering B* **2004**, *B108*, 166-170.

(30) English, D. S.; Pell, L. E.; Yu, Z.; Barbara, P. F.; Korgel, B. A. *Nano Letters*

2002, *2*, 681-685.

(31) Valenta, J.; Fucikova, A.; Vacha, F.; Adamec, F.; Humpolickova, J.; Hof, M.; Pelant, I.; Kusova, K.; Dohnalova, K.; Linnros, J. *Advanced Functional Materials* **2008**, *18*, 2666-2672.

(32) Monelli, A.; Corni, F.; Tonini, R.; Ferrari, C.; Ottaviani, G. *Journal of Applied Physics* **1996**, *80*, 109-114.

(33) Daouahi, M.; Ben Othmane, A.; Zellama, K.; Zeinert, A.; Essamet, M.; Bouchriha, H. *Solid State Communications* **2001**, *120*, 243-248.

5. Silicon nanocrystals for hybrid inorganic / organic light-emitting devices

Note: much of the work discussed in this chapter has been reworked from two journal articles. With permission from the authors, this work has been reproduced in part from Cheng, K.-Y., Anthony, R., Kortshagen, U., and Holmes, R. J. *Nano Letters* **2010,** *10 (4),* 1154-1157, copyright 2010 American Chemical Society, and Cheng, K.-Y., Anthony, R., Kortshagen, U., and Holmes, R. J. *Nano Letters* **2011,** *11 (5),* 1952-1956, copyright 2011 American Chemical Society.

5.1 Introduction

As discussed in Chapter 1, the primary motivation for studying luminescence from silicon nanocrystals in this thesis is their use in light-emitting device applications, such as in solid-state lighting and display technologies. Most relevantly, in collaboration with Professor Russell J. Holmes and his Ph.D. student Kai-Yuan Cheng, we have successfully built several iterations of hybrid organic-SiNC light-emitting devices, one of which has achieved world-record efficiency for a nanocrystal-based LED.[1,2] As the synthesis and processing of SiNCs for this collaboration has been a major component of work for this thesis, and because the device performance is closely related to the photoluminescence efficiency of the SiNCs, this chapter will outline the devices we constructed, summarize the results, and also discuss some current work that is in progress, and yet unpublished.

The device we built is a multilayer structure of organic charge-injection layers, spin-cast SiNCs, and top electrical contacts, all constructed on a glass slide coated with indium tin oxide (ITO), a transparent conductive layer. The SiNCs in the device act as the emissive layer—rather than using ultraviolet photons as an excitation source, the

electrons and holes are injected directly into the SiNC layer *via* the organic layers. The recombination of these charge carriers leads to electroluminescence from the SiNCs. A hybrid device such as the one described here relies on organic layers to transport either electrons or holes—and those layers additionally work to block the opposite charges from exiting the SiNC layer and shorting directly to the electrode layers. This way, the electrons and holes are confined to the SiNCs and must recombine there in some capacity.

The silicon nanocrystals for the devices had a peak PL wavelength in the near-infrared (NIR) of ~850nm and were synthesized as described in Chapter 1 in the nonthermal plasma reactor. The pertinent gas flowrates were 35sccm Ar and 13 sccm SiH_4 (5% in He) with 100 sccm of H_2 injected into the plasma afterglow. Each batch of SiNCs used for LEDs was based on several hours of total collection time, deposited on separate meshes (~1hr/mesh). The SiNCs were dispersed in a dried, degassed mixture of 1:5 v/v 1-dodecene:mesitylene and refluxed for at least 2 hours at 215°C as *per* the description in Ch. 1. Following functionalization, the PL of the SiNCs was recorded. For these devices, overall the PL QYs of all samples were between 40-60%. More details on the preparation of the SiNCs for this project can be found in Appendix D.

To date, we have published two publications on hybrid SiNC-polymer LEDs, and details on the device fabrication and performance can be found in Refs. [1] and [2]. In Section 5.2, we outline the published devices and their performance. In the third section of the chapter, we discuss two works in progress, for which we do not have LED

performance data. These projects will hopefully lead to improved efficiency from hybrid SiNC-organic LEDs by directly altering SiNC characteristics.

5.2 Bilayer SiNC/organic light-emitting devices

The generalized structure of the hybrid LEDs that we have constructed is depicted in Figure 5.1. The device begins with a transparent conductive layer on glass, in this case indium tin oxide (ITO), with a spin-cast layer of PEDOT:PSS (poly[3,4-ethylenedioxythiophene]:poly[styrenesulfonate]) for hole-injection on top. Building from this, there is a hole-transport layer (HTL), made from a spin-cast organic material, then a layer of spin-cast SiNCs, followed by an electron-transport layer (ETL) and capped with patterned LiF/Al electrodes to allow 15 individual device contacts over the

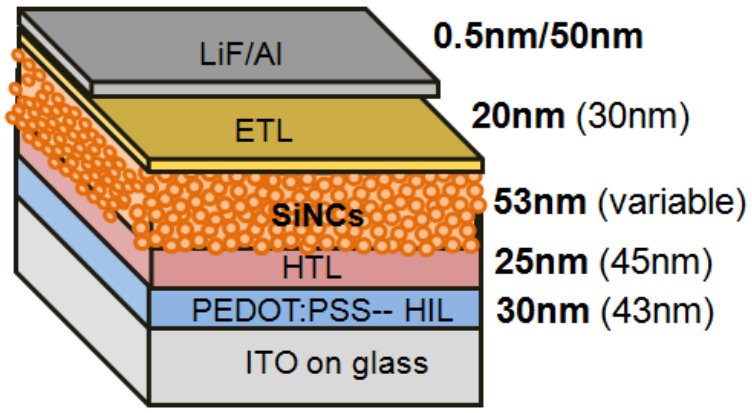

Figure 5.1: Schematic of the hybrid LED structure. Layer thicknesses from [2] (the highest-performing structure) are listed in bold, with layer thicknesses from [1] are in parentheses. For [2], the ETL was Alq3 and the HTL was cross-linked poly-TPD. For [1], the ETL was BCP and the HTL was MEHPPV.

surface of one device substrate. The device operates based on injecting and trapping charge carriers into the SiNC layer, where they recombine at the SiNCs as excitons, leading to light emission.

In the first iteration of the device, we adjusted the thickness of the emissive SiNC layer to examine the effects on LED efficiency. For the second device structure we studied, we kept the SiNC layer the same and tweaked the properties of the ETL and HTL to maximize device performance.

5.2.1 First bilayer device structure: varying the SiNC layer thickness

In the first device,[1] the spin-casting solution concentration of SiNCs was the primary variable. The device structure was composed of commercially fabricated ITO-on-glass substrate, a spin-cast layer of PEDOT:PSS for hole-injection followed by a spin-cast layer of MEH-PPV ((poly[2-methoxy-5-(2′-ethylhexyl-oxy)1,4-phenylene-vinylene]) as the hole-transporting layer. The SiNCs were spin-cast on top of the MEH-PPV layer. The electron-transporting layer was thermally-evaporated BCP (bathocuproine), a small organic molecule, and the device was finished with patterned LiF/Al (lithium fluoride / aluminum) electrodes. Thicknesses of these layers can be read in parentheses in Figure 5.1.

By adjusting the concentration of the SiNCs in solution, we hoped to optimize the electroluminescence from the SiNC layer of the device. Some successful II-VI light-emitting devices rely on a single monolayer of quantum dots, although an incomplete monolayer (with gaps) could lead to charge leakage that bypasses the nanocrystal layer.[3]

A thicker nanocrystal layer could potentially inhibit charge transfer to all of the nanocrystals through the thickness of the film—but would prevent charges from recombining directly in the organic layers rather than becoming trapped in the nanocrystal layer. We tried solution concentrations of 1, 5, 10, and 20 mg/mL of SiNCs in chloroform, based on the final weight of the samples (SiNCs-plus-dodecyl chains). Atomic force microscopy (AFM) images of the surfaces of these films show changes in film morphology with increasing solution concentration. The lowest SiNC concentration led to a film with incomplete surface coverage -- however, at concentrations higher than 1 mg/ml, the coverage is improved for all of the films. By scratching through the film, the thickness was measured using AFM as well—the films ranged in thickness from 7 nm

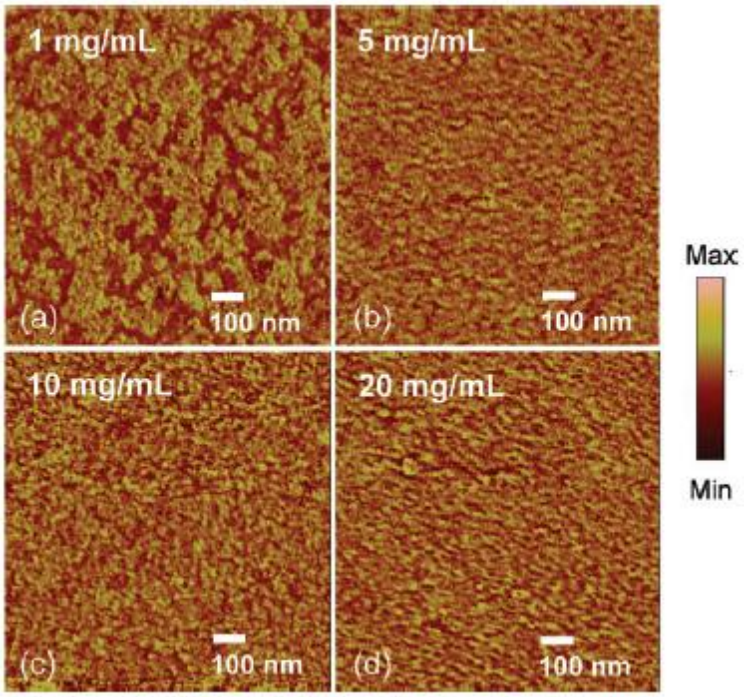

Figure 5.2: AFM images of SiNC films spin-cast from chloroform at different concentrations. The coverage in (a) is decreased compared to the coverage in the higher-concentration films. Thickness measurements on the films indicate a range of 7nm (a) to around 80nm (d). Reproduced from [1].

(1-2 monolayers) for the 1 mg/mL spin-casted film to 80 nm for the 20 mg/mL film. The AFM images of the films are shown in Figure 5.2.

This variation in film thickness was confirmed by the device characteristics. As the emissive-layer thickness was increased *via* changing the SiNC solution concentration, the emission from MEH-PPV decreased and the electroluminescence from the device was dominated by SiNC emission (Fig. 5.3b), excited with an applied current density (J) of 10mA/cm^2. The emission from MEH-PPV indicates that the injected charges are not recombining in the SiNC layer and are instead recombining in the MEH-PPV. With increasing SiNC solution concentration, the electroluminescence from the hole-transporting layer is diminished and the SiNC emission begins to dominate the device performance, showing that the charges are properly confined in the SiNC layer. The devices also exhibit different current-voltage (J-V) characteristics (Fig. 5.3a). With increasing concentration, the SiNC layers add more resistivity to the device behavior as seen in the decreasing current and increasing voltage. This is consistent with an increase in device thickness with higher-concentration SiNC solutions.

The highest-performing device was created using the 20 mg/mL SiNC solution, leading to an SiNC layer thickness of ~80nm. The measurement of LED performance used here is the external quantum efficiency, or EQE, which is defined as the ratio of the number photons emitted in the forward direction to the number of electrons injected into the device. The peak efficiency of 0.6% occurred at a current density of 7 μA/cm^2. As the injected current density increased, the emission from this device began to incorporate a component from the MEH-PPV, which indicates that under high excitation densities the

electrons and holes may recombine in the HTL rather than being strictly confined to the SiNCs.

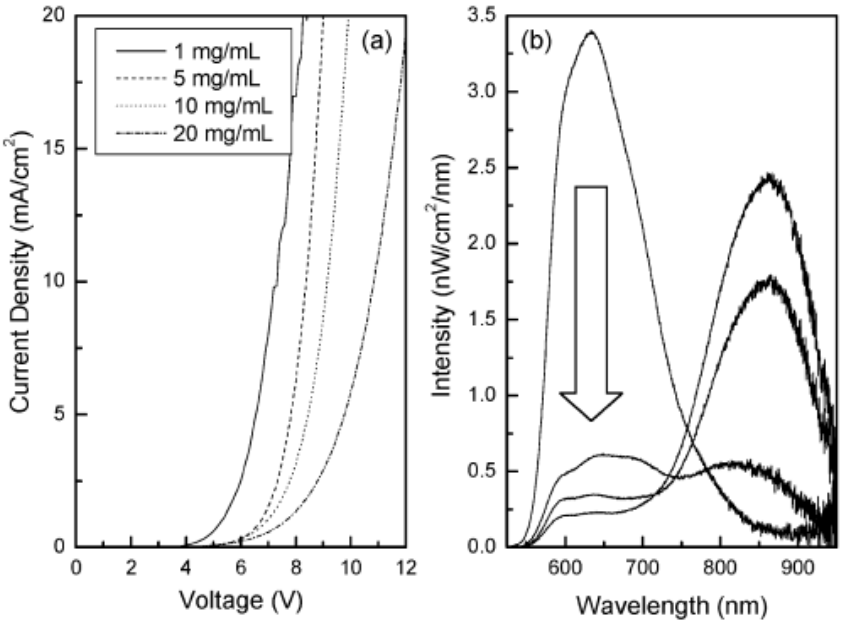

Figure 5.3: Current-density (J-V) curves (a) and electroluminescence spectra (b) from LEDs with SiNC films cast from different solution concentrations. Increasing the SiNC concentration leads to thicker films, as seen in the shift of the J-V curves to higher voltages in (a) and the increase in EL from the SiNCs as opposed to the HTL (b). Reproduced from [1].

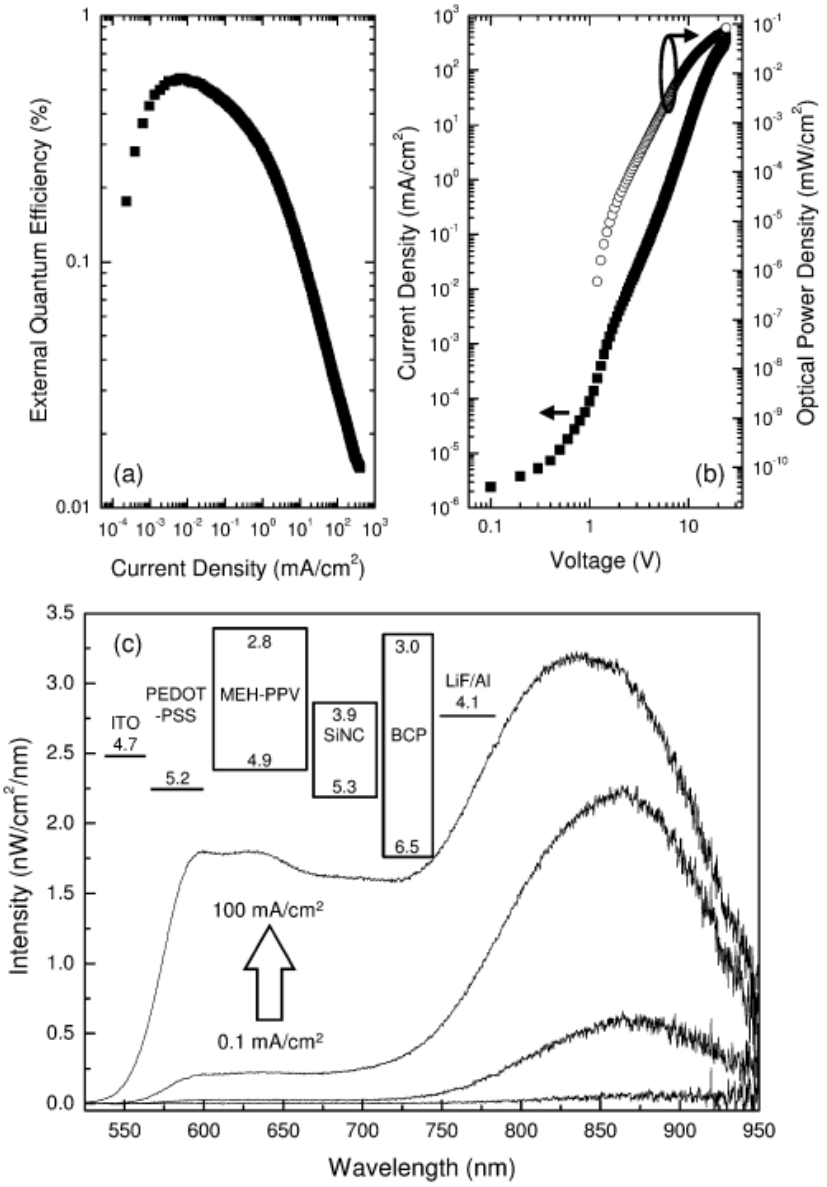

Figure 5.4: Device performance characteristics from the best-performing SiNC LED, spin-cast from a 20mg/mL solution. (a) External quantum efficiency shows a peak performance of 0.6% at 7μA/cm^2. (b) compares the optical power density and current density as voltage is increased. The electroluminescence from the device is shown for varying current densities in (c). Emission near 600nm is from the HTL, and NIR emission near 850nm is from the SiNCs. The inset of (c) shows the band diagram for the device. Reproduced from [1].

5.2.2 Second bilayer device structure: changing the transport layers

Aside from the emission from MEH-PPV at high current densities, we also encountered some issues with the synthesis steps in the device described above. For spin-casting of the MEH-PPV, we dissolved the polymer into chloroform. Then, after drying, the SiNCs were spin-casted on top, also from chloroform solution. This led to inhomogeneous layer formation and possible mixing of the two materials, despite our attempts to create a layered structure. For the next device structure we sought a hole-transporting material that was either not solution-processed or else could be solidified to prevent it from redissolving upon spin-casting the SiNCs. The material we chose was poly-TPD (poly[*N*,*N*′-bis(4-butylphenyl)-*N*,*N*′-bis(phenyl)benzidine]). While this material is also spin-cast from chloroform solution, we cross-linked the polymer using exposure to UV light, ensuring that it would no longer dissolve in the chloroform from spin-casted SiNCs. At the same time, we switched the electron-transporting layer from BCP to Alq3 (tris-[8-hydroxyquinolinato] aluminum), also a thermally evaporated molecule. This device was constructed with both infrared-emitting and red-emitting SiNCs. The change in emission energy of the SiNCs was brought about by altering the argon flowrate during synthesis, which changes the average SiNC size. The sizes used for this work were estimated to be 5nm and 3nm, based on emission peak. Functionalization of the red-emitting SiNCs was performed as described previously.

Making these transport-layer changes had a dramatic impact on the performance from the device. We immediately saw the device performance improve—and there were

no adjustments in SiNC synthesis or processing. The energy level diagram for the new device is pictured in Fig. 5.5. Although not shown, we also tried using different electron transporting layers. The other molecules chosen were CBP and TCTA, which have even wider bandgaps than Alq3, at both the highest-occupied molecular orbital (HOMO) and the lowest-unoccupied molecular orbital

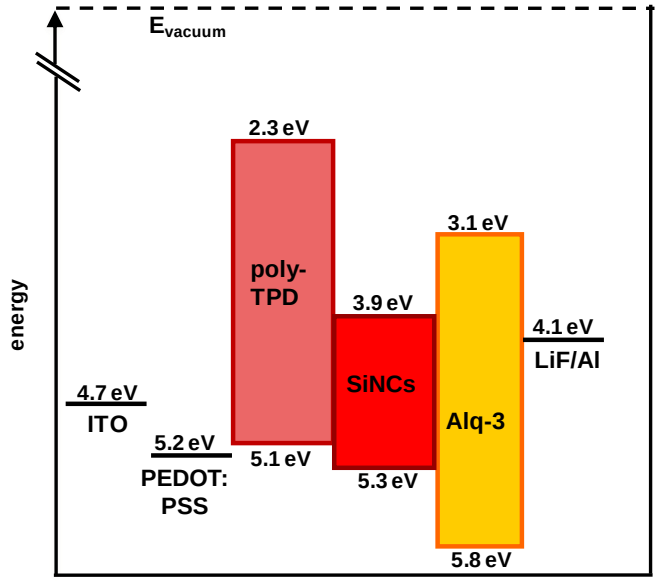

Figure 5.5: Energy level diagram for the 8.6% LED. The HOMO levels for the transport layers were taken from the literature, and LUMO levels were estimated from the absorption edge. The levels for the poly-TPD were measured using cyclic voltammetry, and the levels for the SiNCs were based on those for bulk silicon, adjusted to reflect the quantum confinement effect.

(LUMO). The molecules also have varying electron mobilities. Altering the electron mobility and HOMO/LUMO serves to probe whether the injection rate of charge carriers plays a role in the device performance.

The best-performing device utilized Alq3 as the ETL, as aforementioned, and had an efficiency of 8.6%. However, using ETLs with wider bandgaps and a range of electron mobilities still yielded device performances of >6.8%. As this performance is an order of

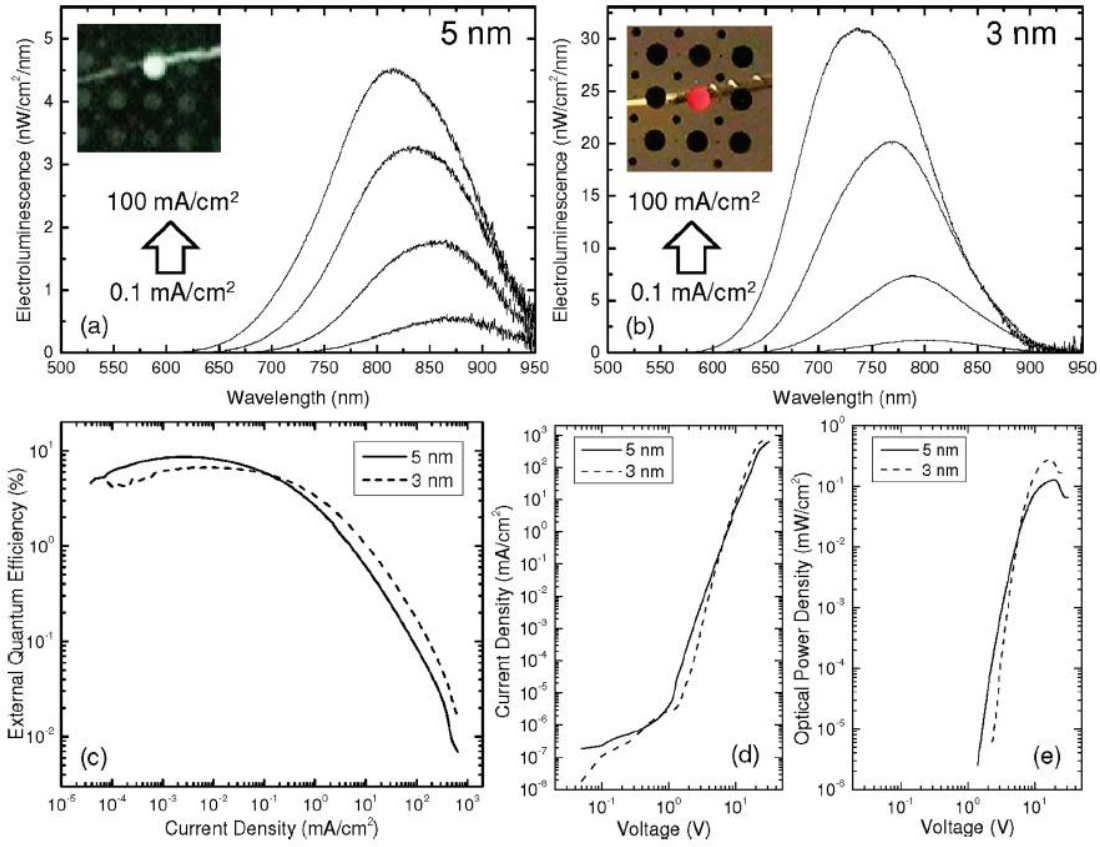

Figure 5.6: Device characteristics for the red(dashed lines) and NIR(solid lines) LEDs. Electroluminescence spectra at different current densities are plotted in (a) and (b) for the devices, with insets showing photographs of the devices in operation taken through the transparent conductive electrode. The device EQEs are plotted in (c), demonstrating peak efficiencies of 8.6% and 6.7% for NIR- and red-emitting SiNCs. (d) and (e) depict the J-V and optical power density curves for these devices as a function of applied voltage. Reproduced from [2].

magnitude better than the performance of the device with MEH-PPV as the hole-transporting layer, we can safely conclude that exchanging this layer for poly-TPD was the most influential optimization step. Poly-TPD has nearly the same energy levels as MEH-PPV, but the ability to cross-link the poly-TPD prevented issues with the non-orthogonality of the spin-casting solvents for the polymer layer and SiNC layer. Figure 5.6 shows the performance characteristics for the red (dashed lines) and NIR (solid lines) LEDs. The device efficiency that we achieved using this structure is more than two times the previous record for a nanocrystal-based LED, which is 2.7% in a hybrid device utilizing orange-emitting CdSe quantum dots capped with ZnS.[4]

5.3 Future experiments

For the first two iterations of the hybrid SiNC-organic LED, we mostly adjusted device construction parameters such as the selection and thicknesses of layers. Having seemingly optimized the device structure itself, we have now begun to change the SiNC processing steps in order to improve their electroluminescence. The studies described in this chapter are preliminary, although they will be completed and submitted for publication in the coming months.

5.3.1 Changing the ligand length

The SiNCs which are functionalized with 1-dodecene exhibit excellent PL QY—however, exciting the SiNCs using UV photons is a different situation from exciting them with injected charge carriers. For thin films of functionalized SiNCs, the SiNC cores are

surrounded by ligands nearly 1.4 nm in length, which may impact charge carrier transport in the film. In this regard, the functionalizing 1-dodecene ligands possibly present barriers to efficient charge transfer between polymers and nanocrystals, and also between SiNCs themselves. Within the Group II-VI quantum dot device community, the detrimental effects of long ligands on device performance are well-known. Many groups have experimented with removing, exchanging, or shortening the ligands on quantum dots and seen that the conductivity and device performance improve.[5-11] With SiNCs capped using alkyl chains, as in the functionalization process used in this thesis, the capping ligand is covalently bound to the SiNC surface. The covalent attachment prevents simple ligand exchange using thermal treatments, but there are other ways to attempt to improve charge transfer into and between SiNCs by altering the surface.

One of the advantages to the hydrosilylation process is that the choice of ligand is fairly flexible, provided the molecule has a functional group for binding to the SiNCs.[12] One way to examine the effects of the SiNC ligands on device performance is to change the overall length of the carbon chain attached. For example, Bakueva *et al.* found an improvement in electroluminescence efficiency when using PbS nanocrystals capped with C_8 ligands compared with C_{18} ligands.[5] In preliminary experiments, we have tried attaching 6-carbon (1-hexene), 12-carbon (1-dodecene), and 18-carbon (1-octadecene) ligands to the SiNC surfaces for LED fabrication. By doing so, we change the ligand length from ~0.6 nm (1-hexene) to 2.1 nm (1-octadecene), and we hope to find the optimal ligand length for charge transport in the LED structure. Based on the work done by other groups, we hypothesized that shorter ligands on the SiNC surfaces would result

in improved LED performance, due to enhanced electronic coupling between SiNCs and increased proximity between the charge-transport layers and the SiNC film.

Surface functionalization of SiNCs using 1-octadecene as the ligand is nearly identical to the process for using 1-dodecene, as described already. 1-octadecene has a higher boiling point than 1-dodecene (315°C compared to 212°C), and hence we raised the reaction temperature to 220-230°C, but the reaction proceeded without any problems and, in fact, often the solution "became clear" more quickly than with 1-dodecene. The PL QYs from octadecyl-capped SiNCs are comparable to those for dodecyl-capped SiNCs. The only obstacle in using 1-octadecene for functionalization was that evaporation of the mesitylene and removal of the residual, non-reacted 1-octadecene often takes several days.

Reaction of the SiNCs with 1-hexene is somewhat more challenging. 1-hexene is half as long as 1-dodecene, and has a low boiling point of 64°C, which is not a sufficiently high temperature to begin the hydrosilylation reaction. Higher temperatures, on the other hand, could potentially result in evaporation of the alkene. By keeping the reaction temperature near 200°C, ensuring a high flowrate of cold water through the refluxer tube to recondense any evaporated solvent, and adjusting the valves on the Schlenk line to result in a slightly elevated pressure within the reaction vessel, this reaction in the liquid phase did proceed. PL spectra from hexyl-, dodecyl-, and octadecyl-capped SiNCs are plotted together in Figure 5.7, along with a spectrum from unfunctionalized SiNCs, for comparison. A slight shift in PL peak can be seen amongst

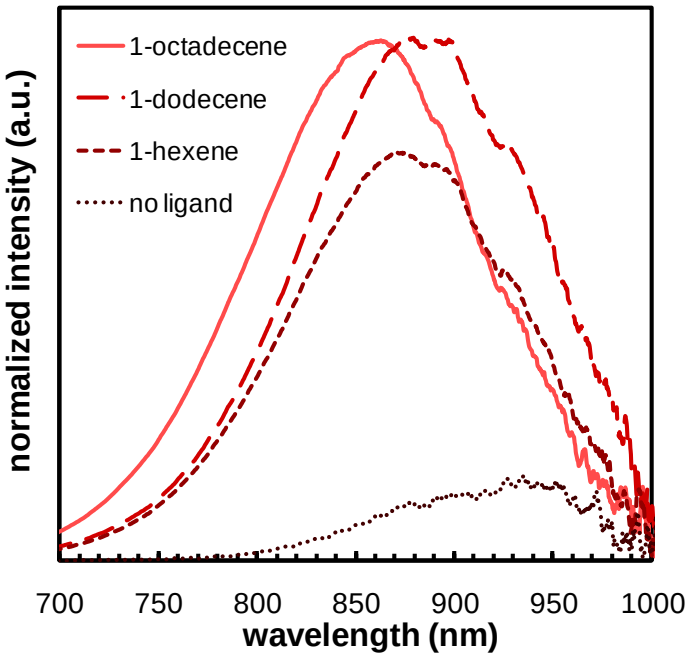

Figure 5.7: PL spectra (normalized to the absorption peak) for samples functionalized with alkenes of different lengths. The spectrum from an unfunctionalized sample is shown as well.

these samples, which has yet been unexplained. One possibility is that the peak shift can be justified based on minor run-to-run deviations in the plasma reactor. Another hypothesis is that the octadecyl-capped SiNCs are sufficiently evenly dispersed and separated from one another that the electron and hole wavefunctions of the excitons do not approach one another, particle-to-particle, as they might between dodecyl- or hexyl-capped SiNCs. Because the deviation is small and the PL QYs remain comparable, we continued with LED fabrication.

As the work is still in progress, we do not show the LED characteristics here. However, we can qualitatively state that, contrary to our hypothesis, decreasing the chain length does not lead to improved LED performance. In fact, to date we have seen that the dodecyl-capped SiNCs resulted in the best-performing LED structures. The reduced

performance for octadecyl-capped SiNCs is not surprising, as the ligand has a length nearly equal to the SiNC radius. Speculations about the reasons a dodecyl-coverage would lead to improved LED performance over hexyl-capped SiNCs are less straightforward, as shorter ligands have been demonstrated to improve charge transport in quantum dot films.[5,6]

However, the results to date should be considered in light of the fact that we do not believe the reaction of SiNCs with 1-hexene in the liquid phase leads to a surface coverage that is comparable when using 1-dodecene or longer alkenes. Alternatively, although the surface capping ratio may be equivalent, the shorter chain may not promote a homogeneous dispersion of SiNCs in concentrated solution, instead allowing clumps or agglomerates to form despite the alkyl coverage. Although PL QY was high, the SiNCs reacted in the liquid phase with 1-hexene tended to flocculate over a period of days, even though the solution was filtered with a 200nm pore size PTFE filter prior to drying and redispersing in chloroform for the final spin-casting step. Thus, the film morphology of the hexyl-capped SiNCs may not be as desirable as compared to the other SiNC films. Before the results can be confirmed, we need to make sure that the films from hexyl-covered SiNCs are as smooth and homogeneous as the others. AFM and SEM imaging will be useful tools in evaluating the surface roughness of these spin-cast SiNC films. In the meantime, we are developing a dual reaction scheme to assist in capping the SiNCs more completely, so that they do not agglomerate as quickly, and can stay suspended for the long duration that we see for the SiNCs functionalized with 12- and 18-carbon chains. In this scheme, we use a gas-phase functionalization step similar to the one reported by

Mangolini and Kortshagen[13] to preliminarily cap the SiNCs with 1-hexene. This allows them to be evenly dispersed in a 1:5 (v/v) 1-hexene:mesitylene mixture for a subsequent liquid-phase reaction, which will potentially aid in capping more of the surface sites and leading to longer-term stability in solution. Once the results of this study are confirmed, we hope to publish the work as a manuscript.

5.3.2 Changing the capping ratio

An alternative to using shorter ligands is to continue functionalizing the SiNCs with long (dodecyl) ligands, but instead change the density of ligands on the SiNC surface. By reducing the number of ligands on the surface, we may be able to promote charge transfer through non-reacted Si-H_x sites rather than forcing the charge carriers to tunnel across long chains before reaching the SiNC core. A paper by Jihua Yang *et al.* from the Kortshagen group, which has been submitted but not yet published, demonstrated improved photovoltaic performance by using SiNCs with a lower ligand capping ratio. This decrease in the number of capped sites can be achieved by reducing the v/v ratio of alkene:mesitylene by several orders of magnitude.

We have begun to experiment with reducing the 1-dodecene:mesitylene ratio and examining the effects on LED performance. In this case, we hypothesize that a reduced capping ratio will lead to improved charge transport, and therefore improved LED performance, provided the QYs of the SiNCs are consistently high and the films remain smooth. For our experiments, we have prepared SiNCs at capping ratios of 1:5, 1:20, 1:100, and 1:1000. With decreasing

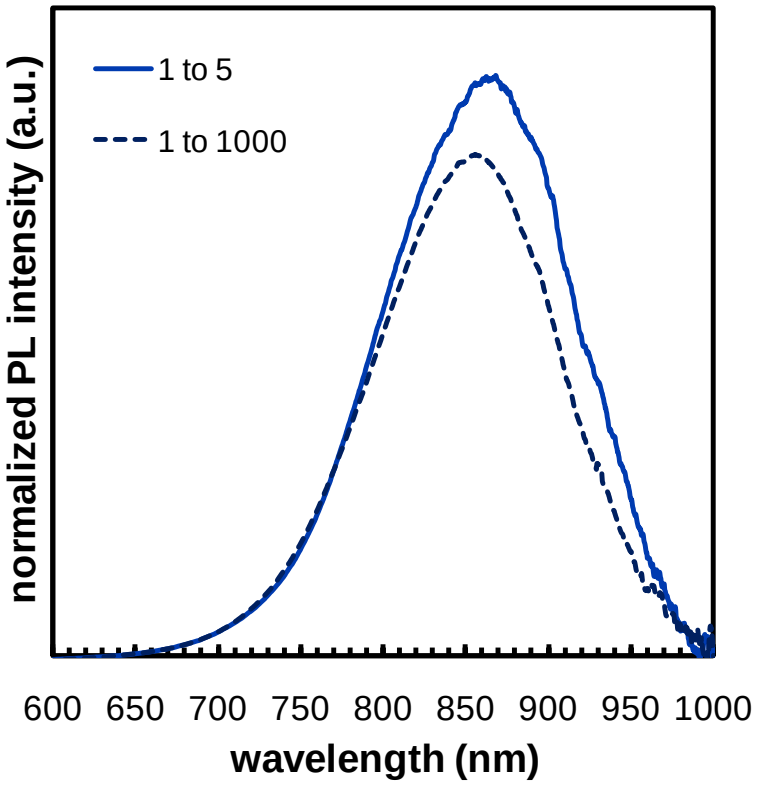

Figure 5.8: PL spectra from a 1:5 sample (solid line) and the average of two 1:1000 samples (dashed line). The lower functionalizing mixture ratio seems to give rise to a broader range of PL QYs than the 1:5 mixture. The spectra have been normalized to the absorption peaks.

alkene concentration in the functionalization solution the reaction time increases, such that the 1:1000 reaction requires heating at 215°C for 12-36 hours before becoming "clear". A comparison of PL spectra from SiNCs that were hydrosilylated in a solution of 1:5 and 1:1000 1-dodecene:mesitylene is displayed in Figure 5.8. The 1:1000-functionalized SiNCs exhibit a fluctuation in PL QY from sample to sample, so the spectrum shown is an average from two sample spectra, with 56%and 33% QY respectively. As the 1:5 ratio samples are fairly consistent in QY's above 45%, that spectrum is not an average—it is simply a representative.

Quantifying the number of ligands at the surface is an important step in this study. To do so, we have tried thermal gravimetric analysis (TGA) as a method to estimate the relative amounts of ligands in the various samples. Zachary Holman performed similar measurements on functionalized Ge nanocrystals to estimate the removal of ligands.[14] Mark Swihart's group at the University of Buffalo (SUNY) has also tried TGA for estimating the coverage of ligands on SiNCs.[15] Kai-Yuan Cheng has begun to carry out experiments using the TGA in the Chemical Engineering Department, and found that the 1:5 solvent mixture consistently results in a greater weight loss during the TGA heating to 600°C than the most extreme mixture ratio of 1:1000. While we have constructed devices using these SiNC samples, we recently discovered that the SiNC film thicknesses are different depending on the capping ratio, and so we must re-analyze the data before coming to conclusive results.

5.4 Conclusions

Constructing, testing, characterizing, and analyzing data from these hybrid SiNC-organic LEDs is time-consuming, but we have made major advances in the past 3 years of this collaboration. Our first published device, using MEHPPV as the hole-transporting layer, was a step in the right direction with an EQE of 0.6%, and showed us the importance of the SiNC film thickness. By maintaining our SiNC synthesis and processing parameters and changing the organic layers in the device, we made a leap forward and improved our device performance up to 8.6%, a world-record for nanocrystal-based LEDs.

The next steps are to optimize the LED performance from the standpoint of engineering the SiNCs for better electroluminescence. We have two active projects addressing this challenge, both concerning the SiNC capping ligands. In the first project, we are adjusting the length of the carbon chain attached to the SiNC surfaces. By fabricating LEDs using SiNCs with different capping ligand lengths, we hope to find a dependence of LED efficiency on ligand length. In the second endeavor, we are tweaking the number of ligands on the SiNC surfaces. All other parameters being equal, by reducing ligand coverage we predict enhanced performance from the LEDs, due to more efficient charge transport to the SiNC cores.

Given the versatility of SiNC properties, there are many routes for future work on the hybrid LED project. For example, thus far only NIR- and red-emitting SiNCs have been tried. As the size of the SiNCs can easily be tuned, it may be of interest to make LEDs with peak emission at other wavelengths, or to combine SiNCs of different sizes in a single device to create a broad electroluminescence peak or to study the charge transfer dynamics by examining EL peak as a function of operating parameters. Another idea in the same line as the current work described in Section 5.3 is to create core-shell SiNCs, using a wide-bandgap material as a capping layer, allowing closer packing of the SiNCS in films and possibly enhancing the charge transport, while still saturating dangling bonds and surface defects with the shell material. Some ideas include SiO_2, amorphous Si, and ZnS, ZnSe, or ZnO.

References

(1) Cheng, K.; Anthony, R.; Kortshagen, U. R.; Holmes, R. J. *Nano Letters* **2010**, *10 (4)*, 1154-1157.

(2) Cheng, K.; Anthony, R.; Kortshagen, U. R.; Holmes, R. J. *Nano Letters* **2011**, *11 (5)*, 1954-1956.

(3) Coe-Sullivan, S.; Woo, W.; Steckel, J. S.; Bawendi, M.; Bulovic, V. *Organic Electronics* **2003**, *4*, 123-130.

(4) Anikeeva, P. O.; Halpert, J.; Bawendi, M.; Bulovic, V. *Nano Letters* **2009**, *9*, 2532-2536.

(5) Bakueva, L.; Musikhin, S.; Hines, M.; Chang, T. F.; Tzolov, M. *Applied Physics Letters* **2003**, *82*, 2895-2897.

(6) Talgorn, E.; Moysidou, E.; Abellon, R. D.; Savenije, T. J.; Goossens, A.; Houtepen, A. J.; Siebbeles, L. D. A. *Journal of Physical Chemistry C* **2010**, *114*, 3441-3447.

(7) Seo, J.; Kim, S. J.; Kim, W. J.; Singh, R.; Samoc, M.; Cartwright, A. N.; Prasad, P. N. *Nanotechnology* **2009**, *20*.

(8) Talapin, D. V.; Murray, C. B. *Science* **2005**, *310*, 86-89.

(9) Wills, A. W.; Kang, M. S.; Khare, A.; Gladfelter, W. L.; Norris, D. J. *ACS Nano* **2010**, *4*, 4523-4530.

(10) Zhou, Y.; Riehle, F. S.; Yuan, Y.; Schleiermacher, H.; Niggemann, M.; Urban, G. A.; Kruger, M. *Applied Physics Letters* **2010**, *96*.

(11) Niu, Y.; Munro, A. M.; Cheng, Y.; Tian, Y.; Liu, M. S.; Zhao, J.; Bardecker, J. A.; Jen-La Plante, I.; Ginger, D. S.; Jen, A. K. *Advanced Materials* **2007**, *19*, 3371-3376.

(12) Buriak, J. M. *Chemical Reivews* **2002**, *102*, 1272-1308.

(13) Mangolini, L.; Kortshagen, U. *Advanced Materials* **2007**, *19*, 2513-2519.

(14) Holman, Z. C.; Kortshagen, U. R. *Langmuir* **2009**, *25*, 11883-11889.

(15) Hua, F.; Swihart, M. T.; Ruckenstein, E. *Langmuir* **2005**, *21*, 6054-6062.

6. Luminescent films of surface-functionalized silicon nanocrystals: a gas-phase-only approach to device formation

Note: parts of this text will be submitted to the journal *Nano Letters* in 2011 with the authors R. J. Anthony, K.-Y. Cheng, Z. C. Holman, R. J. Holmes, and U. Kortshagen.

6.1 Introduction

The development of light-emitting devices, solar cells, and other optoelectronic devices using novel materials such as nanocrystals and thin inorganic films hinges on creating ways to deposit those materials that are efficient, streamlined, and easily scaled up. Contemporary technologies using inorganic nanomaterials in these types of applications frequently rely on solution-processing techniques:[1-10] while liquid-phase processing is a reliable method of creating thin films of semiconductor nanomaterials, it can also lead to problems for scaling up production. Many of these device architectures are best optimized in layered structures of strictly inorganic or both organic and inorganic materials, for example in creation of heterojunction devices or multi-color or multi-layer light emitting devices.[1,7,9,11,12] In these multilayer structures, solution-processing of thin films can lead to redissolving of layers during sequential layer deposition, and more steps may be needed during processing to remove excess solvents. For nanocrystal deposition, sometimes lengthy solution-based functionalization procedures are necessary to achieve nanocrystal solubility, and following film formation the ligands must be removed to

improve device performance. For these next-generation devices, a key step will be to design a way to make thin films of inorganics in absence of liquid-phase processes, preferably minimizing the number of discrete, user-mediated steps.

Here, we present an exciting means of creating dense films of luminescent, surface-passivated silicon nanocrystals (SiNCs) without the use of solution-phase processing steps. In this scheme, silicon nanocrystals are produced using a flow-through plasma reactor, given a nominal surface functionality in the afterglow of the plasma, and then impacted onto device substrates directly from the gas-phase. This impaction-driven film deposition technique is an exciting route to producing thin, dense films of nanocrystals on a variety of substrates. Additionally, because the method is an exclusively gas-phase process, it can be used for depositions of molecules and materials other than nanocrystals, provided the materials can be aerosolized. Due to the flexibility of the procedure, this lays the foundation to enable many types of single and multi-layer device structures with components that can be aerosolized or evaporated to allow gas-phase deposition.

6.2 Experimental details

The technique we used was first introduced by Holman and Kortshagen, who used a plasma reactor and gas-phase impaction to fabricate films of germanium nanocrystals.[13] Those authors extensively characterized the resulting germanium nanocrystal films and modeled the parameters of the impaction scheme to better understand the formation of dense films. In addition, they were able to use photolithography to pattern the Ge

nanocrystal films, showing that the nanocrystal layers deposited in this way are dense and robust enough to withstand conventional device processes. In the present work, we have applied this film-formation technique to SiNCs produced in a plasma reactor, adding to the process a simple, minimal-effort, gas-phase surface functionalization step. This enables us to create films of nanocrystals which exhibit photoluminescence and, when incorporated into a silicon nanocrystal-only light-emitting device, also show electroluminescence. The manufacture of the light-emitting device involves no liquid-phase processing: for nanocrystal synthesis, surface passivation, film formation, and top-contact deposition, we have utilized purely gas-phase methods.

In this scheme, we used a plasma reactor as described in Ref. 14, but made an alteration to accommodate a gas-phase plasma-afterglow-initiated reaction between SiNCs and alkene vapor. The gas-phase-functionalization step is a modified version of a technique to plasma-graft alkene ligands onto SiNCs as reported by Mangolini *et al*.[15] In that process, the SiNCs were injected into a secondary, low-power plasma, into which was also injected the vapor of alkene molecules such as 1-dodecene and 1-hexene. The energy from the low-intensity plasma successfully instigated the reaction of the alkene molecules with the SiNC surfaces. Here we rely upon the same principle; however, rather than utilizing a secondary plasma reactor for ligand attachment, we simply flow the vapor of the 1-dodecene into the sidearm of the plasma reactor tube, where it enters the afterglow of the SiNC synthesis plasma. The afterglow also has sufficient energy to attach the ligand molecules to SiNC surfaces. Ordinarily, surface-functionalization of SiNCs serves both to reduce surface defect states and to improve solubility for spin-

casting film formation. As the SiNCs synthesized and functionalized as described above will be directly impacted into films, in this case we are primarily interested in the capping of defects for improvement of luminescence.

With the reactor set up as described, we then added the apparatus for impaction as per Ref. 13 to allow the aerosol of alkene-capped SiNCs to be collected directly as a film. Using a PTFE slit-shaped orifice directly below the plasma reactor, a pressure differential is established between the reactor above the orifice and the deposition region below the orifice. This pressure difference acts to accelerate the SiNCs through the orifice, where they reach or exceed sonic speeds.[13] To form dense films of the accelerated alkyl-capped SiNCs, device substrates are rastered beneath the orifice at a distance of < 1 cm from the opening using a stainless-steel pushrod (MDC Vacuum Products). Figure 6.1 shows a schematic of the reactor.

The gases used for synthesis were argon (35 sccm) and silane (5% bal. He), and the 1-dodecene vapor was carried into the plasma afterglow using 100 sccm of hydrogen. The pressure above the orifice in the synthesis region was 1.2 Torr, and the pressure below the orifice in the impaction region was ~230 mTorr, a pressure differential of ~5. We deposited films on ITO-on-glass slides for LED growth, on glass slides for photoluminescence (PL) and x-ray diffraction (XRD) measurements, and on gold-coated silicon wafers for Fourier-transform infrared (FTIR) spectroscopy.

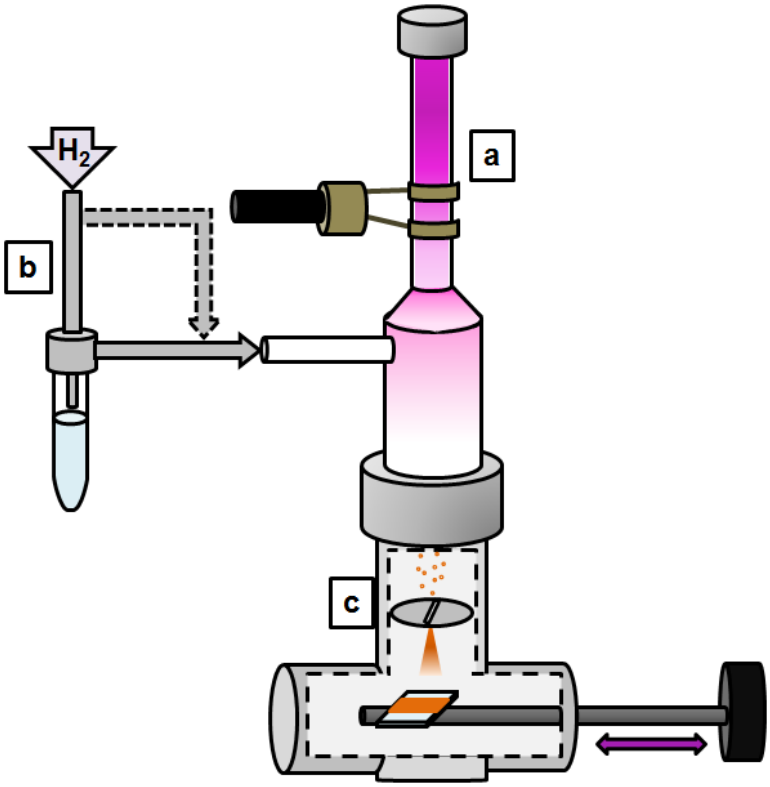

Figure 6.1: Schematic of the gas-phase-only synthesis, functionalization, and deposition apparatus.

6.3 Film Characterization

We examined the SiNC films using FTIR spectroscopy to search for evidence of carbon-chain attachment on the SiNCs. The FTIR spectra were recorded inside a nitrogen-purged glove box using a Bruker Alpha FTIR operating in diffuse reflectance (DRIFTS) mode, and taken from thick films deposited on gold-coated silicon wafers during 80 raster scans. Based on our film thickness calibration for thinner films, 80 raster

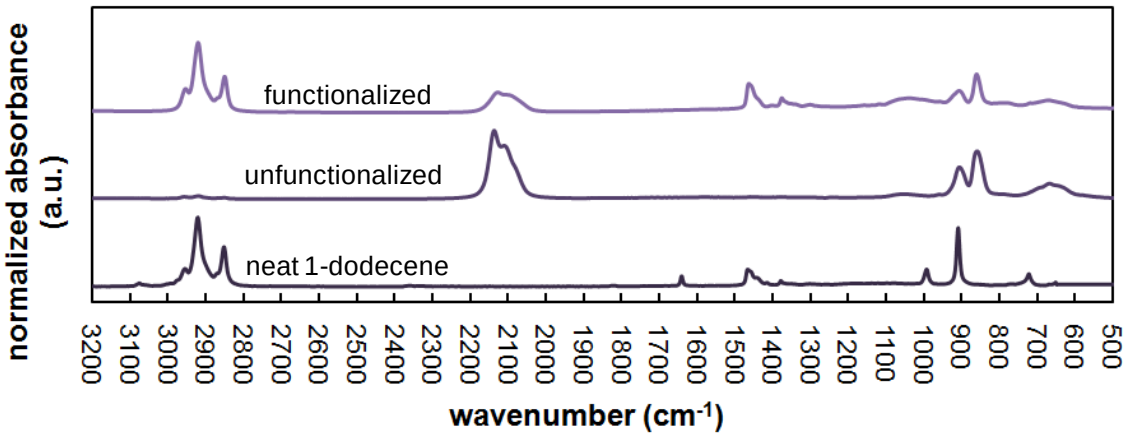

Figure 6.2: FTIR spectra from bare and gas-phase-functionalized SiNC films, with neat 1-dodecene also shown. The sharp peaks from the unsaturated carbon bond, as evidenced in near 3,080cm^{-1}, 1,640cm^{-1}, and between 900-1,000cm^{-1} in the neat 1-dodecene spectrum, are not present in the functionalized SiNC film, although –CH_x and C-H_x peaks are present. This indicates reaction of the 1-dodecene with the SiNCs in the gas-phase plasma-afterglow-initiated functionalization step.

scans should correspond to a film roughly 1-2 μm thick. FTIR spectra from both hydrogen-capped and gas-phase-functionalized SiNC films are shown, for comparison, in Figure 6.2, along with a spectrum from neat 1-dodecene. The unfunctionalized film displays peaks primarily from Si–H_x(~2,100 cm^{-1} and 800-900 cm^{-1})[16] with a small Si–O–Si peak near 1,100 cm^{-1}, due to slight and difficult-to-eliminate air exposure. While there is still a significant peak near 2,100 cm^{-1} from Si–H_x vibrations, the presence of carbon chains is confirmed from the C–H_x stretching vibrations near 2,900 cm^{-1} (Figure 2). It is difficult to prove that the carbon chains have chemically bound to the SiNC surfaces using FTIR, especially since the degree of capping using the gas-phase-functionalization scheme is expected to be low. However, we observe that the peaks associated with the double-bond of the alkene (near 1,640 cm^{-1} for C=C and 3,080 cm^{-1}

for $=CH_2$)[17] are not present. As this is the bond that reacts with the SiNC surface during hydrosilylation, the absence of these peaks is one clue that the reaction has proceeded.

To further confirm that the alkene ligands had reacted with the SiNCs during the plasma-initiated functionalization step, we tried to remove the SiNC films into solvents. While hydrogen-capped (as-produced) SiNCs are lyophobic and will not disperse in nonpolar solvents, dodecyl-capped SiNCs are soluble in nonpolar solvents and should be easily dispersed. The films of SiNCs can be generated with or without gas-phase passivation, as shown in Fig. 1, providing a simple test for SiNC functionality. We made films on glass substrates both with and without the alkene ligand flow, and tried to rinse the SiNC films from the glass. The SiNC films deposited in the absence of ligand flow remained intact on the glass substrates when rinsed with chloroform. In contrast, the films made in accordance with the gas-phase functionalization scheme were easily removed from the glass substrates by washing with chloroform, and formed clear colloids. This confirms the success of alkyl attachment using this scheme.

The films were examined using SEM to verify the thickness and uniformity of the SiNC layers. Films for SEM were deposited on aluminum-coated ITO-on-glass and coated with 30Å of platinum, to improve contrast. A cross-section of the film made with 30 raster passes is shown

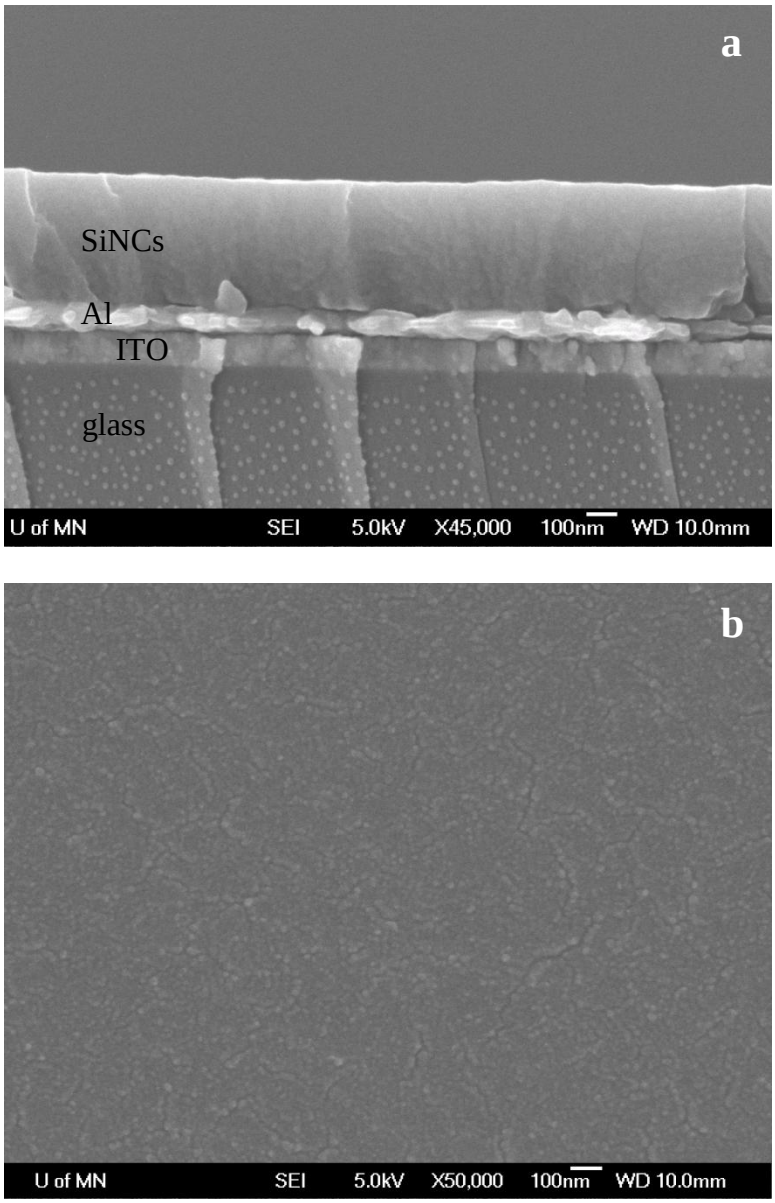

Figure 6.3: SEM images of gas-phase-impacted SiNC films: (a) cross-section and (b) top-down view.

in Figure 6.3a—the film is even and dense. The top-down view (Figure 6.3b) demonstrates that the film is uniform.

In order to measure the photoluminescence spectrum from gas-phase-passivated SiNCs, we made a thicker film on a microscope glass slide, then placed the slide in an

integrating sphere connected using an optical fiber to an Ocean Optics, Inc. USB2000+ spectrometer. The integrating sphere is useful for measuring quantum yields of solution-based samples; here we use it simply to collect the light from the SiNC film and measure a photoluminescence spectrum. The sample was illuminated using a UV-blue LED (395 nm peak), and data was collected for long integration times and averaged in order to smooth the PL curve. The spectrum is shown in Figure 6.4a. X-ray diffraction, shown in Figure 6.4b, confirms that the deposited SiNCs are nanocrystalline, and Scherrer broadening calculations indicate an average crystallite size of ~3.3 nm.

The long collection time necessary for a smooth curve prohibited an accurate quantification of PL QY, and so we also collected PL data for shorter integration times to attempt to measure QY. For this experiment, we also placed the slide into the integrating sphere, and adjusted its angle with respect to the LED source and optical fiber such that the PL signal from the SiNCs was not artificially high or low due to reflection of the LED and SiNC PL off of the glass and into or away from the optical fiber. For a reference, we used a clean glass slide, similarly oriented to avoid signal distortion. These measurements were performed using an Ocean Optics USB2000 spectrometer, which has a range to include both the peak from the LED as well as the SiNC peak. The resulting PL QY from the gas-phase-functionalized impacted SiNC film was ~5.6%, and it was ~2.5% for the bare (unfunctionalized) SiNC film. These films were kept air-free in a nitrogen-purged glove box until measurement, but were exposed to air during the measurement. The PL spectra for these two samples, normalized to the absorption peak, are plotted in Figure 6.4c.

As a last experiment on the photoluminescence from SiNC films produced in this manner, we also adjusted the SiNC size to achieve different peak PL wavelengths from these films. To change the SiNC sizes, we increased the argon flowrate through the reactor, increasing the width of the slit orifice to keep the pressure in the reactor close to 1.4 Torr regardless of total gas flowrate. In Figure 6.4d, we show PL curves from three SiNC sizes, which were all functionalized in the gas phase as described previously in this chapter. We performed XRD measurements of these films, and Scherrer broadening analysis indicated crystallite sizes of 4.1nm, 3.2nm, and 2.5nm, with the emission peak shifting to the blue with decreasing SiNC crystallite size.

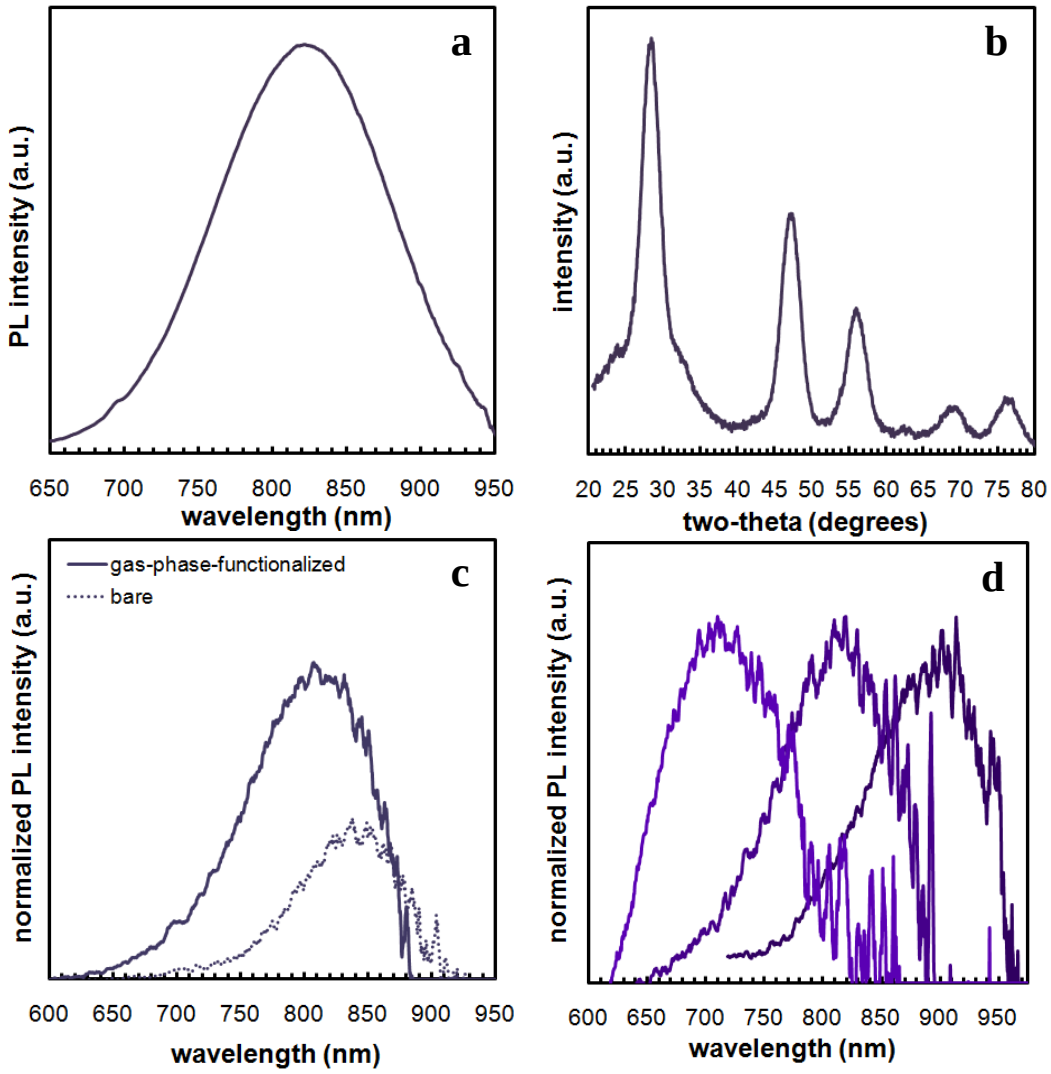

Figure 6.4: PL spectra and XRD pattern from SiNC films. (a) PL spectrum with long integration time from gas-phase-functionalized impacted SiNC film; (b) XRD pattern showing peaks from 3.3 nm crystallites; (c) comparison of PL spectra of gas-phase-functionalized (solid line) and bare (dashed line) impacted SiNC films, normalized to LED absorption; (d) PL spectra from gas-phase-functionalized impacted films of different SiNC sizes, normalized to emission peak. From right to left, these films incorporated SiNCs of 4.1, 3.2, and 2.5 nm as calculated based on XRD peak broadening. Thanks to David Rowe for obtaining the XRD data.

6.4 Gas-phase-only SiNC light-emitting films for devices

One of the advantages of gas-phase-only film deposition is the added flexibility in patterning and layer formation that can be achieved. We experimented with deposition of SiNCs onto a lift-off mask. Following deposition, we allowed the SiNCs to oxidize in air for a few days, then removed the mask. The film of nanocrystals in the features of the mask remained intact. A photograph of the film, illuminated using a 395 nm LED (shown at the top of the photo)

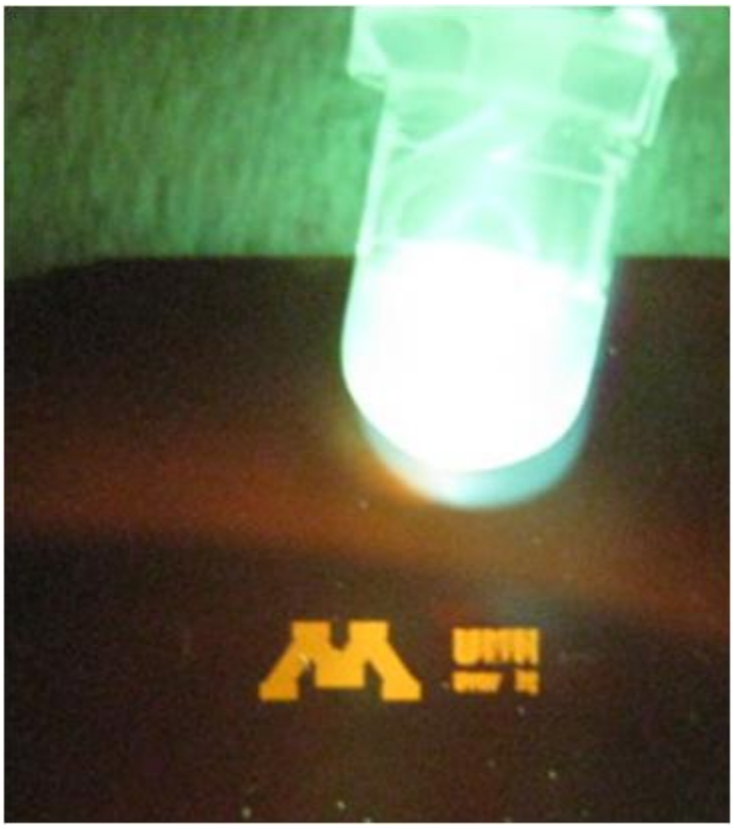

Figure 6.5: Photograph of SiNC film following several days' oxidation and photolithographic mask lift-off. The image is taken using a digital camera and a longpass filter between the LED and camera lens.

and taken through a 475 nm longpass filter to reduce the intensity of the LED's emission, is shown in Figure 6.5. The photoluminescence of the SiNC features (in a U of M – themed pattern) is clearly visible in the photograph. This demonstration is quite meaningful, as it shows preliminarily that luminescent films of SiNCs deposited from the gas-phase can be accurately patterned. As we have shown, the luminescence peak of different films can be tuned according to the SiNC size, and with the illustration that the films can be spatially designed, we propose that multicolor luminescent displays, such as the one demonstrated by Kim *et al.*[18] could be fabricated exclusively from the gas phase by adjusting patterns and SiNC sizes in this streamlined synthesis/functionalization/deposition step.

To elaborate on the functionality of these SiNC films, we made single-layer light-emitting devices comprised of purely inorganic materials. A glass substrate commercially coated with ITO (indium tin oxide) was placed on the pushrod using double-sided carbon tape. Films of gas-phase-passivated SiNCs were deposited through the orifice onto the device substrates. The pushrod setup is accompanied by a miniature gate valve, which can be sealed before the pushrod and substrates are removed from the reactor, so that the samples remain under vacuum until they are transferred to a nitrogen-purged glovebox for the final device layer deposition. The top contacts of the device are made from thermally evaporated LiF/Al (5Å/50nm).

We studied three thicknesses of SiNC films for the purposes of LED performance analysis, ranging in thickness from 150 nm to 600 nm. For the devices measured, the thinnest device (10 raster passes) performed the best, with a peak external quantum

efficiency of 0.03%. The thicker films exhibited very poor EQE and erratic behavior, likely due to the thickness of the film inhibiting effective charge transfer. We also tried much thinner devices (1 and 5 passes) but the films were so thin and the charges so inefficiently confined to the SiNC layer that the leakage current prevented effective electroluminescence. The EQE and J-V curves of the best device are plotted in Figure

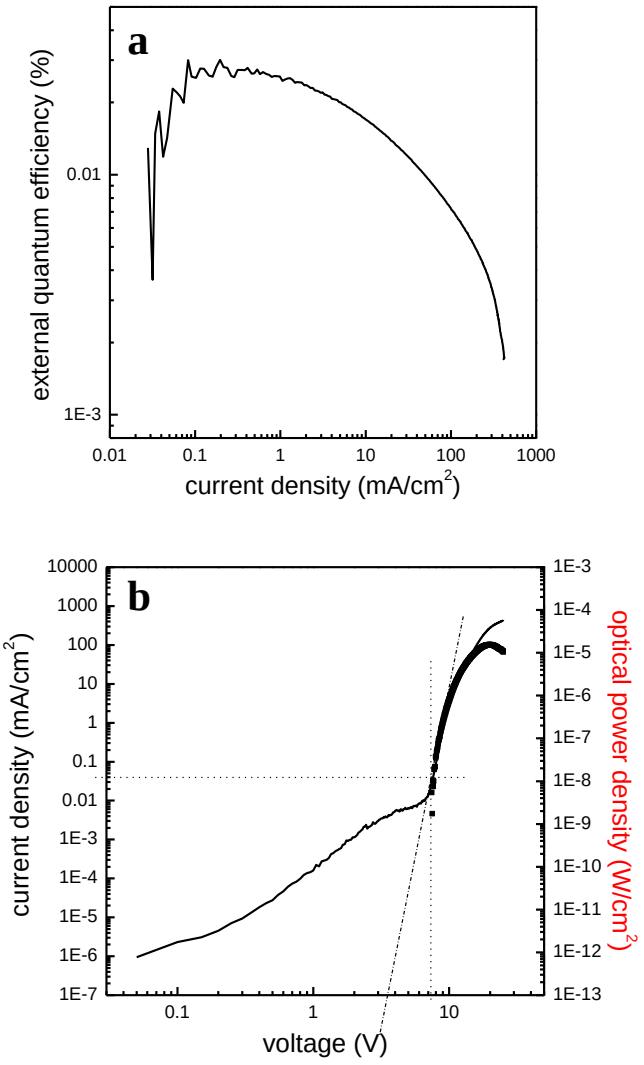

Figure 6.6: Device characteristics for the all-gas-phase SiNC LED. (a) external quantum efficiency and (b) current density and optical power density as a function of voltage.

6.6a and b, and the electroluminescence spectrum from the device is shown in Figure 6.7. Although this performance is unremarkable in comparison to other silicon nanocrystal-based LEDs,[3,19,20] this proof-of-concept device structure is unoptimized and involv no charge-carrier blocking or injection layers to confine the electrons and holes in the SiNC film. Previous work has shown that confining the charges to the SiNC layer using wide-bandgap molecules can lead to excellent electroluminescence from SiNCs,[3] and so we are encouraged by the electroluminescence from the device and firmly believe that an optimized multilayer structure can lead to much improved device characteristics.

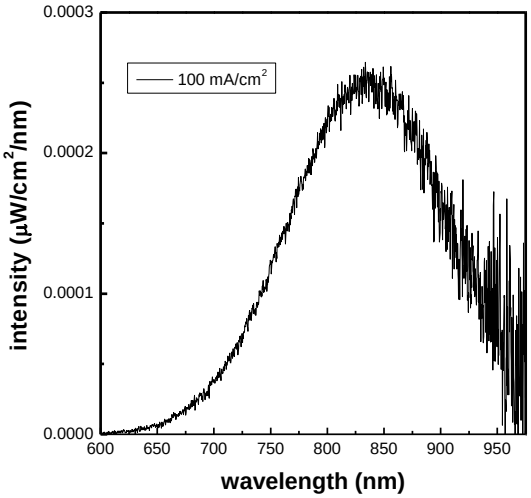

Figure 6.7: Electroluminescence from the gas-phase-functionalized impacted SiNC LED.

6.5 Conclusions

In conclusion, we have demonstrated a novel process for deposition of luminescent SiNC films using a gas-phase-only approach. This impaction-driven film formation process is versatile with regards to film material and substrate, and has the potential to be a component of a complete device deposition chamber in absence of any

liquid-phase processes. The SiNC films exhibit photoluminescence and electroluminescence, and can be used in a variety of device synthesis schemes including simple mask lift-off processes and multilayer structures. By eliminating the necessity for liquid-phase processing steps, this approach can lead to gas-phase-only routes to fabrication single- and multi-layer devices in a streamlined flexible scheme.

References

(1) Anikeeva, P. O.; Halpert, J. E.; Bawendi, M. G.; Bulovic, V. *Nano Letters* 2007, *7*, 2196-2200.

(2) Bakueva, L.; Musikhin, S.; Hines, M.; Chang, T. F.; Tzolov, M. *Applied Physics Letters* 2003, *82*, 2895-2897.

(3) Cheng, K.; Anthony, R.; Kortshagen, U. R.; Holmes, R. J. *Nano Letters* **2011**, *11(5)* 1952-1956.

(4) Coe, S.; Woo, W.; Bawendi, M.; Bulovic, V. *Nature* 2002, *420*, 800-803.

(5) Dabbousi, B. O.; Bawendi, M. G.; Onitsuka, O.; Rubner, M. F. *Applied Physics Letters* 1995, *66*, 1316-1318.

(6) Haverinen, H. M.; Myllyla, R. A.; Jabbour, G. E. *Journal of Display Technology* 2010, *6*, 87-89.

(7) Stouwdam, J. W.; Janssen, R. A. J. *Journal of Materials Chemistry* 2008, *18*, 1889-1894.

(8) Svrcek, V.; Mariotti, D.; Shibata, Y.; Kondo, M. *Journal of Physics D: Appled Physics* 2010, *43*.

(9) Tan, Z.; Xu, J.; Zhang, C.; Zhu, T.; Zhang, F.; Hedrick, B.; Pickering, S.; Wu, J.; Su, H.; Gao, S.; Wang, A. Y.; Kimball, B.; Ruzyllo, J.; Dellas, N. S.; Mohney, S. E. *Journal of Applied Physics* 2009, *105*.

(10) Wood, V.; Panzer, M. J.; Chen, J.; Bradley, M. S.; Halpert, J. E.; Bawendi, M. G.; Bulovic, V. *Advanced Materials* 2009, *21*, 2151-2155.

(11) Gao, J.; Luther, J. M.; Semonin, O. E.; Ellingson, R. J.; Nozik, A. J.; Beard, M. C. *Nano Letters* 2011, *11*, 1002-1008.

(12) Osedach, T. P.; Geyer, S. M.; Ho, J. C.; Arango, A. C.; Bawendi, M. G.; Bulovic, V. *Applied Physics Letters* 2009, *94*.

(13) Holman, Z. C.; Kortshagen, U. R. *Nanotechnology* 2010, *21*.

(14) Mangolini, L.; Thimsen, E.; Kortshagen, U. *Nano Letters* 2005, *5*, 655-659.

(15) Mangolini, L.; Kortshagen, U. *Advanced Materials* 2007, *19*, 2513-2519.

(16) Marra, D. C.; Edelberg, E. A.; Naone, R. L.; Aydil, E. S. *Journal of Vacuum Science and Technology A* 1998, *16*, 3199-3210.

(17) Mangolini, L.; Jurbergs, D.; Rogojina, E.; Kortshagen, U. *physics status solidi (c)* 2006, *3*, 3975-3978.

(18) Kim, T.; Cho, K.; Lee, E. K.; Lee, S. J.; Chae, J.; Kim, J. W.; Kim, D. H.; Kwon, J.; Amaratunga, G.; Lee, S. Y.; Choi, B. L.; Kuk, Y.; Kim, J. M.; Kim, K. *Nautre Photonics* 2011, *5*, 176-182.

(19) Cheng, K.; Anthony, R.; Kortshagen, U. R.; Holmes, R. J. *Nano Letters* 2010, **10** (4), 1154-1157.

(20) Puzzo, D. P.; Henderson, E. J.; Helander, M. G.; Wang, Z.; Ozin, G. A.; Lu, Z. *Nano Letters ASAP*.

Bibliography

Anikeeva, P. O.; Halpert, J. E.; Bawendi, M. G.; Bulovic, V. *Nano Letters* **2007**, *7*, 2196-2200.

Anikeeva, P. O.; Halpert, J.; Bawendi, M.; Bulovic, V. *Nano Letters* **2009**, *9*, 2532-2536.

Anopchenko, A.; Marconi, A.; Moser, E.; Wang, M.; Pucker, G.; Bellutti, P.; Pavesi, L. *IEEE Conference on Group IV Photonics* **2009**.

Anthony, R.; Kortshagen, U. *Physical Review B* **2009**, *80*.

Bakos, T.; Valipa, M. S.; Maroudas, D. *The Journal of Chemical Physics* **2006**, *125*.

Bakueva, L.; Musikhin, S.; Hines, M.; Chang, T. F.; Tzolov, M. *Applied Physics Letters* **2003**, *82*, 2895-2897.

Beard, M. C.; Knutsen, K. P.; Pingrong, Y.; Luther, J. M.; Song, Q.; Metzger, W. K.; Ellingson, R. J.; Nozik, A. J. *Nano Letters* **2007**, *7*, 2506-2512.

Biaggi-Labiosa, A.; Sola, F.; Resto, O.; Fonseca, L. F.; Gonzalez-Berrios, A.; De Jesus, J.; Morell, G. *Nanotechnology* **2008**, *19*.

Bondar, V. *physics status solidi (a)* **1999**, *176*.

Boninelli, S.; Iacona, F.; Franzo, G.; Bongiorno, C.; Spinella, C.; Priolo, F. *Journal of Physics: Condensed Matter* **2007**, *19*.

Boukherroub, R.; Morin, S.; Wayner, D. D. M.; Bensebaa, F.; Sproule, G. I.; Baribeau, J.; Lockwood, D. J. *Chemical Materials* **2001**, *13*, 2002-2011.

Brus, L. E.; Szajowski, P. F.; Wilson, W. L.; Harris, T. D.; Schuppler, S.; Citrin, P. H. *Journal of the American Chemistry Society* **1995**, *117*, 2915-2922.

Buriak, J. M. *Chemical Reivews* **2002**, *102*, 1272-1308.

Canham, L. T. *Applied Physics Letters* **1990**, *57*, 1046-1048.

Cao, Y.G.; Chen, X.L.; Lan, Y.C.; Liang, J.K. *Applied Physics A* **2000**, *71*, 229-231.

Ceriotti, M.; Bernasconi, M. *Physical Review B* **2007**, *76*.

Chatgilialoglu, C. *Chemical Reviews* **1995**, *95*, 1229-1251.

Chen, C. H.; Chen, Y. F.; Shih, A.; Lee, S. C. *Physical Review B* **2002**, *65*.

Cheng, K.; Anthony, R.; Kortshagen, U. R.; Holmes, R. J. *Nano Letters* **2010**, *10(4)*, 1154-1157.

Cheng, K.; Anthony, R.; Kortshagen, U. R.; Holmes, R. J. *Nano Letters* **2011**, *11(5) 1952-1956*.

Cheylan, S.; Elliman, R. G. *Applied Physics Letters* **2001**, *78*, 1912-1914.

Chitara, B.; Bhat, S. V.; Vivekchand, S. R. C.; Gomathi, A.; Rao, C. N. R. *Solid State Communications* **2008**, *147*, 409-413.

Cho, K. S.; Park, N.; Kim, T.; Kim, K.; Sung, G. Y. *Applied Physics Letters* **2005**, *86*.

Coe, S.; Woo, W.; Bawendi, M.; Bulovic, V. *nature* **2002**, *420*, 800-803.

Coe-Sullivan, S.; Woo, W.; Steckel, J. S.; Bawendi, M.; Bulovic, V. *Organic Electronics* **2003**, *4*, 123-130.

Colvin, V. L.; Schlamp, M. C.; Alivisatos, A. P. *Nature* **1994**, *370*, 354-357.

Comedi, D.; Zalloum, O. H. Y.; Mascher, P. *Applied Physics Letters* **2005**, *87*.

Comedi, D.; Zalloum, O. H. Y.; Wojcik, J.; Mascher, P. *IEEE Journal of Selected Topics in Quantum Electronics* **2006**, *12*, 1561-1569.

Credo, G. M.; Mason, M. D.; Buratto, S. K. *Applied Physics Letters* **1999**, *74*, 1978-1980.

Cullis, A. G.; Canham, L. T. *Nature* **1991**, *353*, 335-338.

Dabbousi, B. O.; Bawendi, M. G.; Onitsuka, O.; Rubner, M. F. *Applied Physics Letters* **1995**, *66*, 1316-1318.

Damilano, B.; Grandjean, N.; Massies, J.; Semond, F. *Applied Surface Science* **2000**, *164*, 241-245.

Daouahi, M.; Ben Othmane, A.; Zellama, K.; Zeinert, A.; Essamet, M.; Bouchriha, H. *Solid State Communications* **2001**, *120*, 243-248.

Delerue, C.; Allan, G.; Lannoo, M. *Physical Review B* **2001**, *64*.

EERE: Solid-State Lighting Home Page **2010**.

English, D. S.; Pell, L. E.; Yu, Z.; Barbara, P. F.; Korgel, B. A. *Nano Letters* **2002**, *2*, 681-685.

Erogbogbo, F.; Yong, K.; Roy, I.; Xu, G.; Prasad, P. N.; Swihart, M. T. *ACS Nano* **2008**, *2*, 873-878.

Gao, J.; Luther, J. M.; Semonin, O. E.; Ellingson, R. J.; Nozik, A. J.; Beard, M. C. *Nano Letters* **2011**, *11*, 1002-1008.

Garcia, R.; Thomas, A.; Bell, A.; Stevens, M.; Ponce, F. A. *Materials Research Society Symposium Proceedings* **2004**, *798*.

Garrido Fernandez, B.; Lopez, M.; Garcia, C.; Perez-Rodriguez, A.; Morante, J. R.; Bonafos, C.; Carrada, M.; Claverie, A. *Journal of Applied Physics* **2002**, *91*, 798-807.

Gates, S. M.; Greenlief, C. M.; Beach, D. B. *Journal of Chemical Physics* **1990**, *93*, 7493-7503.

Godefroo, S.; Hayne, M.; Jivanescu, M.; Stesmans, A.; Zacharias, M.; Lebedev, O. I.; van Tendeloo, G.; Moshchalkov, V. V. *Nature Nanotechnology* **2008**, *3*, 174-179.

Goodwin, T. J.; Leppert, V. J.; Risbud, S. H.; Kennedy, I. M.; Lee, H. W. H. *Applied Physics Letters* **1997**, *70*, 2133-2124.

Gresback, R.; Holman, Z.; Kortshagen, U. *Applied Physics Letters* **2007**, *91*.

Gresback, R.; Holman, Z.; Kortshagen, U. *Applied Physics Letters* **2007**, *91*.

Gresback, R.; Hue, R.; Gladfelter, W. L.; Kortshagen, U. R. *Nanoscale Research Letters* **2011**, *68*.

Gupta, A.; Swihart, M. T.; Wiggers, H. *Advanced Functional Materials* **2009**, *19*, 696-703.

Gupta, A.; Wiggers, H. *Nanotechnology* **2011**, *22*.

Gupta, P.; Colvin, V. L.; George, S. M. *Physical Review B* **1988**, *37*, 8234-8243.

Gur, I.; Fromer, N. A.; Geier, M. L.; Alivisatos, A. P. *Science* **2005**, *310*, 462-471.

Hao, H. L.; Shen, W. Z. *Nanotechnology* **2008**, *19*.

Haverinen, H. M.; Myllyla, R. A.; Jabbour, G. E. *Journal of Display Technology* **2010**, *6*, 87-89.

Herring, C.; Johnson, N. M.; Van de Walle, C. G. *Physical Review B 64*.

Hines, M. A.; Guyot-Sionnest, P. *Journal of Physical Chemistry* **1996**, *100*, 468-471.

Hirschman, K. D.; Tsybeskov, L.; Duttagupta, S. P.; Fauchet, P. M. *Nature* **1996**, *384*, 338-341.

Holm, J.; Roberts, J. T. *Journal of Physical Chemistry C* **2009**, *113*, 15955-15963.

Holm, J.; Roberts, J. T. *Journal of Vacuum Science and Technology* **2010**, *28*, 161-169.

Holman, Z. C.; Kortshagen, U. R. *Langmuir* **2009**, *25*, 11883-11889.

Holman, Z. C.; Kortshagen, U. R. *Nanotechnology* **2010**, *21*.

Holmes, J. D.; Ziegler, K. J.; Doty, R. C.; Pell, L. E.; Johnston, K. P.; Korgel, B. A. *Journal of the American Chemistry Society* **2001**, *123*, 3743-3748.

Honda, Tohru; Akiyama, Miwako; Egawa, Shinichi; Aoki, Yohta; Obinata, Naoyuki; Kawanishi, Hideo. *physics status solidi (a)* **2004**, *201*, 2814-2817.

Hoshino, K.; Arakawa, Y. *Journal of Crystal Growth* **2004**, *272*, 161-166.

Hua, F.; Swihart, M. T.; Ruckenstein, E. *Langmuir* **2005**, *21*, 6054-6062.

Huh, C.; Kim, K.; Kim, B. K.; Kim, W.; Ko, H.; Choi, C.; Sung, G. Y. *Advanced Materials* **2010**, *2010*, 5058-5062.

Independent Statistics and Analysis: U. S. Energy Information Administration **2003**.

Irrera, A.; Iacona, F.; Crupi, I.; Presti, C. D.; Franzo, G.; Bongiorno, C.; Sanfilippo, D.; Di Stefano, G.; Piana, A.; Fallica, P. G.; Canino, A.; Priolo, F. *Nanotechnology* **2006**, *17*, 1428-1436.

Jung, Y.; Yoon, J.; Elliman, R. G.; Wilkinson, A. R. *Journal of Applied Physics* **2008**, *104*.

Jurbergs, D.; Rogojina, E.; Mangolini, L.; Kortshagen, U. *Applied Physics Letters* **2006**, *88*.

Kapaklis, V.; Politis, C.; Poulopoulos, P.; Schweiss, P. *Applied Physics Letters* **2005**, *87*.

Kendrick, C.E.; Anderson, P.A.; Kinsey, R. J.; Kennedy, V. J.; Markwitz, A.; Asadov, A.; Gao, W.; Reeves, R. J.; Durbin, S. M. *physics status solidi (c)* **2005**, *2*, 2236-2239.

Kessels, W. M. M.; Nadir, K.; van de Sanden, M. C. M. *Journal of Applied Physics* **2006**, *99*.

Kim, B.; Cho, C.; Kim, T.; Park, N.; Sung, G. Y.; Park, S. *Applied Physics Letters* **2005**, *86*.

Kim, S.; Park, Y. M.; Choi, S.; Kim, K. J. *Journal of Applied Physics* **2007**, *101*.

Kim, T.; Cho, K.; Lee, E. K.; Lee, S. J.; Chae, J.; Kim, J. W.; Kim, D. H.; Kwon, J.; Amaratunga, G.; Lee, S. Y.; Choi, B. L.; Kuk, Y.; Kim, J. M.; Kim, K. *Nautre Photonics* **2011**, *5*, 176-182.

Kisailus, D.; Choi, J. H.; Lange, F. F. *Journal of Crystal Growth* **2003**, *249*, 106-120.

Kudrawiec, R.; Nyk, M.; Syperek, M.; Podhorodecki, A.; Misiewicz, J. *Applied Physics Letters* **2006**, *88*.

Ledoux, G.; Gong, J.; Huisken, F.; Guillois, O.; Reynaud, C. *Applied Physics Letters* **2002**, *80*, 4834-4836.

Lee, K. J.; Lee, J.; Hwang, H.; Reitmeier, Z. J.; Davis, R. F.; Rogers, J. A.; Nuzzo, R. G. *Small* **2005**, *1*, 1164-1168.

Li, X.; He, Y.; Talukdar, S. S.; Swihart, M. T. *Langmuir* **2003**, *19*, 8490-8496.

Ligman, R. K.; Mangolini, L.; Kortshagen, U. R.; Campbell, S. A. *Applied Physics Letters* **2007**, *90*.

Littau, K. A.; Szajowski, P. J.; Muller, A. J.; Kortan, A. .. R.; Brus, L. E. *Journal of Physical Chemistry B* **1993**, *97*, 1224-1230.

Liu, C.; Holman, Z. C.; Kortshagen, U. R. *Nano Letters* **2009**, *9*, 449-452.

Liu, Q.; Kauzlarich, S. M. *Materials Science and Engineering B96* **2002**, 72-75.

Lu, Z. H.; Lockwood, D. J.; Baribeau, J. *Nature* **1995**, *378*, 258-260.

Mangolini, L. Non-thermal plasma synthesis and passivation of luminescent silicon nanocrystals. Ph.D. Thesis, University of Minnesota: Minneapolis, MN, 2007.

Mangolini, L.; Jurbergs, D.; Rogojina, E.; Kortshagen, U. *Journal of Luminescence* **2006**, *121*, 327-334.

Mangolini, L.; Jurbergs, D.; Rogojina, E.; Kortshagen, U. *physics status solidi (c)* **2006**, *3*, 3975-3978.

Mangolini, L.; Kortshagen, U. *Advanced Materials* **2007**, *19*, 2513-2519.

Mangolini, L.; Kortshagen, U. *Physical Review E* **2009**, *79*.

Mangolini, L.; Thimsen, E.; Kortshagen, U. *Nano Letters* **2005**, *5*, 655-659.

Marra, D. C.; Edelberg, E. A.; Naone, R. L.; Aydil, E. S. *Journal of Vacuum Science and Technology A* **1998**, *16*, 3199-3210.

Martin, P.; Fernandez, J. F.; Sanchez, C. *Materials Science and Engineering B* **2004**, *B108*, 166-170.

Matsumoto, T.; Belogorokhov, A. I.; Belogorokhova, L. I.; Masumoto, Y.; Zhukov, E. A. *Nanotechnology* **2000**, *11*, 340.

Min, K. S.; Shcheglov, K. V.; Yang, C. M.; Atwater, H. A.; Brongersma, M. L.; Polman, A. *Applied Physics Letters* **1996**, *69*, 2033-2035.

Molinari, M.; Rinnert, H.; Vergnat, M. *Europhysics Letters* **2004**, *66*, 674-679.

Monelli, A.; Corni, F.; Tonini, R.; Ferrari, C.; Ottaviani, G. *Journal of Applied Physics* **1996**, *80*, 109-114.

Narukawa, Y.; Ichikawa, M.; Sanga, D.; Sano, M.; Mukai, T. *Journal of Physics D: Appled Physics* **2010**, *43*.

Niesar, S.; Stegner, A. R.; Pereira, R. N.; Hoeb, M.; Wiggers, H.; Brandt, M. S.; Stutzmann, M. *Applied Physics Letters* **2010**, *96*.

Niu, Y.; Munro, A. M.; Cheng, Y.; Tian, Y.; Liu, M. S.; Zhao, J.; Bardecker, J. A.; Jen-La Plante, I.; Ginger, D. S.; Jen, A. K. *Advanced Materials* **2007**, *19*, 3371-3376.

Nozaki, T.; Sasaki, K.; Ogino, T.; Asahi, D.; Okazaki, K. *Nanotechnology* **2007**, *18*.

Ogi, Takashi; Itoh, Yoshifumi; Abdullah, Mikrajuddin; Iskandar, Ferry; Azuma, Yasushi; Okuyama, Kikuo *Journal* **2005**, *281*, 234-241.

Onischuk, A. A.; Levykin, A. I.; Strunin, V. P.; Ushakova, M. A.; Samoilova, R. I.; Sabelfeld, K. K.; Panfilov, V. N. *Journal of Aerosol Science* **2000**, *31*, 879-906.

Osedach, T. P.; Geyer, S. M.; Ho, J. C.; Arango, A. C.; Bawendi, M. G.; Bulovic, V. *Applied Physics Letters* **2009**, *94*.

Park, N.; Choi, C.; Seong, T.; Park, S. *Physical Review Letters* **2001**, *86*, 1355-1357.

Park, N.; Kim, T.; Park, S. *Applied Physics Letters* **2001**, *78*, 2575-2577.

Pellegrino, P.; Garrido, B.; Garcia, C.; Ferre, R.; Moreno, J. A.; Morante, J. R. *Physica E* **2003**, *16*, 424-428.

Pi, X. D.; Kortshagen, U. *Nanotechnology* **2009**, *20*.

Pi, X. D.; Zalloum, O. H. Y.; Roschuk, T.; Wojcik, J.; Knights, A. P.; Mascher, P.; Simpson, P. J. *Applied Physics Letters* **2006**, *88*.

Pierret, R. F. *Advanced Semiconductor Fundamentals*; Modular Series on Solid State Devices; Second Edition.; Pearson Education, Inc.: Upper Saddle River, New Jersey, 2003; Vol. VI.

Poling, B. E.; Prausnitz, J. M.; O'Connell, J. *Properties of Gases and Liquids*, 5th edition, McGraw-Hill, (2000)

Puzzo, D. P.; Henderson, E. J.; Helander, M. G.; Wang, Z.; Ozin, G. A.; Lu, Z. *Nano Letters ASAP*.

Reshchikov, M. A.; Moon, Y. T.; Gu, X.; Nemeth, B.; Nause, J.; Morkoc, H. *Physica B* **2006**, *376-377*, 715-718.

Rinnert, H.; Vergnat, M.; Marchal, G.; Burneau, A. *Applied Physics Letters* **1998**, *72*, 3157-3159.

Rivolo, P.; Geobaldo, F.; Rocchia, M.; Amato, G.; Rossi, A. M.; Garrone, E. *physica status solidi (a)* **2003**, *197*, 217-221.

Roura, P.; Farjas, J.; Rath, C.; Serra-Miralles, J.; Bertran, E.; Roca i Cabarrocas, P. *Physical Review B* **2006**, *73*.

Salivati, N.; Ekerdt, J. G. *Surface Science* **2009**, *603*, 1121-1125.

Sankaran, R. M.; Holunga, D.; Flagan, R. C.; Giapis, K. P. *Nano Letters* **2005**, *5*, 537-541.

Sankaran, R. M.; Holunga, D.; Flagan, R. C.; Giapis, K. P. *Nano Letters* **2005**, *5*, 537-541.

Santato, C.; Manunza, I.; Bonfiglio, A.; Cicoira, F.; Cosseddu, P.; Zamboni, R.; Muccini, M. *Applied Physics Letters* **2005**, *86*.

Schrage, C.; Kaskel, S. *ACS Applied Materials & Interfaces* **2009**, *1*, 1640-1644.

Seo, J.; Kim, S. J.; Kim, W. J.; Singh, R.; Samoc, M.; Cartwright, A. N.; Prasad, P. N. *Nanotechnology* **2009**, *20*.

Seraphin, A. A.; Ngiam, S.; Kolenbrander, K. D. *Journal of Applied Physics* **1996**, *80*, 6429-6433.

Shen, P.; Uesawa, N.; Inasawa, S.; Yamaguchi, Y. *Journal of Materials Chemistry* **2010**, *20*, 1669-1675.

Shimada, M.; Azuma, Y.; Okuyama, K.; Hayashi, Y.; Tanabe, E *Japanese Journal of Applied Physics* **2006**, *45*, 328-332.

Sirenko, A. A.; Fox, J. R.; Akimov, I. A.; Xi, X. X.; Ruvimov, S.; Liliental-Weber, Z. *Solid State Communications* **2000**, *113*, 553-558.

Stouwdam, J. W.; Janssen, R. A. J. *Journal of Materials Chemistry* **2008**, *18*, 1889-1894.

Stutzmann, M.; Biegelsen, D. K. *Physical Review B* **1989**, *40*, 9834-9840.

Sun, Q.; Subramanyam, G.; Dai, L.; Check, M.; Campbell, A.; Naik, R.; Grote, J.; Wang, Y. *ACS Nano* **2009**, *3*, 737-743.

Svrcek, V.; Mariotti, D.; Shibata, Y.; Kondo, M. *Journal of Physics D: Appled Physics* **2010**, *43*.

Talapin, D. V.; Murray, C. B. *Science* **2005**, *310*, 86-89.

Talgorn, E.; Moysidou, E.; Abellon, R. D.; Savenije, T. J.; Goossens, A.; Houtepen, A. J.; Siebbeles, L. D. A. *Journal of Physical Chemistry C* **2010**, *114*, 3441-3447.

Tan, Z.; Xu, J.; Zhang, C.; Zhu, T.; Zhang, F.; Hedrick, B.; Pickering, S.; Wu, J.; Su, H.; Gao, S.; Wang, A. Y.; Kimball, B.; Ruzyllo, J.; Dellas, N. S.; Mohney, S. E. *Journal of Applied Physics* **2009**, *105*.

Tang, C. W.; VanSlyke, S. A. *Applied Physics Letters* **1987**, *51*, 913-915.

Tang, H.; Webb, J. B.; Bardwell, J. A.; Raymond, S.; Salzman, Joseph; Uzan-Saguy, C. *Applied Physics Letters* **2001**, *78*, 757-759.

Tippins, H.H. *Physical Review* **1965**, *A 140*, 317-319.

Tripathi, V.; Nazrul Islam, M.; Mohapatra, Y. N.; Roca i Cabarrocas, P. *The European Physical Journal Applied Physics* **2007**, *39*, 203-209.

Valenta, J.; Fucikova, A.; Vacha, F.; Adamec, F.; Humpolickova, J.; Hof, M.; Pelant, I.; Kusova, K.; Dohnalova, K.; Linnros, J. *Advanced Functional Materials* **2008**, *18*, 2666-2672.

Walters, R. J.; Kalkman, J.; Polman, A.; Atwater, H. A.; de Dood, M. J. A. *Physical Review B* **2006**, *73*.

Wang, L.; Zunger, A. *Journal of Physical Chemistry* **1994**, *98*, 2158-2165.

Wang, M.; Anopchenko, A.; Marconi, A.; Moser, E.; Prezioso, S.; Pavesi, L.; Pucker, G.; Bellutti, P.; Vanzetti, L. *Physica E* **2009**, *41*, 912-915.

Wang, Y. Q.; Chen, W. D.; Liao, X. B.; Cao, Z. X. *Nanotechnology* **2003**, *14*, 1235-1238.

Wang, Y. Q.; Kong, G. L.; Chen, W. D.; Diao, H. W.; Chen, C. Y.; Zhang, S. B.; Liao, X. B. *Applied Physics Letters* **2002**, *81*, 4174-4176.

Weaver, M. S.; Michalski, L. A.; Rajan, K.; Rothman, M. A.; Silvernail, J. A.; Brown, J. J.; Burrows, P. E.; Graff, G. L.; Gross, M. E.; Martin, P. M.; Hall, M.; Mast, E.; Bonham, C.; Bennett, W.; Zumhoff, M. *Applied Physics Letters* **2002**, *81*, 2929-2931.

Willander, M.; Nur, O.; Bano, N.; Sultana, K. *New Journal of Physics* **2009**, *11*.

Wills, A. W.; Kang, M. S.; Khare, A.; Gladfelter, W. L.; Norris, D. J. *ACS Nano* **2010**, *4*, 4523-4530.

Wood, V.; Panzer, M. J.; Caruge, J.; Halpert, J. E.; Bawendi, M. G.; Bulovic, V. *Nano Letters* **2010**, *2010*, 24-29.

Wood, V.; Panzer, M. J.; Chen, J.; Bradley, M. S.; Halpert, J. E.; Bawendi, M. G.; Bulovic, V. *Advanced Materials* **2009**, *21*, 2151-2155.

Xiao, Hong-Di; Ma, Hong-Lei; Xue, Cheng-Shan; Zhuang, Hui-Zhao; Ma, Jin; Zong, Fu-Jian; Hu, Wen-Rong *Materials Letters* **2005**, *59*, 4041-4043.

Xie, Z.; Zhu, J.; Zhang, M.; Zhao, Y.; Lu, M. *Applied Surface Science* **2009**, *255*, 3833-3836.

Yanagisawa, S.; Sato, K.; Hirakuri, K. *Thin Solid Films* **2007**, *515*, 7990-7993.

Yu, W.; Zhang, J. Y.; Ding, W. G.; Fu, G. S. *European Physical Journal B* **2007**, *57*, 53-56.

Zhou, Y.; Riehle, F. S.; Yuan, Y.; Schleiermacher, H.; Niggemann, M.; Urban, G. A.; Kruger, M. *Applied Physics Letters* **2010**, *96*.

Zhu, X. -.; Boiadjiev, V.; Mulder, J. A.; Hsung, R. P.; Major, R. C. *Langmuir* **2000**, *16*, 6766-6772.

Zunger, A.; Wang, L. *Applied Surface Science* **1996**, *102*, 350-359.

Appendix A: Additional work on crystalline and amorphous silicon nanoparticles

In studying the effects of input power on plasma-produced silicon nanoparticles, we performed some additional measurements that were not published, but may be useful for future students. In particular, the surface bonding of the nanoparticles was studied as a function of input power, and we found that the input power (and hence, crystallinity) of the nanoparticles influenced the structure of surface hydrogen bonding. The FTIR spectra from nanoparticles produced at different reactor powers is shown in Figure A1.

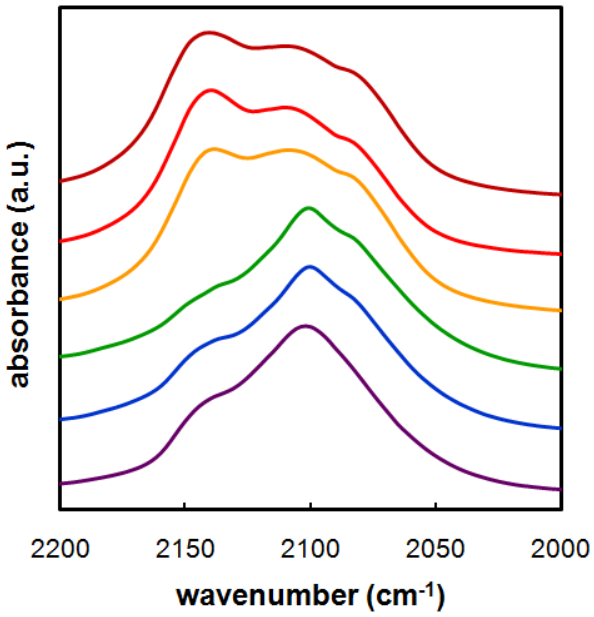

Figure A1: FTIR spectra from SiNCs made with different reactor powers.

This result is interesting because it indicates that the nanoparticle surface also changes with crystallinity and input power. While we concluded that the silicon nanoparticle

structure determines the PL QY, it's possible that the surface also plays a role here which we have not investigated. It would be an interesting study to try to use the surface hydrogen structure of plasma-produced nanoparticles to predict the crystallinity of the sample, or to predict ultimate quantum yield. In addition, SiNCs on the small side of the possible size range possible using the plasma reactor often exhibit reduced QY compared to larger SiNCs—and this is accompanied by a surface structure more akin to that seen for particles produced with lower power. Future work could focus on changing the surface of these smallest SiNCs to yield a hydride structure with a predominance of di- and tri-hydrides: this may lead to more higher-efficiency light emission.

Appendix B: Supporting information on gas injection studies

In the write-up of this work, we chose Ar, He, H_2, and D_2 as injection gases for presentation. However, we also performed experiments under complete omission of the injection gas flow. The pressure in the reactor remained constant due to the feedback-monitored throttle valve, even without this additional gas flow. The results were surprising, and indicated that the scenario of "no injection" yielded SiNCs with PL QYs between those of Ar and He injection (see Fig. B1). One proposed reason that argon injection would be more detrimental to the optical quality of the SiNCs than a complete omission of injection gas is that the argon gas is more likely to absorb the afterglow plasma energy and generate additional excited and ionized species,

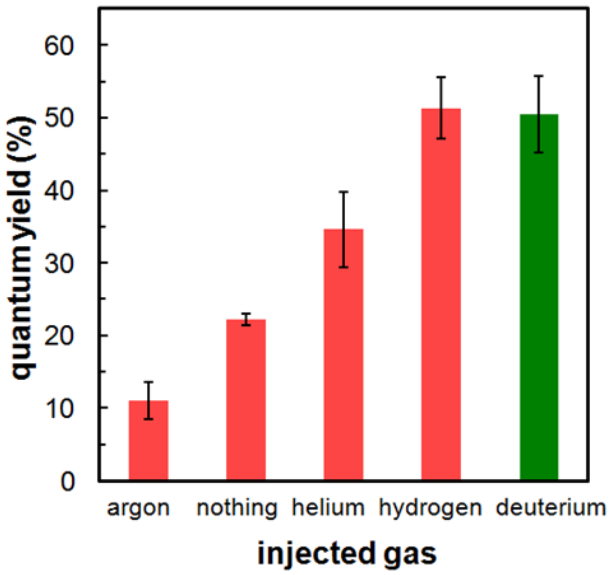

Figure B1: PL QYs from SiNCs made with injection of different gases, including no gas, into the afterglow of the synthesis plasma.

contributing to the SiNC temperature in the afterglow region. This could cause even more changes to the SiNC surface than if there were no gas injection. An idea for future work is to model the SiNC-afterglow scenario using computational methods and examine the effects on SiNC temperature upon injection of different gases or injection gas omission.

Some additional experiments have indicated that the location of gas injection is important in achieving high QY from these SiNCs. We performed a series of experiments in which we shifted the gas injection further downstream from its initial position by approximately 5cm. In this region of the tube, there is no plasma afterglow visible to the eye. Schematics of the experiment are shown in Fig. B2. For these experiments, the SiNCs had PL QYs comparable to those for the "no injection" scenario, even when an additional low-power plasma was ignited near this lower injection region (Fig. B3).

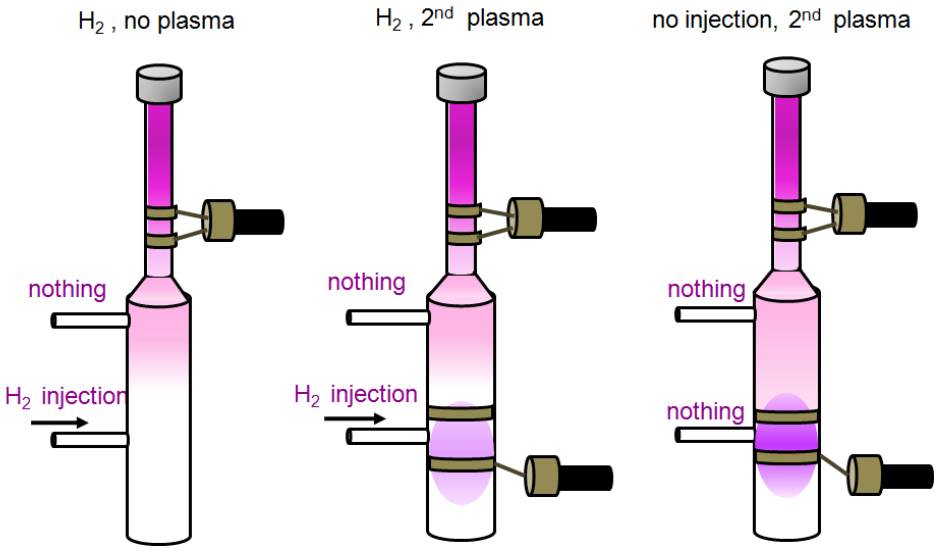

Figure B2: Schematics of the three scenarios of shifted injection-region experiments.

These results indicate that the effects of gas and particle temperature quenching and additional passivation with hydrogen must occur shortly after the SiNCs exit the nucleation and growth region of the plasma.

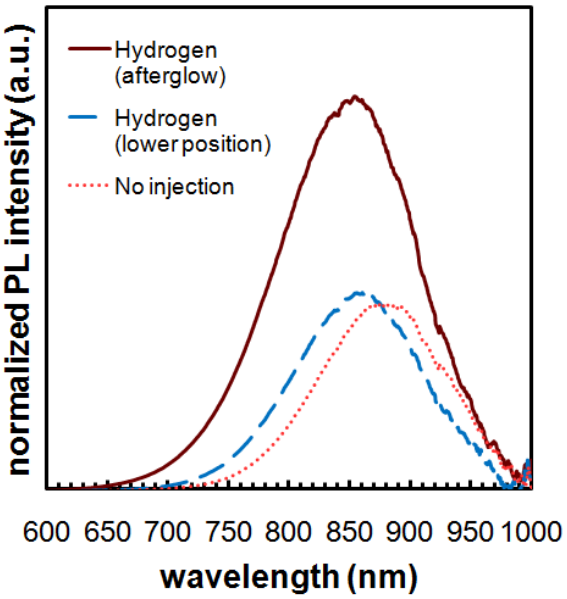

Figure B3: PL spectra of SiNCs produced without injection and using shifted gas injection.

To estimate the time necessary for back diffusion from the position of hydrogen injection to the beginning of the expansion region, we use the simple relation for the characteristic diffusion time from solving Fick's law:

$$l_{diff} = \sqrt{4D_{ab}t_{diff}} \Rightarrow t_{diff} = \frac{{l_{diff}}^2}{4D_{ab}} \Rightarrow t_{diff} = \frac{(4.0cm)^2}{4\left(421.6cm^2/s\right)} \Rightarrow t_{diff} = 9.5ms$$

where l_{diff} is the characteristic diffusion length, t_{diff} is the characteristic time, and D_{ab} is the binary diffusion coefficient of hydrogen and argon. We can measure l_{diff} = 4.0 cm directly from the geometry of the reactor tube, and use the Chapman-Enskog relation[S1] evaluated at 25°C and 1.4 Torr to estimate D_{ab} = 421.6 cm^2/s.

Comparatively, to estimate the time that it would take the forced flow convection to move gas from the end of the main plasma zone, we simply divide the volume of reactor being traveled by the standard volumetric flow rate corrected to the actual pressure:

$$t_{conv} = \frac{l_{cons}A_{cons}}{Q\frac{P_{std}}{P_{act}}} + \frac{l_{\exp}A_{\exp}}{Q\frac{P_{std}}{P_{act}}} = \frac{(2.5cm)(0.238cm^2)}{\left(48cm^3/min\right)\left(\frac{760torr}{1.4torr}\right)} + \frac{(1.5cm)(0.865cm^2)}{\left(48cm^3/min\right)\left(\frac{760torr}{1.4torr}\right)} = 4.4ms$$

where t_{conv} is the time for convective flow to travel from the plasma region to the injection location, l_{cons} and l_{exp} are the lengths of the reactor in the constricted and expanded regions, respectively, such that $l_{cons} + l_{exp} = l_{diff} = 4.0$cm, A_{cons} and A_{exp} are the cross sectional areas of the constricted and expanded regions, respectively, Q is the standard flow rate, P_{std} is the standard pressure, and P_{act} is the actual pressure measured in the system and is assumed constant at 1.4 Torr.

References:

(B1) Poling, B. E.; Prausnitz, J. M.; O'Connell, J. *Properties of Gases and Liquids*, 5th edition, McGraw-Hill, (2000)

Appendix C: Additional measurements on gas-phase-impacted SiNC films

C.1 Film density measurements

To confirm the density of the SiNC films created in the gas-phase impaction scheme, we carried out measurements as is described in detail in Ref. [C1]. Specifically, we deposited films on gold-coated silicon and measured the true film thickness using scanning electron microscopy (SEM). We then used Rutherford backscattering (RBS) to calculate the thickness of the film if it were bulk silicon, rather than in discrete

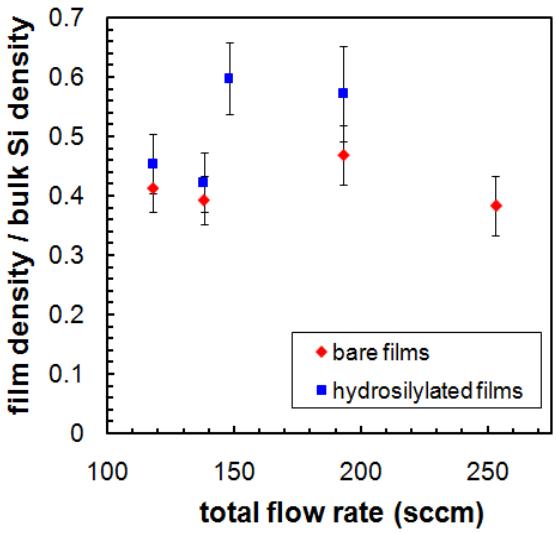

Figure C1: results of film density measurements using a combination of SEM and RBS. The measurements were completed on both gas-phase-functionalized (hydrosilylated) and bare SiNC films.

nanocrystals separated by gas and ligands. By comparing these two measurements, we can calculate the density of the actual film. We performed these measurements using

SiNCs of different sizes, a parameter which is adjusted by tuning the total gas flowrate through the reactor. While pressures varied slightly depending on gas flowrate and orifice size, the goal was to keep the pressure in the reactor near 1.4 Torr. The results of this calculation are plotted in Figure C1, versus the total gas flowrate. For these measurements, the ratio between the pressures upstream and downstream of the slit orifice were between 7:1 and 10:1.

C.2 Film PL measurements

While the SiNCs used for construction of the LED were made under specific flowrate conditions to obtain NIR-emitting SiNCs, we also changed the flowrate and orifice slit width to examine films made from SiNCs of different sizes. We tried to maintain a pressure of near 1.4 Torr through adjustments to the orifice width and flowrates. While we measured the PL from films of bare and functionalized SiNCs, here we present only the PL data from the gas-phase-functionalized impacted films. We measured the photoluminescence peaks of each sample using the PTI Spectrometer in Professor Russell J. Holmes' laboratory in the Chemical Engineering and Materials Science department. That spectrometer uses a Xenon light source equipped with a chopper and monochromator to excite the samples at specific wavelengths, and the light is collected using a photomultiplier tube (in the case of visible-light-emitting samples) or an indium gallium arsenide (InGaAs) detector for infrared-emitting samples. We continued to monitor the PL peaks over the course of a week to see the effects of

oxidation on the film PL. The films were kept in the laboratory exposed to ambient conditions following their initial exposure to air, just prior to the PL measurements.

The results of these measurements are plotted in Figure C2. Over the course of the week, the peak PL of each sample undergoes a blueshift consistent with oxidation of SiNCs. After several days, this blueshift has apparently ceased progressing. This is interesting, as solution-dispersed SiNCs undergo a more dramatic blueshift that takes place over a longer period of time (Figure C2b). There are two possible reasons for premature cessation of blueshift of the gas-phase-functionalized impacted films in comparison with bare, dispersed SiNCs. One hypothesis is that the functionalization of the SiNCs in films may sterically hinder the oxidation of the nanocrystals, preventing a complete oxide shell from growing, whereas for the dispersed particles, there were no ligands attached. However, the degree of capping provided in the gas-phase route is sufficient solubilizing the SiNCs, but is not as complete as in the liquid-phase functionalization step—and the PL peaks measured on bare SiNC films demonstrate the same approximate blueshift as the gas-phase-functionalized films. This indicates that the functionalization in the gas-phase is not enough to present a steric barrier to the complete oxidation of the SiNCs. A more plausible possibility is that the density of the films leads to oxidation of only the top several monolayers of SiNCs, while the majority of the SiNCs in these films remain relatively unaffected by oxygen. Therefore, the ensemble PL from the SiNC films shifts relatively little in comparison to the dispersed SiNCs, which were in a fairly dilute solution such that oxygen could easily interact with their surfaces.

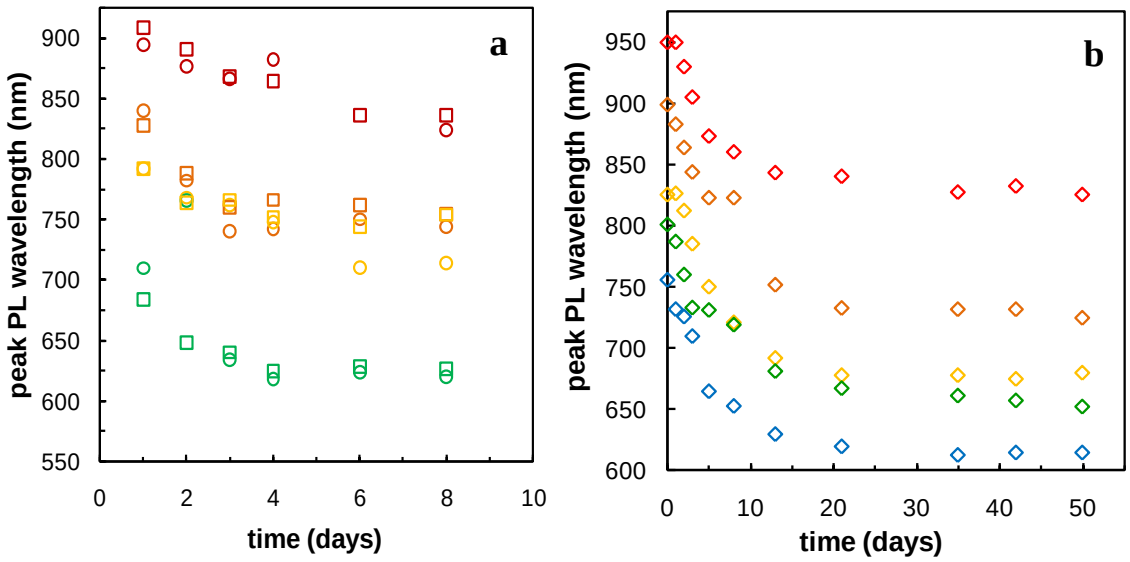

Figure C2: Peak PL wavelengths of SiNCs as a function of aging time in ambient conditions. (a) SiNC impacted film PL data: square symbols represent films from gas-phase-functionalized SiNCs, and circles represent bare SiNC films. (b) PL data from bare SiNCs dispersed in chloroform during aging.

Comparisons of the FWHM for film vs solution spectra at t=8 days indicate that, even after only 8 days of air exposure, there may be slightly more spectrum widening for the film samples, which could allude to a reduced oxidation of some of the buried film layers. However, a study over time scales closer to 1 month would be more conclusive, as a longer time would allow for more equilibration of the oxidation process in both solution and films. Unfortunately, we stopped taking data after 8 days for the SiNC films, so the experiment would need to be repeated to acquire more detailed data on comparative spectra linewideths, and provide a more conclusive answer about the oxidation of SiNCs contingent on environment. An interesting experiment would be to age functionalized, solubilized SiNCs to compare their PL peak shifts to the data presented here, and draw some conclusions about the rate of oxidation of various forms of SiNCs.

References:

(C1) Holman, Z. C.; Kortshagen, U. R. *Nanotechnology* **2010**, *21*.

Appendix D: Details regarding SiNC preparation for the hybrid SiNC-organic LED project

Some of the exact procedures used in processing the SiNCs are listed in this section. For construction of the device, the weight of the SiNCs was necessary—and so several steps were required to measure an accurate mass of the SiNC-ligand system. After the functionalization step, the SiNCs were dried on the Schlenk line and then redispersed in dried, degassed chloroform. The chloroform/SiNC colloid was passed through a 200μm pore size PTFE filter using a special cannula, to remove any large agglomerates, and transferred into a cleaned vial of known weight. The chloroform was then evaporated using the Schlenk line and the final weight of the vial was recorded, to give a net SiNC+ligand weight. Typically, for 1 hour of SiNC collection and functionalization using the 5:1 solvent mixture, the weight of the sample was ~20mg. To prevent UV damage of the SiNCs from room lights or sunlight, the sample vials were wrapped in aluminum foil for both of the drying steps, and during storage. The samples were transferred air-free to the Holmes laboratory and dispersed in chloroform for spin-casting onto the device substrates.

Appendix E: Synthesis and characterization of gallium nitride (GaN) nanocrystals by nonthermal plasma reactor

E.1 Introduction

Gallium nitride (GaN) is emerging as a one of the leading choices in optoelectronic devices. The direct bandgap of GaN makes it an especially efficient energy absorber and emitter, with stable emission over time and a good tolerance for high heat. The bandgap of GaN is a wide 3.4eV, enabling its use in ultraviolet/ blue light emission technologies. Furthermore, the relative non-toxicity of GaN, especially compared to other popular semiconductors such as cadmium selenide (CdSe), gives it a distinct advantage. The applicability of GaN nanoparticles lies in high-brightness solid-state lighting devices.[1-3] Doping of GaN and incorporation of other semiconductors could enable devices that span the visible spectrum.[4-7] New methods are emerging that combine nanocrystals with organic semiconductors for inexpensive and high-efficiency light-emitting devices (LEDs).[8-10] Also, the surfacing technology of using layers of nanocrystals in photovoltaic devices expands the potential of GaN nanocrystals into devices that emulate organic solar cells.[11,12]

One obstacle in realizing the high efficiency of GaN devices is the necessity of a defect-free crystal lattice. Because GaN is grown epitaxially in many cases, and because finding a matched lattice substrate is difficult, the growth of defect-free GaN crystals is challenging. By growing freestanding GaN nanocrystals, the substrate mismatch problem

can be sidestepped, possibly reducing lattice defects. Use of GaN nanoparticles in devices is becoming increasingly popular as the versatility and efficiency of these particles continue to grow. Methods for GaN nanoparticle synthesis include reactive laser ablation,[13] metal-organic chemical vapor deposition (MOCVD),[14] thermal reactions,[15,16] and mechanical grinding of powders.[2] However, these methods can be time- and energy- consuming. Using plasmas for GaN nanocrystal synthesis, however, is an attractive process, because plasmas provide the reactive environment necessary for stoichiometric synthesis of GaN without the applied high temperatures which are typically required.[17] The plasma reactor has been shown to be an elegant high-yield synthesis route for group IV nanocrystals such as silicon and germanium as well as for compound materials such as indium phosphide and Si-Ge alloys.[18-21] Here, we report results on the fabrication of GaN nanocrystals using a nonthermal plasma reactor, and the photoluminescence from these nanocrystals.

E.2 Experimental details

The reactor consists of a 1.27 cm O.D. quartz tube with two ring electrodes encircling the tube. Figure E1 shows a schematic of the reactor used for these experiments. Trimethylgallium ($Ga(CH_3)_3$, TMGa) was used as a gallium precursor, and vapor of this metal-organic liquid was carried into the reactor by nitrogen or argon gas. The total TMGa vapor flowrate was around 1 sccm. Ammonia gas (NH_3) was the nitrogen source for the reaction, at a flowrate from 10-30 sccm. Pressure inside the tube was maintained at 10-30 Torr using a manually-operated butterfly valve. RF power at

13.56 MHz and ~100 W (nominal) was supplied through a matching network to the ring electrodes. Upon entering the discharge region, the precursor gases dissociated, nucleating GaN nanoparticles which were then collected on a stainless steel mesh.

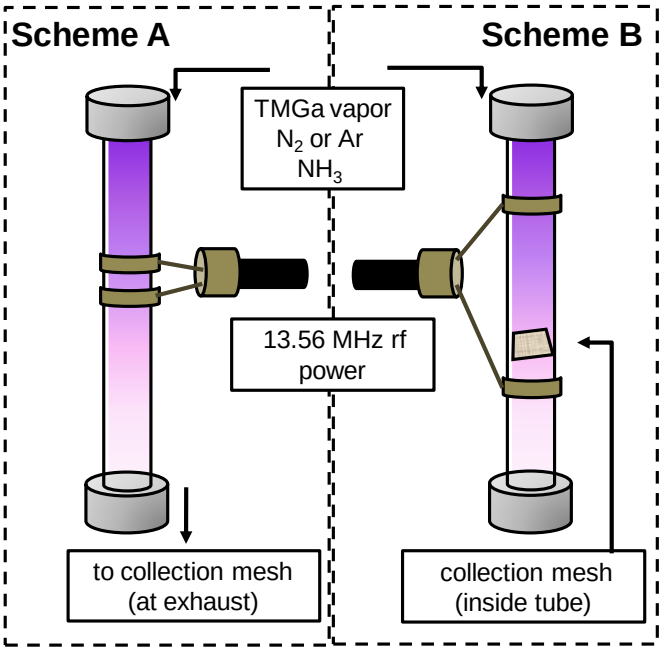

Figure E1: Schemes for synthesis and collection of GaN nanocrystals.

In these experiments, two collection schemes were utilized: in Scheme A, the nanoparticles were collected on the mesh at the exhaust region of the reactor. In Scheme B, the mesh was inserted into the reactor tube below the ring electrode and the particles were collected there. Crystallinity of the GaN nanocrystals was studied by x-ray diffraction (XRD) using a Bruker Microdiffractometer. The nanocrystals were also studied using transmission electron microscopy (TEM) on a FEI Tecnai T12 microscope and high-resolution TEM on an FEI Tecnai G2 30 instrument, scanning electron microscopy (SEM) using a JEOL 6500 SEM, and x-ray photoelectron spectroscopy

(XPS). Photoluminescence from the GaN nanocrystals was measured using the 325 nm emission of a HeCd laser at 5 mW power.

E.3 Results from Scheme A

During the synthesis for Scheme A, a pale yellow powder was collected on the stainless steel mesh filter at the exhaust of the reactor, and additionally a film was grown on the reactor tube walls. Fig. E2 shows SEM images of the powder. At low magnification, powder deposition in a thick layer can be seen on the mesh. The large rifts seen in the powder layer are due to flexing of the mesh. Higher magnification imaging shows that the thick layer is comprised of a fluffy network of particles. Based on this result, we also performed TEM and HRTEM on the GaN crystals. This imaging revealed a fairly wide size distribution of GaN crystals, as seen in Fig. E3. Dark-field imaging (Fig. E3b) indicates crystalline material, as does selected-area electron diffraction. We gave samples like these to Divakar Ramachandran, a member of Prof. B. Carter's group (at the time, in the CEMS department), for high-resolution TEM imaging. Dr. Ramachandran revealed that the small particles were indeed crystalline, and crystal planes can be seen in Fig. E3c.

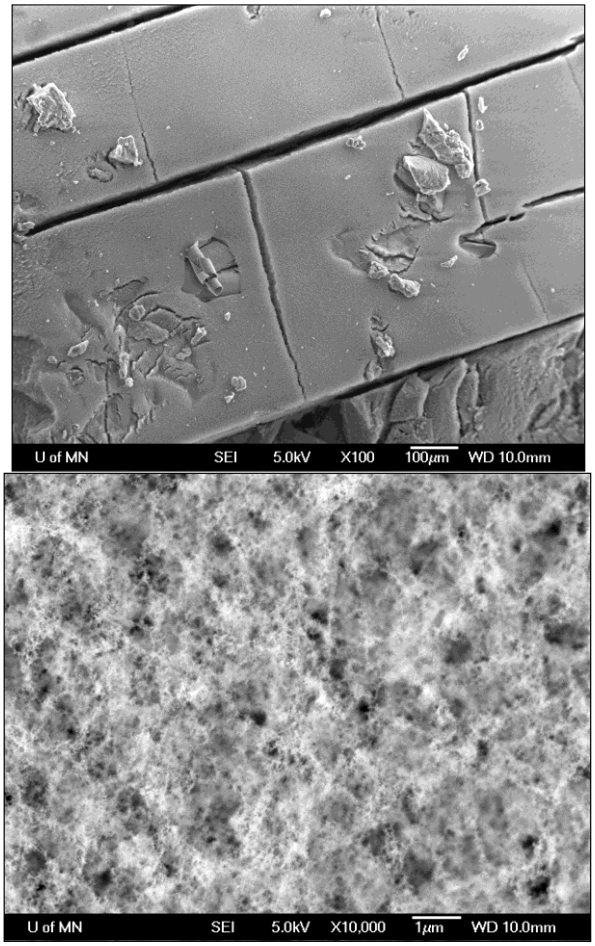

Figure E2: SEM images of GaN powder produced in the nonthermal plasma reactor.

We performed PL measurements on these samples, based on excitation with a HeCd laser. The PL curve is shown in Fig. E4a. As the band gap of GaN is 3.4 eV, we expected emission near this energy (~365nm). However, the emission we saw from this sample peaked near 2.7 eV, or 460nm. Due to the difficulty in incorporating nitrogen into GaN at a 1:1 stoichiometric ratio, defect emission in GaN in several PL bands due to surface states, impurities, and nitrogen vacancies, possibly occupied by oxygen, is not uncommon.[22-25] Indeed, XPS of the GaN nanoparticles revealed a small peak due to oxidation near the Ga 2p3 peak (Fig. E4b).

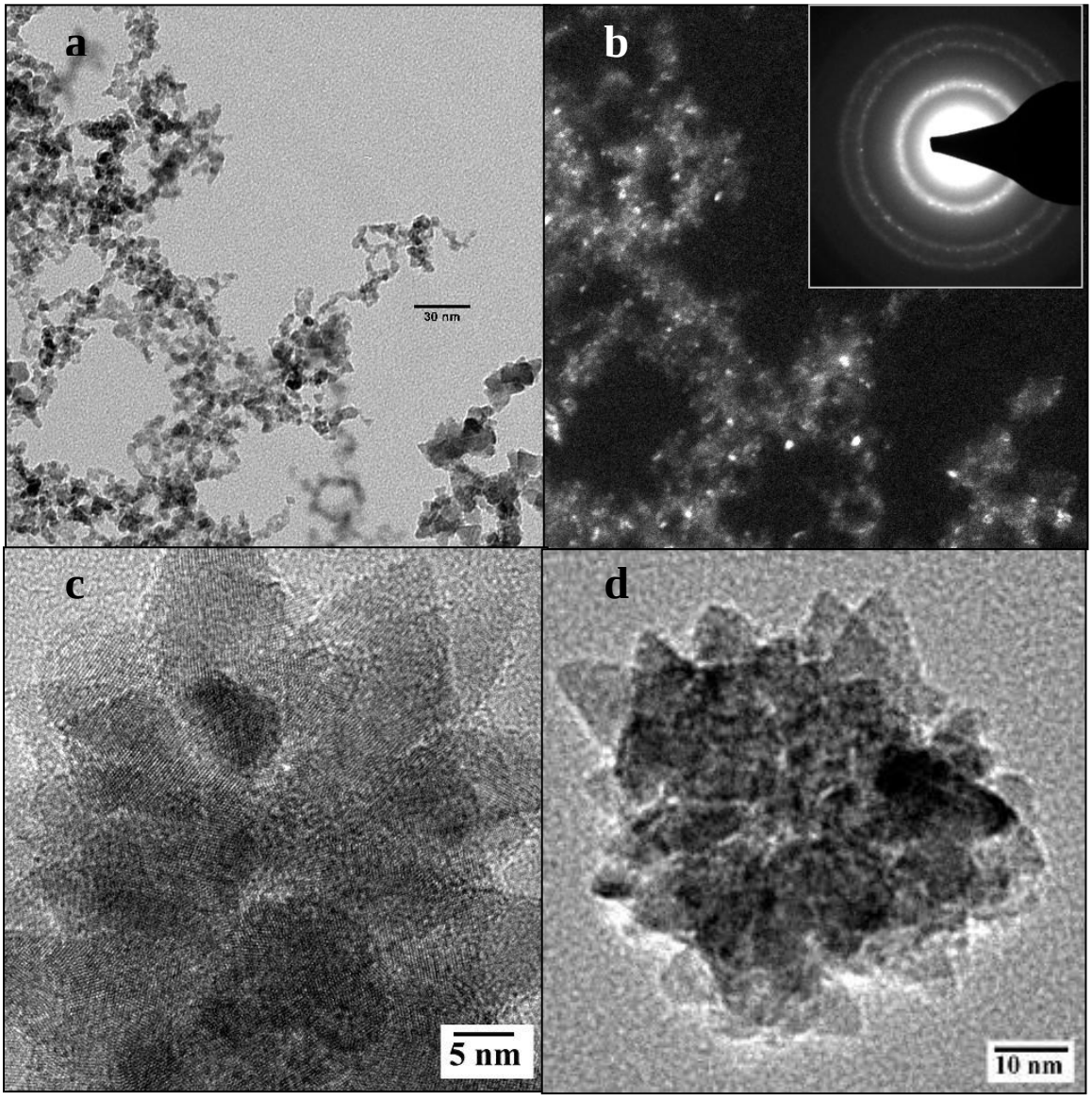

Figure E3: TEM images of GaN nanocrystals. (a) and (b) show conventional TEM images (bright-field and dark-field, respectively) of GaN nanoparticles. The inset in (b) shows the selected-area electron diffraction pattern. (c) and (d) are high-resolution TEM images of a cluster of GaN nanocrystals. Lattice planes can be seen in (c).

When examined with XRD, the powders revealed a zinc-blende / cubic crystal structure. While the equilibrium crystal structure for GaN is wurtzite / hexagonal, the

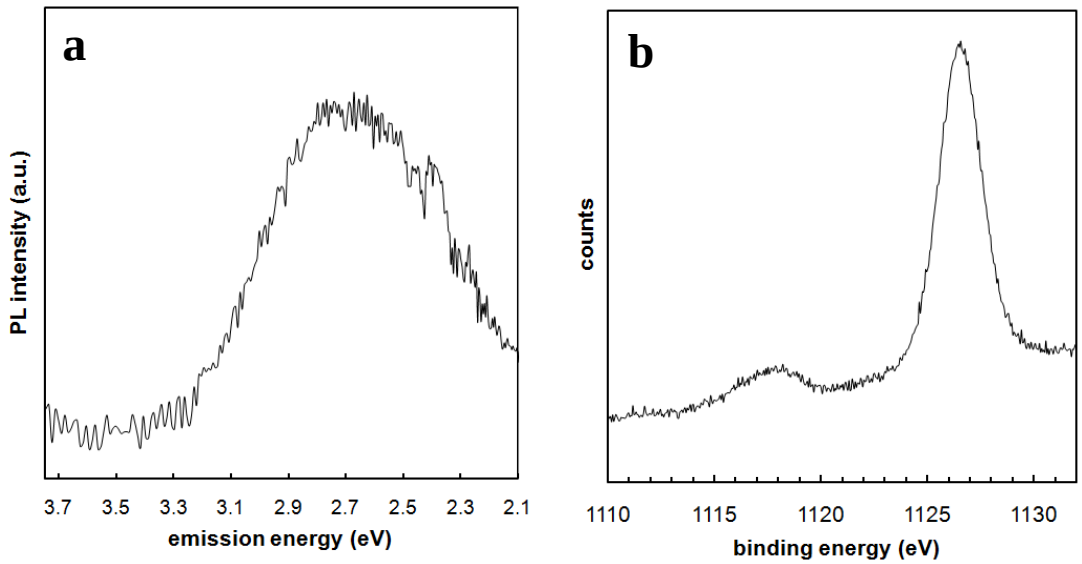

Figure E4: PL (a) and XPS (b) measurements from GaN nanocrystals. The PL emission peak is in the region for defect emission rather than band-edge emission. XPS shows a small peak due to oxygen around 1118 eV, near the Ga 2p3 peak at 1127 eV.

fast synthesis and rapid quenching of the particle temperature outside the plasma region of the reactor can potentially lead to nanoparticles in nonequilibrium structures. We also studied the crystal structure of the film grown on the walls of the reactor with XRD. For this film, which remains in contact with the plasma for the duration of the collection period, we see the equilibrium wurtzite structure. XRD patterns are depicted in Figure E5.

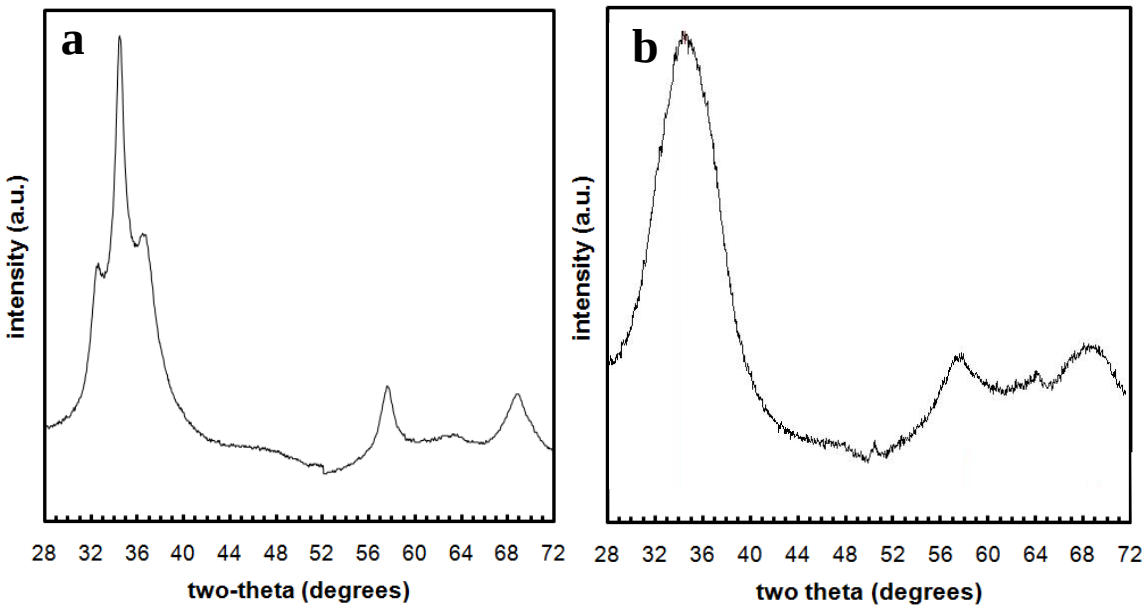

Figure E5: XRD patterns from GaN powder collected from (a) the reactor tube walls and (b) the collection mesh downstream of the plasma. The pattern in (a) shows a hexagonal structure, while (b) shows a cubic crystal structure.

E.4 Results from Scheme B

Based on this observation that the longer exposure time to the plasma led to the equilibrium crystal structure, in Scheme B a small piece of stainless steel mesh was inserted into the plasma discharge region of the reactor. The GaN material was deposited directly onto this mesh substrate and exposed to the plasma for the duration of the deposition. We first characterized the GaN nanocrystals using XRD, which confirmed that the hexagonal wurtzite structure was achieved for these samples (Fig. E6a). SEM imaging showed a dense and thick growth of larger-scale GaN crystals on the mesh (Fig. E6b). By scraping the material onto a TEM grid, we were able to get a closer look at the deposited crystals (Fig. E7). The triangle corners on some of the larger particles are interesting to note. Again, the size dispersity is not especially narrow. We performed PL

measurements on these samples as well; however, we again saw the defect emission near 2.7 eV rather than band-edge emission near 3.4 eV (Fig. E8).

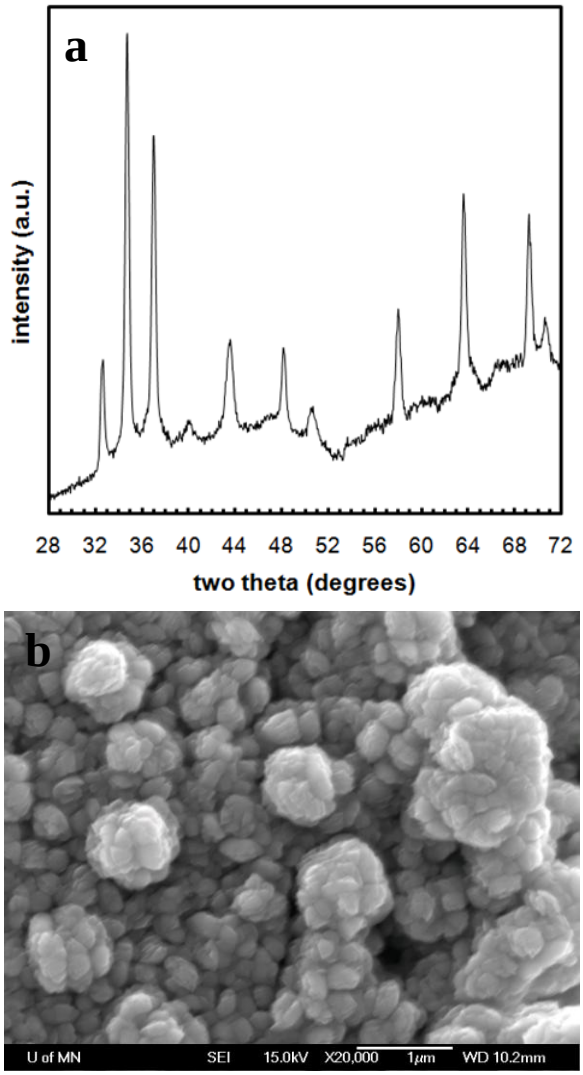

Figure E6: XRD pattern (a) and SEM image (b) of GaN crystals collected in Scheme B.

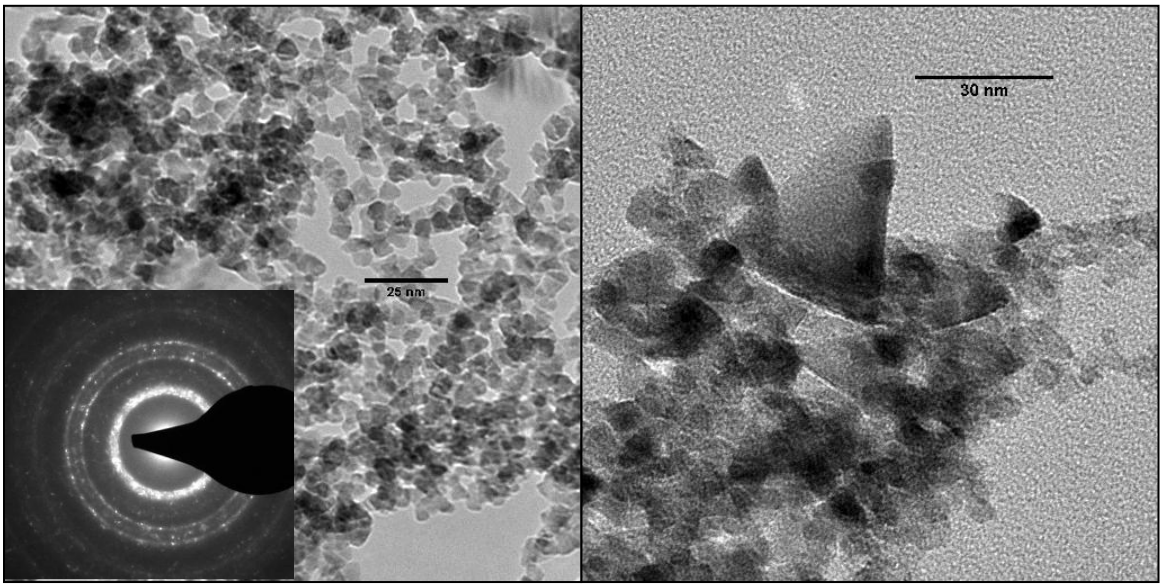

Figure E7: TEM images from GaN nanocrystals collected in Scheme B. The inset shows the selected-area diffraction pattern, indicating the presence of crystallites.

E.5 Conclusions

In conclusion, GaN nanocrystals can be successfully synthesized in a nonthermal plasma reactor. However, the nanocrystals exhibit defect emission only instead of the direct band-to-band emission of GaN. This defect emission is likely due to non-stoichiometry in the elemental makeup of the crystals, possibly at the surface, resulting in lower-energy emission than is predicted for GaN. One suggestion for future work is to find a way to reduce surface defects. While functionalization of the GaN surface may be difficult, an attractive option may be to grow a gallium oxide (Ga_2O_3) shell on the GaN

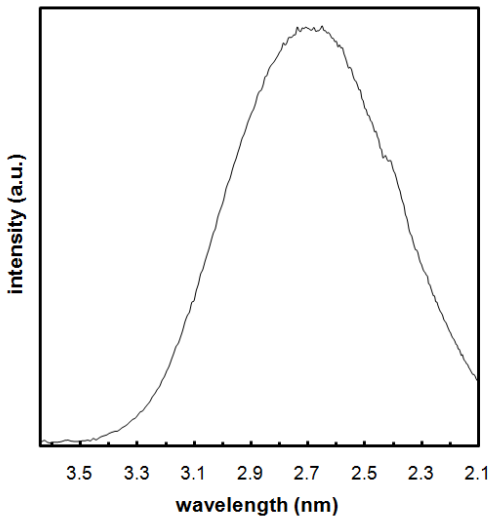

Figure E8: PL from GaN nanocrystals produced in Scheme B. The emission near 2.7 eV is again attributed to defects.

nanocrystals. We saw using XPS that oxidation of the GaN, perhaps at nitrogen vacancies, is one possible contributor to the defect emission from our GaN nanocrystals. However, a complete oxide shell may diminish surface defect states, and Ga_2O_3 has the wide band gap necessary for energy transfer through the shell.[26] Growth of the oxide layer could be achieved thermally[27] or *via* an additional plasma process, incorporating oxygen or an oxygen-containing gas into a region downstream of the synthesis plasma. A layer of oxide may passivate surfaces and allow the core GaN crystal to exhibit band-edge emission.

We would like to thank Elijah Thimsen who helped get this project started, Zak Holman for his help with SEM, Jason Schmidt for help with PL measurements, Brooke Timp (formerly Carlson) for her XPS expertise, and Divakar Ramachandran for high-resolution TEM.

References

(1) Lee, K. J.; Lee, J.; Hwang, H.; Reitmeier, Z. J.; Davis, R. F.; Rogers, J. A.; Nuzzo, R. G. *Small* **2005**, *1*, 1164-1168.

(2) Honda, Tohru; Akiyama, Miwako; Egawa, Shinichi; Aoki, Yohta; Obinata, Naoyuki; Kawanishi, Hideo. *physics status solidi (a)* **2004**, *201*, 2814-2817.

(3) Chitara, B.; Bhat, S. V.; Vivekchand, S. R. C.; Gomathi, A.; Rao, C. N. R. *Solid State Communications* **2008**, *147*, 409-413.

(4) Damilano, B.; Grandjean, N.; Massies, J.; Semond, F. *Applied Surface Science* **2000**, *164*, 241-245.

(5) Kendrick, C.E.; Anderson, P.A.; Kinsey, R. J.; Kennedy, V. J.; Markwitz, A.; Asadov, A.; Gao, W.; Reeves, R. J.; Durbin, S. M. *physics status solidi (c)* **2005**, *2*, 2236-2239.

(6) Tang, H.; Webb, J. B.; Bardwell, J. A.; Raymond, S.; Salzman, Joseph; Uzan-Saguy, C. *Applied Physics Letters* **2001**, *78*, 757-759.

(7) Ogi, Takashi; Itoh, Yoshifumi; Abdullah, Mikrajuddin; Iskandar, Ferry; Azuma, Yasushi; Okuyama, Kikuo *Journal* **2005**, *281*, 234-241.

(8) Coe-Sullivan, S.; Woo, W.; Steckel, J. S.; Bawendi, M.; Bulovic, V. *Organic Electronics* **2003**, *4*, 123-130.

(9) Cheng, K.; Anthony, R.; Kortshagen, U. R.; Holmes, R. J. *Nano Letters* **2011**, *11(5),*1952-1956.

(10) Wood, V.; Panzer, M. J.; Chen, J.; Bradley, M. S.; Halpert, J. E.; Bawendi, M. G.; Bulovic, V. *Advanced Materials* **2009**, *21*, 2151-2155.

(11) Gur, I.; Fromer, N. A.; Geier, M. L.; Alivisatos, A. P. *Science* **2005**, *310*, 462-471.

(12) Liu, C.; Holman, Z. C.; Kortshagen, U. R. *Nano Letters* **2009**, *9*, 449-452.

(13) Goodwin, T. J.; Leppert, V. J.; Risbud, S. H.; Kennedy, I. M.; Lee, H. W. H. *Applied Physics Letters* **1997**, *70*, 2133-2124.

(14) Hoshino, K.; Arakawa, Y. *Journal of Crystal Growth* **2004**, *272*, 161-166.

(15) Garcia, R.; Thomas, A.; Bell, A.; Stevens, M.; Ponce, F. A. *Materials Research Society Symposium Proceedings* **2004**, *798*.

(16) Kisailus, D.; Choi, J. H.; Lange, F. F. *Journal of Crystal Growth* **2003**, *249*, 106-120.

(17) Shimada, M.; Azuma, Y.; Okuyama, K.; Hayashi, Y.; Tanabe, E *Japanese Journal of Applied Physics* **2006**, *45*, 328-332.

(18) Mangolini, L.; Thimsen, E.; Kortshagen, U. *Nano Letters* **2005**, *5*, 655-659.

(19) Gresback, R.; Holman, Z.; Kortshagen, U. *Applied Physics Letters* **2007**, *91*.

(20) Gresback, R.; Hue, R.; Gladfelter, W. L.; Kortshagen, U. R. *Nanoscale Research Letters* **2011**, *68*.

(21) Pi, X. D.; Kortshagen, U. *Nanotechnology* **2009**, *20*.

(22) Cao, Y.G.; Chen, X.L.; Lan, Y.C.; Liang, J.K. *Applied Physics A* **2000**, *71*, 229-231.

(23) Kudrawiec, R.; Nyk, M.; Syperek, M.; Podhorodecki, A.; Misiewicz, J. *Applied Physics Letters* **2006**, *88*.

(24) Bondar, V. *physics status solidi (a)* **1999**, *176*.

(25) Reshchikov, M. A.; Moon, Y. T.; Gu, X.; Nemeth, B.; Nause, J.; Morkoc, H. *Physica B* **2006**, *376-377*, 715-718.

(26) Tippins, H.H. *Physical Review* **1965** *A 140*, 317-319.

(27) Xiao, Hong-Di; Ma, Hong-Lei; Xue, Cheng-Shan; Zhuang, Hui-Zhao; Ma, Jin; Zong, Fu-Jian; Hu, Wen-Rong *Materials Letters* **2005**, *59*, 4041-4043.

Appendix F: Copyright Permissions

The body of Chapter 2 was published in the journal *Physical Review B,* which is an American Physical Society (APS) publication. The APS states on its website, regarding the publication of APS journal articles in theses or dissertations, that "the author has the right to use the article or a portion of the article in a thesis or dissertation without requesting permission from APS, provided the bibliographic citation and the APS copyright credit line are given on the appropriate pages."

Parts of Chapter 5 have been published in the journal *Nano Letters,* which is published by the American Chemical Society (ACS). The American Chemical Society states on its website that "ACS extends blanket permission to students to include in their theses and dissertations their own articles, or portions thereof, that have been published in ACS journals or submitted to ACS journals for publication, provided that the ACS copyright credit line is noted on the appropriate page(s)."